Harvesting Electrical Energy from Air Bubbles Sliding along a Fluoropolymer

Master's Thesis in Physics, Measurement Science

Department of Physics and Technology

University of Bergen

Olav Ekornes Håskjold

September 2023

Supervisor: Professor Lars Egil Helseth, UIB

Abstract

The increased use of small, off-grid, electronic applications call for improvement in harvesting energy from mechanical motion in the environment and transducing it into electricity. Recent studies propose devices generating electricity from rising bubbles in water, altering the electric field along a charged polymer. In this work, a device consisting of two copper electrodes imbedded behind a fluoropolymer film is submerged in water and subjected to air bubbles. The device's ability to transduce the mechanical energy from bubbles into electricity is shown to be dependent on the thickness of the fluoropolymer film. First, it is found that short circuit charge transfer between electrodes increase with decreasing thickness. However, under high resistive load, medium thickness yields the highest charge transferred and the highest transduced energy, reaching 1.2 μJ for a 1.95 ml bubble. A theoretical model is presented and shown to qualitatively replicate the features of the measured data. Comparable studies have not yet addressed the effect of electrification layer thickness. This work shows that this is an important factor in optimizing energy transduction. The presented findings might therefore have useful implications for further development of bubble energy harvesting.

Acknowledgements

I would like to thank my supervisor, professor Lars Egil Helseth, for generously giving of his time in guiding me. I would also like to thank Carsten Peter Hinzmann, Nora Stenersen, Elin E. Håskjold and Frode Håskjold Fagerli for valuable feedback. Last, but most important, Lene, for your support and patience.

List of abbreviations

FEP	Fluorinated ethylene propylene
EDL	Electric double layer
CE	Contact electrification
BMAT	Bubble motion active transducer
TENG	Triboelectric nano generator
PTFE	Polytetrafluorethylene

List of figures

List of tables

List of symbols used in the text

E_1	Bottom electrode.
E_2	Top electrode.
$I(t)$	Current between electrodes.
$\frac{dA(t)}{dt}$	Rate of change in overlap between bubble and E_1 minus rate of change in overlap between bubble and E_2.
$A_{b1}(t)$	Area under bottom electrode covered by the bubble.
$A_{b2}(t)$	Area under top electrode covered by the bubble.
$A_{W1}(t)$	Area of FEP surface directly under bottom electrode in contact with water.
$A_{W2}(t)$	Area of FEP surface directly under top electrode in contact with water.
A_E	Area of one electrode.
$Q_{I1}(t)$	Charge induced by internal redistribution of charge in electrode.
$Q_{I2}(t)$	Charge induced by redistribution of charge between electrodes.
σ	Surface charge density of FEP surface.
ε_{FEP}	Permittivity of FEP.
d	Thickness of FEP sheet.
ε_0	Permittivity of free space.
D	Distance between electrodes.
C_p	Direct mutual capacitance between electrodes.
$A(t)$	Area directly under bottom electrode covered by bubble minus area covered by bubble under top electrode.
$C_{E1}(t)$	Bottom electrode capacitance with water.
$C_{E2}(t)$	Top electrode capacitance with water.
$C_{total}(t)$	The total capacitance of the system.
C_p	The direct mutual capacitance between the two electrodes.
$C_s(t)$	The total serial capacitance through the water.
C_{GROUND}	Capacitive connection between E_2 and water through ground.
$V(t)$	Voltage across load.
R	Resistance of load.

R_W	Resistance in water between electrodes.
W_b	Width of bubble.
l_b	Length of bubble.
W_E	Electrode width.
l_E	Electrode length.
v	Speed of bubble along device.
T_b	Time needed for the bubble to travel one length of its body.
W	Width of bubble where it intersects with a specified electrode edge.
Δt	Time interval between two discrete measurements.
$M1$	Simulation result from model 1.
M1*	Simulation result from model 1 where C_{GROUND} is accounted for.
M2	Simulation result from model 2.
M2*	Simulation result from model 2 where C_{GROUND} is accounted for.
$I_{s1}(t)$	Current past $C_{E1}(t)$ in model 2.
$I_{s2}(t)$	Current past $C_{E2}(t)$ in model 2.
$V_1(t)$	Potential at E_1 relative to water body in model 2.
$V_1(t)$	Potential at E_2 relative to water body in model 2.
V_s	Surface potential.

Contents

1 INTRODUCTION

1.1 BACKGROUND

An increasing number of technical equipment calls for new forms of power generation in order to be viable. Some examples include self-powered sensors, wireless networks, wearable electronics, environmental sensing and other small, low-power, off-grid applications [1]. Important factors are size, simplicity, reliability and cost. In light of this, devices with simple design and no moving parts are attractive. Being able to avoid the need to change batteries is also both economically and environmentally desirable. This calls for investigation and improvement of new methods of harvesting different types of ambient energy and transducing it into electrical form [1-4]. This should be done, preferably, in ways minimizing complexity and the need for maintenance.

Much of the harvestable energy in the environment exists in three forms. These are electromagnetic radiation, temperature gradients and mechanical motion. Table 1.1 lists these exploitable sources of energy available in the environment, with some examples and typical energy densities obtained.

Energy Source	Types	Energy-Harvesting Method	Power density
Radiant	Solar	Solar cells (indoors)	$<10\mu W/cm^2$
		Solar cells (outdoors, sunny days)	$15mW/cm^2$
	RF	Electromagnetic conversion	$0.1\mu W/cm^2$ (GSM)
		Electromagnetic conversion	$0.01\mu W/cm^2$ (WiFi)
Mechanical	Wind Flow and Hydro	Electromechanical conversion	$16.2\mu W/cm^3$
	Acoustic Noise	Piezoelectric	$960nW/cm^3$
	Motion	Piezoelectric	$330\mu W/cm^3$
Thermal	Body heat	Thermoelectric	$40\mu W/cm^2$

Table 1.1: Main sources of harvestable energy in the environment, how they can be transduced and typical power densities. Adopted from [1].

Radiant energy in the form of solar radiation is most commonly harvested by photovoltaic panels. In addition to a substantial contribution to the utility power grid [5], photovoltaic panels are commonly used as power sources in off-grid applications such as navigational marking, environmental sensors and satellites. Among the advantages of this technology is its high energy density and robustness. Photovoltaic panels have no moving parts and the need for maintenance is low. Moreover, they

generate a direct current output, easily used directly in many applications. However, the availability of sufficient solar radiation is variable and can be unpredictable.

In urban areas, harvesting of radio frequency electromagnetic radiation could be viable for some applications if high emitting sources are nearby [2]. This can be done simply by rectifying the signal from an antenna into DC-current. This is advantageous because system design is simple and background RF energy tends to be constant, limiting the need for storage. However, energy density typically obtained is low.

Sharp temperature gradients can be utilized by thermoelectric generators, transducing heat flow into electricity. While inefficient, this is a good example of a highly reliable method of generating electrical power with no moving parts [4].

In environments absent of both exploitable electromagnetic radiation and sharp temperature gradients, mechanical motion in ambient medium is one of the few remaining energy sources that can be utilized – perhaps the only viable one. Examples of such environments could be in the polar regions during wintertime or under water.

The most important physical phenomena utilized to transduce mechanical motion into electricity are electromagnetic induction, the piezoelectric effect and electrostatic induction. These phenomena are illustrated in figure 1.1 respectively from left to right.

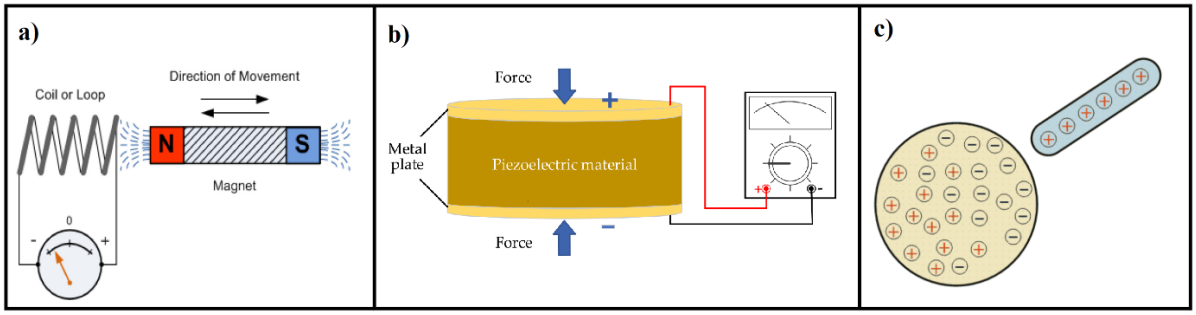

Figure 1.1: Phenomena used to transduce mechanical motion into electricity. a): Electromagnetic induction. Figure adopted from [6]. b): Piezoelectric transduction. Figure adopted from [7]. c): Electrostatic induction. Figure adopted from [8].

The principle of electrostatic induction is illustrated in figure 1.1 a). When the magnetic flux through a loop of conductor is changing, a current is induced in the loop. The majority of electrical power consumed by human activity stems from generators relying on this principle[9]. Electromagnetic generators are highly efficient in transducing mechanical energy into electrical energy, but often not practical for harvesting ambient forms of energy at a small scale. A strong magnetic field is needed, which implies either strong permanent magnets or an electromagnet. This adds to weight and complexity.

Piezo electric materials create an electric field when subjected to mechanical force. This field is used to induce charge in electrodes placed on the material, as shown in figure 1.1 b). The construction of

piezoelectric energy harvesters is simple and easy to scale down in size. As suggested in table 1.1, piezo electric devices can harvest energy from vibrations in the environment [7]. However, energy density is low and the output is alternating current, which must be rectified before use in most applications, adding to necessary hardware [1].

Electrostatic induction, illustrated in figure 1.1 c), can be utilized to transduce mechanical motion into electricity. One general method of doing this relies on statically charged materials interacting with conductive materials. In essence, this works by moving the statically charged material relative to the conductor. This makes charge redistribute within the conducting material, and the redistribution of charge constitutes a current. If the current is channeled through an outer circuit, it can be used to do work. The outer mechanical motion provides the force to create the relative motion between the statically charged material and the conducting material. The source of the static electric field used can be due to the materials contact electrification properties. These devices, are often referred to in the recent literature as triboelectric generators or triboelectric nanogenerators (TENG) [3, 10-13].

In general, triboelectric generators have several promising advantages. First, contact electrification is a surface phenomenon. Therefore, the use of thin-film materials can maximize active area per unit mass of material used, potentially bringing down cost, weight and increasing power density. Second, some materials exhibiting high triboelectric performance, are cheap and easily manufactured into thin films. A third point is that such devices harvesting energy from ambient motion, can be made with very few or even no moving parts. This leads to simple manufacturing, low probability of malfunction and low need for maintenance. Last, water, in many possible applications being the ambient medium one wishes to harvest mechanical energy from, exhibits strong contact electrification effects between itself and a number of materials [14]. If a high enough transducer efficiency is reached, these devices could conceivably be used as power sources for small, low-power applications in aqueous environments [3, 10, 15].

There have been several reports on triboelectric generators which rely on contact electrification between ambient water in motion, and the device itself [15-31]. In 2015, Helseth and Guo squeezed a water droplet in between a metal electrode and a fluorinated ethylene propylene (FEP) sheet with the second electrode over it, creating a peak power near 5 μW [21]. Helseth and Guo showed in several studies that falling raindrops could generate electricity when impacting and sliding across a sheet of an electret polymer with electrodes embedded underneath [18-20]. Similar devices have been reported to harvest water wave energy. For example Zhu et al. reported a device based on a nanostructured fluorinated ethylene propylene with electrodes imbedded underneath which was alternatingly submerged in water [17]. Another report by Xiya Yang et al. proposed to harvest wave energy with a contact-separation mode TENG in 2018 [16]. They looked at different frequencies of contact-separation, different surface modifications of the polytetrafluoroethylene (PTFE) surface, and different

resistive loads. A maximum power density of 9.62 Wm^{-2} was reported using saline water and a surface with a micro scale rhombic pattern [16].

Besides droplets falling or waves sloshing, another form of mechanical energy available for harvesting in water environments is ascending bubbles. Some researchers have proposed to harvest energy by collecting bubbles in a natural environment, directing them to drive a turbine with a conventional electromagnetic generator [32, 33]. However, with regards to simplicity, devices relying on no moving parts would be an improvement to this. One way to achieve this is to employ the same principles as used for harvesting droplet and wave energy by means of contact electrification and electrostatic induction. For the last decade, a few researchers have reported on devices generating electricity from bubbles by means of altering the electric field forming along a charged surface in water [22-24, 27-30]. The research done on these devices is limited.

In 2015, Yang et al. showed how two-phase flow (water and air) in small tubes could generate electricity by altering the electric double layer and inducing charge in imbedded electrodes. They proposed the possible application of a small scale, self-powered sensor for sensing air slugs in water that was flowing in a tube [30]. In 2016, Chen et al. used one electrode imbedded in PTFE on the inside of a waterfilled cylinder to generate electricity when bubbles ascended along its surface [29]. The proposed application being a self-powered sensor of gas flow in medical equipment. Li et al. (2022) experimented with a two-electrode system employed in a PTFE tube generating electricity from bubbles passing in the tube water flow [24]. The first electrode was on the outside of the tube, the second was on the inside of the tube, in contact with the deionized water. Electrode width, distance between electrodes, bubble volume and frequency were discussed and illustrated as contributing factors to output performance. In 2023, the same lead author reported a similar design, which further investigating the effect of tube diameter, electrode length and bubble volume, and was able to reach a peak power of 4.5 μW for a bubble of 10 ml [22].

In a 2017 report, Wijewardhana et al. showed how rising bubbles could generate electricity while sliding across a flat substrate [28]. They compared this against harvesting energy from droplet movement in air with the same device. In this study, bubbles of air would slide across a tilted submerged PTFE surface with two electrodes imbedded underneath. The bubbles disturbed the electric double layer on the polymer and thereby induced charges in the imbedded electrodes. Wijewardhana et al. called this device a bubble motion active transducer, BMAT. In a following study the same group further investigated the design and added electrodes in parallel (interdigitated) exploring how output could be increased and how increasing electrode area effected output [27]. Figure 1.3 shows the BMAT operating in water (a) and how the same device also can harvest energy from a droplet sliding across it in air (b).

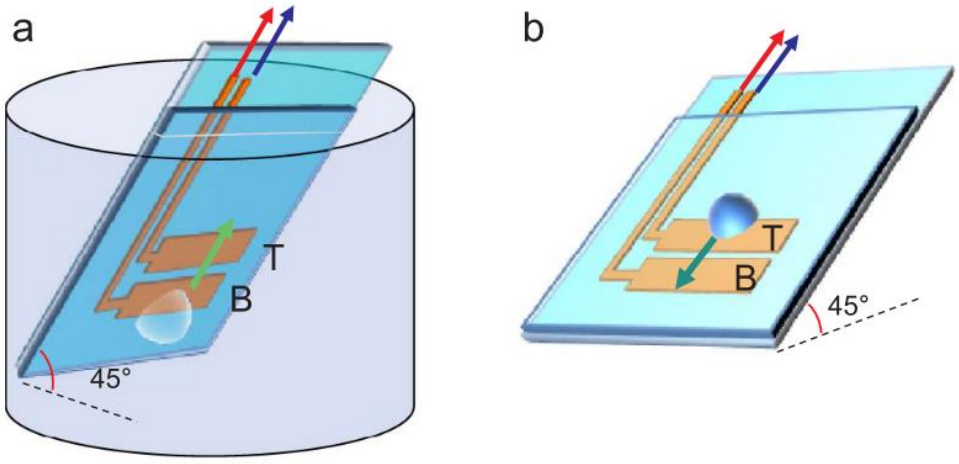

Figure 1.2: BMAT as illustrated by Wijewardhana et al [28]. a): The device operating in water. A bubble connects with the surface and slides across it pass the two imbedded electrodes. A current between the electrodes through an outer circuit (not shown) is induced. b): The same device operating in air. A droplet of water falls on the surface and slide across the electrodes. Current is induced between the electrode through the outer circuit. Figure adopted from [28].

In 2022, Yan et al. made a similar device generating electricity as bubbles rose and impacted a flat electrode imbedded behind a PTFE surface. The authors reported a peak power generated of 5.64 µW and 172 nJ energy harvested from a single 0.1 ml bubble, claiming the output of their device to prove more than an order of magnitude better than existing studies [23]. Like in the report by Li et al [24], the second electrode was here in direct contact with water.

The aforementioned works on harvesting energy from bubbles passing statically charged surfaces, investigate several important factors and their effect on power output. Among these are ion availability in the water [16] , electrode geometry [22, 24, 27], bubble size and speed [22], surface topography [16] and surface treatment with plasma [23, 28]. Some of these works mention the thickness of the electrification layer used in experiments. However, there is no discussion or justification provided for the choice of thickness. Previous research on surface charging of polymers suggests that this should be considered, as it might impact surface charge density, and therefore performance. For example, in 1991 Xia and Jiang reported that the thickness of an FEP film was correlated to its surface charge density after corona charging [34]. The thinner film in this study obtained the highest surface charge density after equal treatment as a thicker one. Two years later, Yatsuzuka et al. studied how drops of ultra-pure water falling on a PTFE surface gained positive charge, leaving the surface net negative. Based on scanning of the surface potential and measuring of the charge gained by the droplets that had been in contact with the surface, they concluded that electrification of a polymer surface by pure water was influenced by the thickness of the polymer [35]. They reported that surface charge density became lower as the thickness of the polymer was increased. In light of this, electrification layer thickness might impact electrostatic bubble energy harvester output.

Another reason to question the effect of electrification layer thickness in submerged devices is its relationship to capacitance. If the electrification layer thickness is the distance between the water and the electrode, a thinner electrification layer should increase the capacitance between charges in the electrodes and charges in the adjacent water.

Wijewardhana et al. showed how capacitance increased with increasing electrode area. The increase in capacitance greatly decreased the system output in this case [27]. Therefore, if thickness of the electrification layer effects capacitance, it should be considered because the output of such devices has been shown to be sensitive to capacitance.

In the wider context of electrostatic energy harvesting with triboelectric materials, a few studies have discussed the effect of the electrification layer thickness in a standard contact-separation mode TENG [36-38]. In this context, thinner electrification layer is reported to be better both in terms of open circuit voltage and short circuit current. Some have focused on increasing the dielectric constant of the electrification material, reporting similar results [39, 40]. Because of their different principles of operation, it is not given that these conclusions apply to the devices harvesting bubble energy discussed above. Several reports show how electrodes imbedded behind a submerged hydrophobic polymer can generate current in an outer circuit when bubbles slides across its surface [22-24, 27, 28]. However, it is not found that any of these consider the dependency of polymer thickness on the effectiveness of energy harvesting.

1.2 THESIS OBJECTIVE

The aim of this thesis is to demonstrate how bubbles sliding across a submerged fluorinated ethylene propylene film can generate electric current between electrodes imbedded through an outer circuit. The main goal is to gain understanding of how the thickness of the FEP film affects the device's ability to harvest energy from the moving bubbles. Different thicknesses of the electrification layer (FEP) are used in the test devices to observe its impact on performance. First, a simple idealized model is analyzed in order to get a quantitative understanding of how device geometry may relate to electric current through a test load connected between electrodes. Second, test devices are built, tested and compare with the model.

2 THEORY

2.1 BACKGROUND

2.1.1 Contact electrification between a solid and water

Contact electrification is used as a collective term for phenomena involving spontaneous charge transfer between two substances in contact. The term triboelectricity is often used in cases where friction or rubbing between the materials occur, sometimes increasing the amount of charge transferred [41]. Contact electrification also occurs between solids and liquids [26, 31, 42-44]. More specifically, in this is this work the liquid is water and the solid is fluorinated ethylene propylene (FEP). FEP exhibits strong contact electrification properties, tending to obtain a negative charge [45]. FEP is a copolymer of hexafluoropropylene and tetrafluoroethylene. It has many of the same properties as polytetrafluoroethylene (PTFE), however it has some additional advantages. It can in many applications be treated as a traditional thermoplastic. It can be welded, molded and laminated. FEP is a material resistive to a wide range of outer stresses like temperature, wear and tear. It is extremely chemically inert and can handle contact with a wide range of compounds without degrading [46].

It has been shown that water streaming along the surface of a hydrophobic material, such as FEP, obtains a net positive charge, leaving the solid surface net negative [35, 47-49]. In other words, a transfer of charge occurs between the water and the solid. The exact mechanism behind this transfer of charge and what the charged species involved are, is still a matter of debate [42, 43, 50-52] and will not be discussed further here. When a hydrophobic material is submerged in water, negative charge is adsorbed on its surface. The now net negatively charged surface creates an electric field, attracting positive charges in the bulk water. The result of this is a net positive layer adjacent to the surface, gradually decaying the field from the surface bound negative charge. The net positive charge of this layer corresponds to the net negative charge on the solid surface. This arrangement is often called an electric double layer (EDL). How far into the bulk water this layer extends depends mainly on ion availability and also temperature. Commonly, the Debye-Hûckel length is used as a measure of the characteristic thickness of this layer. For pure water this length is on the order of 1µm. As availability of ions increase, this distance decreases [53].

Figure 2.1 shows an idealized illustration of the above discussion. A conductor imbedded between a sheet of FEP and an isolating material is submerged in a container holding water. The surface region becomes net negatively charged by contact electrification. The net positive charge in the diffuse layer screens the field from the surface charges. As we move further from the FEP surface the bulk water gradually becomes net neutral. The FEP can therefore be considered net negatively charged while the water gains a complementary positive charge. Because the field from the surface charges and the diffuse layer are of equal magnitude but opposite direction the imbedded conductor in the figure experiences no electric field.

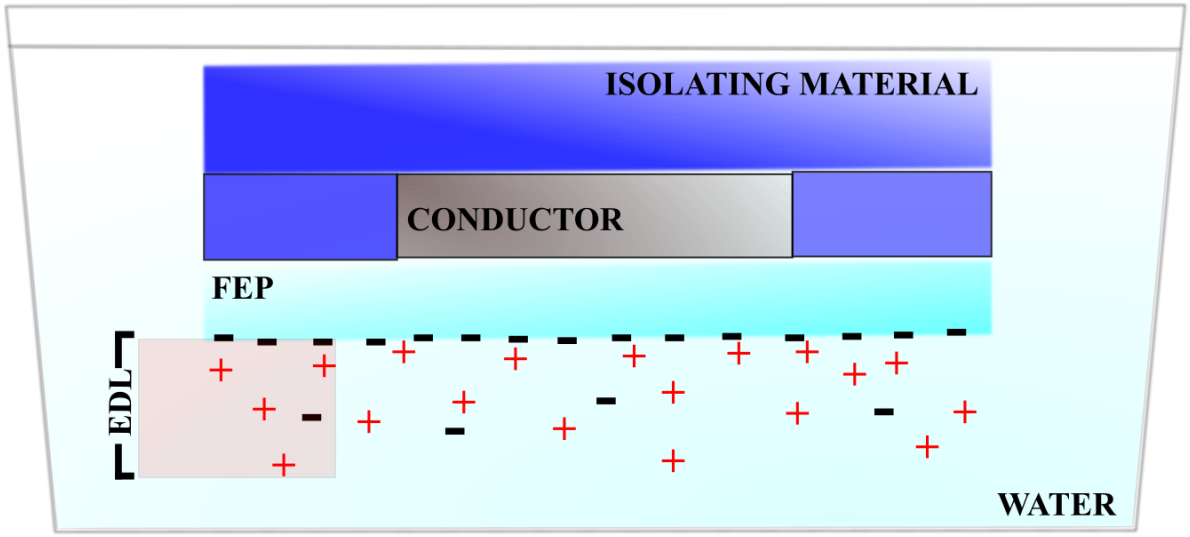

Figure 2.1: A conductor imbedded between a sheet of FEP and an isolating material is submerged in a container holding water. Negative charge species from the water adhere to the surface. A diffuse layer of positive charge in the bulk of the water body screens the field from the surface charges. The FEP becomes net negatively charged while the water gains a complementary positive charge.

2.1.2 Electrostatic induction

When a neutral conductor is subjected to an electric field, charges within it will redistribute in response. This redistribution continues until the distribution of charge within the conductor is such that the resulting electric field is the exact opposite of the original field. When this stage is reached, the superposition of the original field and the field due to the redistributed charges in the conductor is zero within the conductor [54].

As an example of electrostatic induction, consider the situation in figure 2.1. Suppose a bubble rise from below and connects to the FEP surface. This is shown in figure 2.2. In displacing the bulk water next to the surface, it has removed the most of the positive diffuse layer locally. The surface charges are bound tighter to the surface and stays in place, giving this region a net negative charge. Assuming the bubble has displaced the positive charges far enough away not to affect the conductor, the conductor is now subjected to an electric field from the negative surface charges. We assume that the height of the bubble is much larger than FEP thickness, making this is a valid approximation.

Redistribution of charge occurs within the conductor as a response to this field. Positive charge piles up at its bottom surface while a corresponding negative charge piles up at its upper surface.

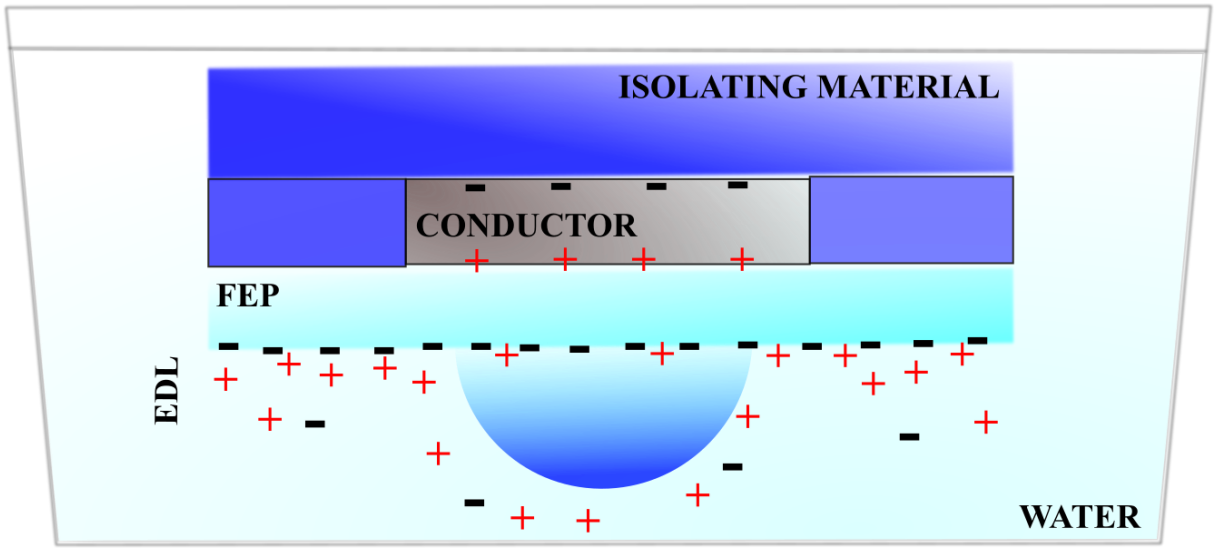

Figure 2.2: The same illustration as in figure 2.1 but with a bubble in contact with the FEP surface. The bubble displaces the positive diffuse layer along the surface leaving it negatively charged because of the more stationary negative surface charges. This leads to the conductor being subjected to an electric field. Charge within the conductor is redistributed because of this

It is probable that some of the positive counter charges are more tightly bound to the surface than others and therefore require more force to be displaced from the surface. For a given mechanical intervention it can therefore be expected that some of the positive charges is removed, and others to stay in place. In figure 2.2 this is illustrated as two positive charges remaining on the FEP surface covered by the bubble.

In the following discussion we will usually consider surface charge density as the net surface charge density after water has been removed from the surface, including any remaining positive charge species. We could call this the effective surface charge density because it determines the potential to induce charge in a nearby conductor. Everywhere surface charge density is mentioned, this is what we refer to. In this manner the following discussion and figures are simplified, only considering the net negative charge on the surface and the loosely bound corresponding net positive counter charge removed by the influence of a bubble.

2.2 THEORETICAL DESCRIPTION OF THE SYSTEM

2.2.1 Qualitative description

The term bubble motion active transducer, BMAT, was coined by Wijewardhana et al. in a 2017 report [28]. This described a device consisting of a PTFE surface with two electrodes imbedded between it and a glass substrate. The BMAT generated current between the electrodes as bubbles ascended along the PTFE surface.

The device investigated in this thesis is analogous to the one studied by Wijewardhana et al. [28]. We will therefore borrow BMAT as a term. In this thesis, it is used to describe any device transducing bubble motion in water into electricity, by disturbing the EDL along a statically charged material in water, thereby inducing charge in one or more imbedded electrodes.

The BMAT architecture in this thesis consists of two flat metal electrodes covered by a sheet of fluorinated ethylene propylene. The electrodes are connected to each other via an outer circuit with copper wire. Above the electrodes a substrate of acrylic plastic and sealant silicone ensure that water does not come into contact with the electrodes. The device is submerged in water with the polymer surface downward and placed at an angle relative to the horizontal plane so that one electrode is deeper than the other, as illustrated in figure 2.3 and 2.4.

We assume that the FEP surface holds a time constant, homogenous, static, negative surface charge due to contact electrification with the water. When the BMAT is submerged, charges in the water body redistribute such as to screen the field from the polymer surface. An electric double layer forms.

When a bubble rises below the device it makes contact with the polymer surface. The hydrophobicity of the polymer and the bubble's buoyancy allows it to displace water and create a dry region on the surface [28]. The angle of the plane and the buoyancy of the bubble results in the bubble, and the dry region on the surface associated with it, to transverse along the surface. We approximate that the bubble perfectly displaces the water along the surface and that no positive ions or other charged species from the EDL remain on the surface in this region. The assumption that water is completely removed results in removal of positive charge. We assume that this positive charge is removed so far away from the FEP surface that its remaining effect on the electrodes can be neglected. When the bubble overlaps with an electrode, the remaining negative charge on the FEP surface will induce a positive charge in it.

The thickness of the FEP sheet is many orders of magnitude smaller than the electrode dimensions in the plane of the device. Therefore, we approximate that electric field flux normal to the device surface dominates. This leads to a one-to-one relationship between the amount of surface charge exposed under the electrode and the amount of opposite charge induced in the electrode.

We propose that the induced charge in the electrode can be divided into two idealized types representing two extreme situations.

1. The induced charge due to internal redistribution of charge within the electrode. *No conduction between the electrodes is possible.*
2. Induced charge due to redistribution of charge between electrodes. *There is no resistance between the electrodes.*

Figure 2.3 illustrates the BMAT and the two types of induced charge proposed.

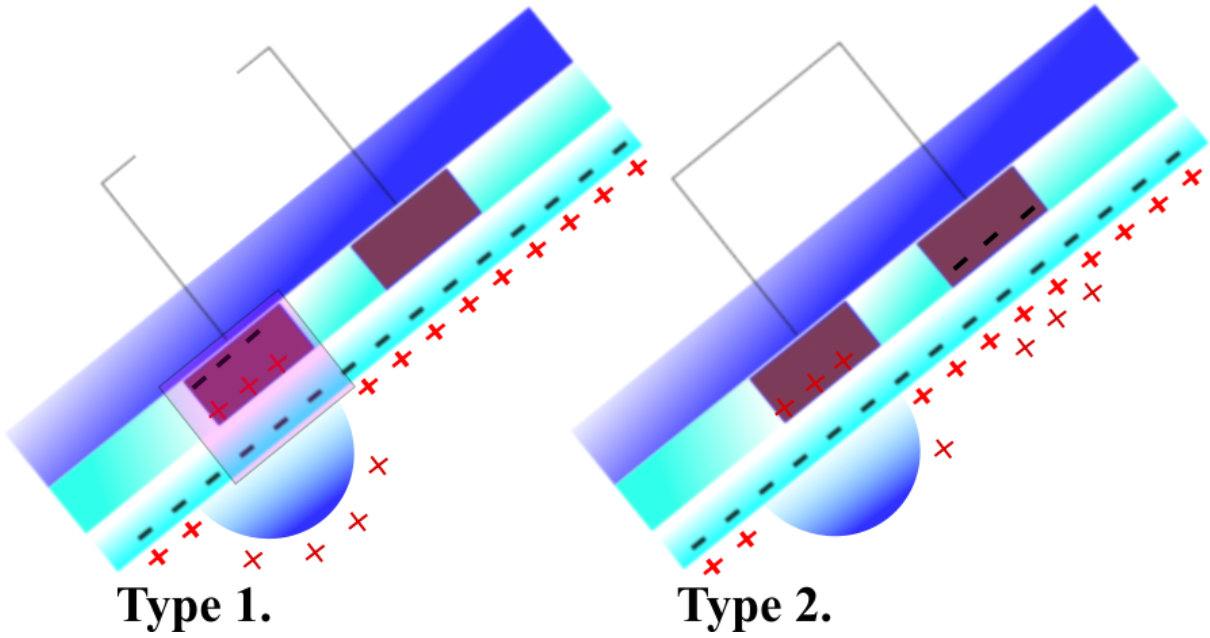

Figure 2.3: Type 1 and type 2 induced charge in the bottom electrode as a bubble overlap with it and thereby removes the positive charges in the water. A pink Gaussian "pillbox" is illustrated around the bottom electrode and the exposed FEP surface underneath in type 1. The region enclosed by this volume has a net negative charge and therefore a net electric field flux into it. The same volume has no net charge in type 2. Therefore, there is no field flux through that surface. In this figure the EDL is simplified, showing only its net positive charge.

Type 1:

Charge is induced in the electrode due to internal redistribution of charge within it. Drawing a Gaussian "pillbox" around the exposed FEP surface and the electrode, we see that this region now has a net negative charge. This is illustrated by a pink square in the left part of figure 2.3. Therefore, there is now an electric field between the electrodes. The other electrode feels the electric field from this region resulting in a displacement current between the electrodes. No physical current runs through the wire connecting the electrodes. There is no net change in charge in any of the electrodes due to this effect. We approximate that all induced charge in the electrode would be in this form if the load resistance is infinite.

Type 2:

If charge is induced in the electrode due to redistribution *between* the electrodes, this must involve conduction current through the wire from the top electrode to the bottom electrode in figure 2.3. The bottom electrode obtains a net positive charge, the top electrode obtains a net negative charge. We assume the negative charge in the top electrode to attract a corresponding positive charge to the diffuse layer below it. The Gaussian boundary surface around the bottom electrode and the exposed surface charges obtains no net charge. The same is true if we draw a similar boundary around the top electrode, including the diffuse layer. Therefore, there is no field between the electrodes. We approximate that all induced charge in the electrode would be in this form if the load resistance is zero.

From the above assumptions type 1 and type 2 induced charge must at any time sum up to the total amount of induced charge. The total amount of induced charge is equal to the product of exposed area under the electrode and the FEP surface charge density.

$$Induced\ charge = Area\ exposed\ \times Surface\ charge\ density.$$

If a bubble slides across the whole device, it will first affect the bottom electrode and then the top electrode. We define current to be positive when flowing to the bottom electrode and divide the process into four phases. These are illustrated in figure 2.4. The illustration shows the expected situation for a low load resistance, discussed as type 2 induced charge above.

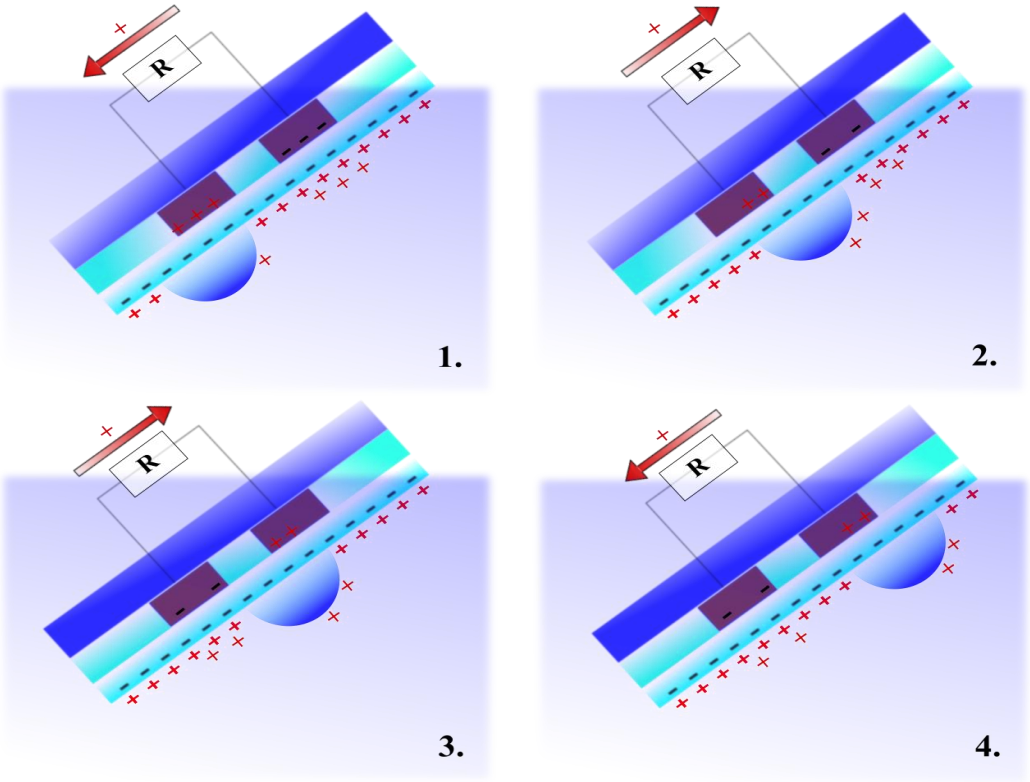

Figure 2.4: Mode of operation of the BMAT. The red arrow denotes the direction of the conventional current. 1: The bubble increases its overlap with the bottom electrode, inducing positive charge in it. Current flows towards the bottom electrode. 2: The bubble slides off and decreases its overlap with the bottom electrode. Current flows back to the top electrode. 3: The bubble slides onto and increases its overlap with the top electrode. Positive charge is induced in it. Current flows to top electrode. 4: The bubble slides off and decreases its overlap with the top electrode. Current flows back to bottom electrode.

1) The bubble increases its overlap with the bottom electrode and removes positive charge from the FEP surface, leaving it negatively charged. Positive charge is induced in the electrode as a response to the field from the FEP surface. Conduction current flows towards the bottom electrode through the load from the top electrode (positive current).
2) The bubble slides off and decreases its overlap with the bottom electrode. This is the reverse of phase 1. Positive charge from the water comes back to the FEP surface, screening the negative charges on it. The net positive charges induced in the electrode in phase 1 flows back to the top electrode (negative current).
3) The bubble slides onto and increases its overlap with the top electrode and removes positive charge from the FEP surface under it, leaving it negatively charged. Positive charge is induced in the top electrode in response to this field. Conduction current therefore flows to the top electrode from the bottom electrode (negative current), giving it a net positive charge.
4) The bubble slides off and decreases its overlap with the top electrode. This is the reverse of phase 3. Positive charge from the water comes back to the FEP surface, screening the negative charges in it. The net positive charges in the top electrode flows back to the bottom electrode (positive current).

In sum, the total charge transferred through the load is zero. The phases described above does not have to be successive and distinct. If, for example, the electrodes are close enough for the leading edge of the bubble to start overlapping with the second electrode before its trailing edge has left the first, the current of phase 2 and 3 will merge and create a shorter pulse of higher amplitude. This can be thought of as a superposition of phase 2 and 3. [27]. If both electrodes were to be subjected to the exact same influence at the same time, their contribution to $\frac{dA(t)}{dt}$ will cancel out and no current flows.

The phases can be described quantitatively by the rate of change of the area the bubble covers under the electrodes, $\frac{dA(t)}{dt}$. In phase 1 it is positive because overlap increases. In phase 2 it is negative because it decreases. In phase 3 overlap increases in the *top* electrode. Because we view the process from the perspective of the *bottom* electrode, $\frac{dA}{dt}$ must be negative in phase 3 and positive in phase 4. An alternative to this would be to view the second electrode as having a opposite polarity of surface charge. To integrate this fact, we define the system dry area rate of change, $\frac{dA(t)}{dt}$, as the dry area rate of change below the bottom electrode, minus the dry area rate of change below the top electrode,

$$\frac{dA(t)}{dt} = \frac{dA_{b1}(t)}{dt} - \frac{dA_{b2}(t)}{dt}. \tag{2.1}$$

From this, if there is no resistance on the wire between the electrodes, the conventional current from the higher electrode to the lower is at most

$$I(t) = \frac{dA(t)}{dt}\sigma, \tag{2.2}$$

where σ is the surface charge density on the FEP surface. In the other extreme, if the resistance between the electrodes is infinite, we see that an electric field and thereby a potential is created between the electrodes. In the next section we will attempt to quantify the potential between the electrodes for a situation where the load is of a finite nonzero value. This, in order to predict the current through the load.

2.2.2 Quantitative analysis

In order to predict the potential difference between the electrodes we must approximate their mutual capacitance. In the following discussion the capacitance associated with the EDL is not considered. As mentioned above, the Debye length of deionized water is on the order of 1µm, even shorter for regular fresh water. This can be viewed as the dielectric thickness of the capacitance associated with the EDL. The dielectric constant of water is approximately 80. Since permittivity is high and dielectric thickness is low, the EDL capacitance is expected to be several orders of magnitude larger than the electrode-water capacitance. The EDL capacitance is in series with the electrode-water capacitance. Because we

assume the much smaller electrode-water capacitance to dominate, we disregard the EDL capacitance from here on.

Figure 2.5 illustrates the geometry of the device viewed from the side, its electrical connections and capacitive couplings. First, we evaluate the different sources of capacitance.

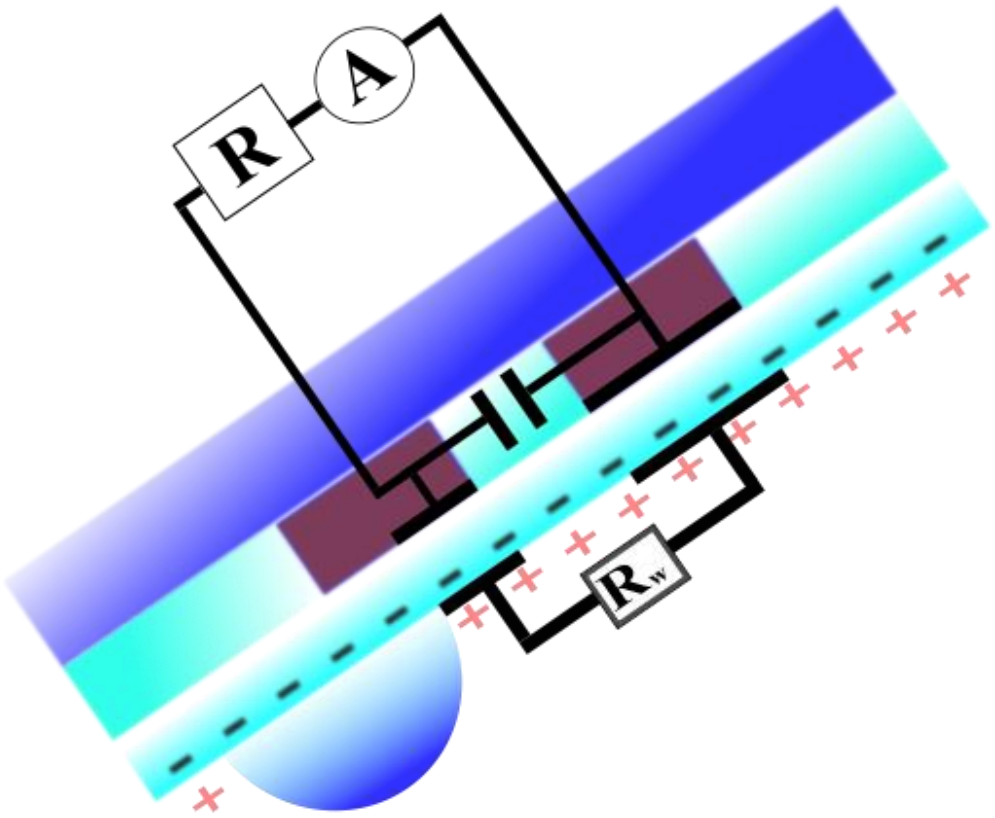

Figure 2.5: Construction of device and assumed capacitive connections. Acrylic substrate (dark blue) with imbedded electrodes (brown), covered by FEP. The electrodes are connected in series with a load resistor (R) and a picoampere meter (A). R_W is the resistance in the water between the electrodes. A bubble has started to displace the EDL in the left side of the device, effectively shrinking the mutual capacitance between the bottom electrode and the water underneath.

The electrode and the water body are separated by a dielectric sheet of FEP. If we consider the water body as a conductor, this resembles the basic construction of a parallel plate capacitor. Here, the plates are the electrode and the water in contact with the FEP surface. As we consider the water as a conductor, it will both constitute capacitor "plates" and connect the two electrode-water capacitors in series. This is shown by the black line in the lower part of figure 2.5.

As a bubble passes the electrode, the volume of water we have assumed acting as a capacitor "plate" will be disturbed. We assume this to decreases the effective "water plate" area and therefore the effective capacitance. This is illustrated in the left electrode in figure 2.5, where a bubble has partly overlapped. The area of the water "plate" will be

$$A_{W1}(t) = A_E - A_{b1}(t), \tag{2.3}$$

where A_E is the area of the electrode and A_{b1} is the area the bubble overlaps with the electrode. The area of the "water plate" will at most be the same area as the electrode. If a bubble covers the entire electrode the area of the "water plate" is zero. Because the thickness of FEP is much smaller than the width and length of the capacitor plates, we assume that edge effects are negligible, and the waterbody and electrodes can be regarded as infinite planes with homogenous charge distributions. If so, the mutual capacitance between one electrode and the water becomes

$$C_{E1/E2}(t) = \frac{A_{W1/W2}(t)\varepsilon_{FEP}}{d}, \tag{2.4}$$

where ε_{FEP} is the permittivity of FEP and d is the thickness of it. In this study, the thinnest FEP sheet used is 25 µm. Electrode area used is 1 by 4 cm. The relative permittivity of FEP is approximately 2 [46]. From this we expect the maximum magnitude of $C_{E1/E2}(t)$ to be 283 pF. For the thickest FEP sheet used in this study, 125 µm, the corresponding capacitance is 57 pF. From equation 2.4 we expect this capacitance to vary in the interval the electrode interacts with the bubble.

The electrodes will also have mutual capacitance directly between themselves. This is illustrated in figure 2.5 by the capacitor symbol between the electrodes. The space separating the electrodes is the interface between the acrylic substrate and FEP. If there is a potential difference between the electrodes, the field lines between them will pass through a mix of acrylic plastic, FEP and a variable mix of air and water. These are materials with relative permittivity ranging from close to 1 to around 80. We make a very rough order of magnitude estimate here and postulate that the parallel capacitance is constant at

$$C_p \approx \frac{80\varepsilon_0 A_E}{D} = 28 \times 10^{-12}\ F, \tag{2.5}$$

where D is the distance between the electrodes and ε_0 is the permittivity of vacuum.

The contribution of the electrode coupling with water above the device could also be considered. However, because the acrylic layer is 5 mm, about 3-4 orders of magnitude larger than the FEP thicknesses used, this capacitance is expected to be low compared with the electrode-FEP-water capacitance, and is therefore neglected from the discussion.

Next, recall the key assumptions made earlier:

1. There is at any time a one-to-one relationship between the amount of charge exposed under an electrode and the amount of charge induced in that electrode.
2. The induced charge in the electrode is the sum of,

   Type 1: Charge induced by internal redistribution of charge in the electrode.

Type 2: Charge induced by redistribution of charge between electrodes.

The second assumption can be formulated as

$$A(t)\sigma = Q_{I1}(t) + Q_{I2}(t), \tag{2.6}$$

where $A(t)$ is the dry area described in equation 2.1, $Q_{I1}(t)$ is the sum of type 1 induced charge in the electrodes and $Q_{I2}(t)$ is the sum of type 2 induced charge in the electrodes.

We assume that there is no source or sink of charge in the water body. We also disregard the resistance in the water and approximate it as an ideal conductor. This is based on the assumption that source impedance is high compared to the resistivity of the water. From this, the water body can be regarded as an isolated node. The current through $C_{E1}(t)$ must therefore be equal to the current through $C_{E2}(t)$ and we can therefore regard them as one capacitor, $C_s(t)$, with capacitance

$$\frac{1}{C_s(t)} = \frac{1}{C_{E1}(t)} + \frac{1}{C_{E2}(t)}, \tag{2.7}$$

where $C_s(t)$ is the total *serial* capacitance. Substituting 2.4 into 2.7 and rearranging we obtain

$$C_s(t) = \frac{\varepsilon_{FEP}}{d\left(\frac{1}{A_{W1}(t)} + \frac{1}{A_{W2}(t)}\right)}. \tag{2.8}$$

Observe that C_p and $C_s(t)$ are parallel and can therefore be added and viewed as one capacitance

$$C_{total}(t) = C_s(t) + C_p. \tag{2.9}$$

If type 1 induced charge is the same as the charge stored in the total mutual capacitance between the electrodes, the corresponding potential between the electrodes is

$$V(t) = \frac{Q_{I1}(t)}{C_{total}(t)}. \tag{2.10}$$

Because the type 2 induced charge in the bottom electrode by definition was transferred through the load, it can be expressed as the integral of the current through the load. By using ohms law to describe current in terms of the potential across the load and the resistance of the load, this can be written as

$$Q_{I2}(t) = \int_0^t \frac{V(t)}{R}\, dt. \tag{2.11}$$

By integrating 2.10 and 2.11 into 2.6 we obtain

$$C_{total}(t)V(t) + \int_0^t \frac{V(t)}{R}\, dt = A(t)\sigma. \tag{2.12}$$

The above assumptions are analogous to a current source in parallel to the load in figure 2.5. This current source has an output equal to $\frac{dA(t)}{dt}\sigma$, as stated in equation 2.2. The above discussion leads to the equivalent circuit shown in figure 2.6.

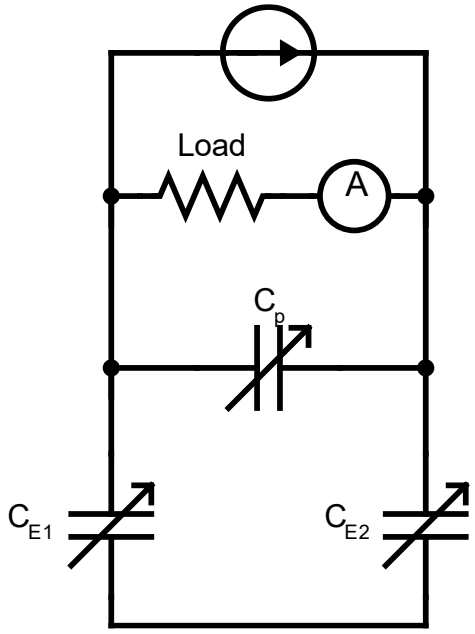

Figure 2.6: Equivalent circuit of model 1.

This describes the system proposed in figure 2.5 with one first order differential equation. This model relates the system voltage across the load resistor to the following parameters:

- The time dependent total capacitance. This is shown in equation 2.4, 2.5, and 2.7-9.
- The resistivity of the load.
- The surface charge density on the FEP surface.
- The rate at which air is displacing water below the electrodes.

2.2.3 Model of how the bubble displaces water under an electrode over time

From preliminary experiments, bubbles were observed to be sliding across the polymer surface in a roughly elliptical shape with an extension in the direction of movement of $1-2\ cm$ and a width of $3-4\ cm$. A picture of this can be seen in appendix 4. The duration of the current signal created when a bubble slid across the electrodes was approximately 0.18 seconds. Assuming that the current signal starts when the leading edge of the bubble reaches the first electrode, and stops when its trailing edge leaves the second electrode, the speed of the bubble was calculated to be $0.25\ ms^{-1}$ along the plane of the BMAT. We will attempt to approximate how these observed characteristics translates into the rate at which area under the electrodes overlaps with a bubble. The three-phase contact line the bubble, water, and polymer interface makes, is described as an elliptical shape, moving at a constant speed along the surface.

When an elliptical shape of width W_b and length l_b moves in the x-direction at a constant speed of v, the width, W, of the shape where it intersects with x = 0 at time t is

$$W_{x=0}(t) = W\sqrt{sin\left(\frac{t}{T_b}\pi\right)}, \tag{2.13}$$

where T_b is the time interval the bubble needs to travel one length of its body, $\frac{l_b}{v}$. Figure 2.7 illustrates how an elliptical bubble slides across two electrodes. By looking at the superposition of the bubbles positive areal change rate at its lower border (x = 0) and the negative areal change rate at its higher border ($x = l_e$), the total area rate of change for one electrode is obtained. Doing this for both electrodes we can calculate $\frac{dA(t)}{dt}$ resulting from an elliptical bubble sliding pass both electrodes. Recall equation 2.1 describing the definition of $\frac{dA(t)}{dt}$. A more detailed derivation of this can be found in appendix 2.

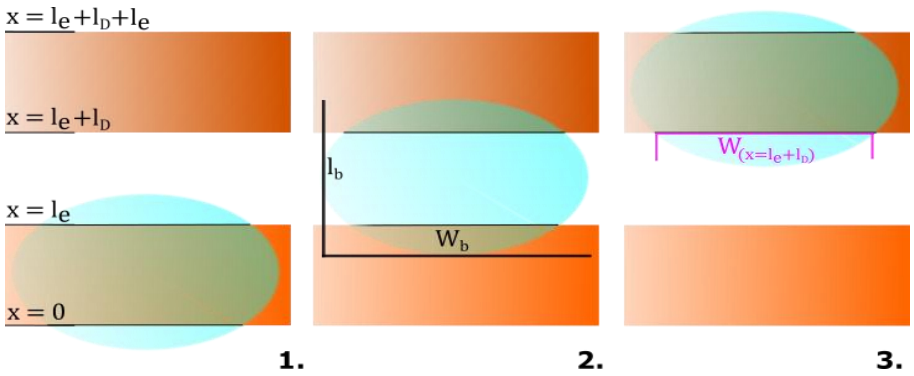

Figure 2.7: Illustration of an elliptical bubble of length l_b and width W_b, sliding across two electrodes. The width of the line where the bubble intersects with the lower or upper edge of an electrode, and the speed of the bubble determines how fast the area overlap between bubble and electrode increase or decrease. 1: The bubble is midway over the first electrode. In this instant the rate at which it slides off the electrode is equal to the rate at which it slides on. 2: The bubble is sliding off E_1 and

onto E_2 at the same time. 3: Same situation as in (1.) but for E_2. The magenta line shows the width of the bubble where it slides on to E_2.

The shape of the intersection between bubble, surface and water described by equation 2.13 is illustrated in figure 2.8. Here, the width of the shape is 3 cm and its length 1.5 cm.

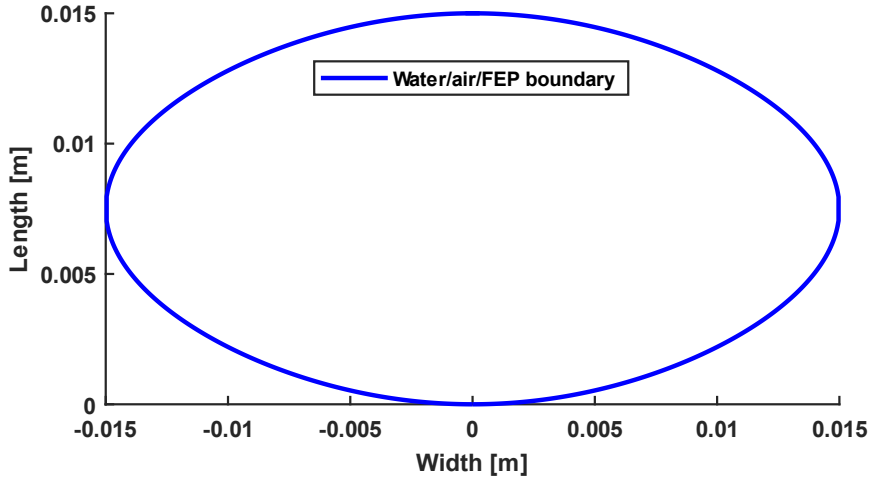

Figure 2.8: The bubble shape described by equation 3.15 when the width is 3 cm and the length is 1.5 cm.

For the BMAT device used in this work the electrode length is 1 cm, the electrode width is 4 cm, and the gap between the electrodes is 1 cm. Assuming the bubble travels along the surface at a constant speed of 0.25 m/s, we have the necessary parameters to do the calculations described above and in appendix 2. This is shown in figure 2.10. In the left panel of figure 2.10 we see the calculated areal overlap change for the bottom electrode (red) and the top electrode (green). We recognize here what was described descriptively in chapter 2.2.1. As the bubble slides onto the first electrode, it increases its overlap with it. When it has reached the state illustrated in the figure 2.7, part 1, its leading edge is sliding off the electrode at the same rate as its trailing edge is sliding onto the electrode. Therefore, the rate of area change is here zero. From there on the bubble slides off the bottom electrode, the area rate of change is now negative. We see that because we have modeled a bubble longer than the gap between the electrodes, the bubble starts to overlap with the top electrode before it has stopped interacting with the bottom electrode. Since the shape is assumed to be constant the area rate of change curve for the top electrode is an exact mirror image of the curve for the bottom electrode, only delayed in time.

Recall the discussion in 2.2.1 leading to equation 2.1. We argued here why the current in the outer circuit should be proportional to the area change rate in the bottom electrode minus the area rate change in the top electrode. This followed from defining positive current to be towards the bottom

electrode. This is shown in the right panel of figure 2.9. The blue curve in this plot is therefore representative for the short circuit current signal shape we expect from the ideal bubble described earlier in this chapter and in appendix 2.

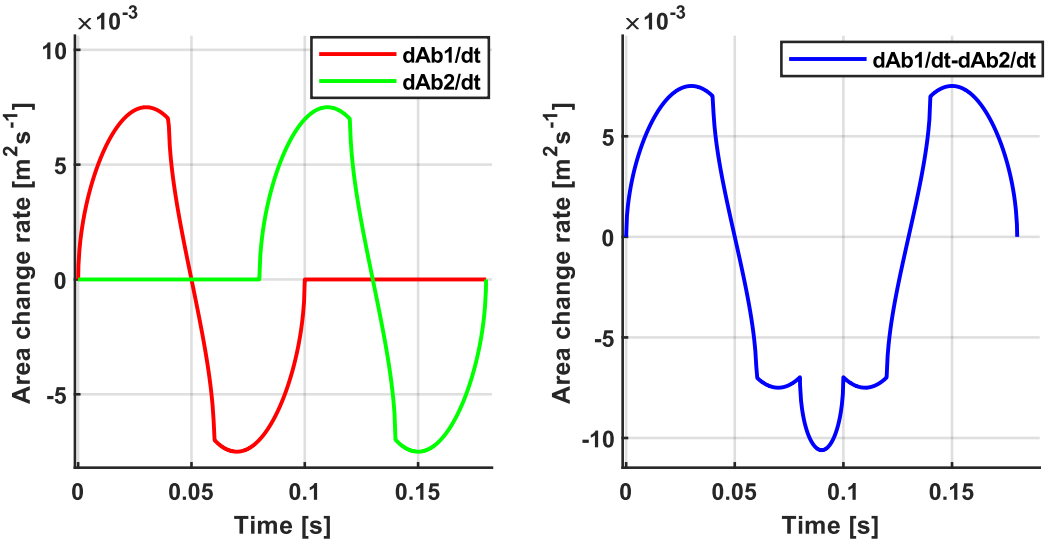

Figure 2.9: Left: Area covered by bubble rate of change under the bottom $\left(\frac{dA_{b1}(t)}{dt}\right)$ *and top* $\left(\frac{dA_{b2}(t)}{dt}\right)$ *electrode as the bubble depicted in figure 2.8 slides across the device in 0.25 m/s. Right: Total dry area rate of change as defined in equation 2.1, for the same bubble.*

Notice the strange looking negative pulse in the total area change rate, to the right in figure 2.9. This is the superposition of phase 2. and 3. discussed in chapter 2.2.1, yielding a peak negative area rate change of higher magnitude than the positive peaks.

3 EXPERIMENTAL SETUP

Four BMAT devices were made with four different thicknesses of FEP sheet. The devices were submerged in a water filled container and subjected to bubbles. Current between electrodes were measured and recorded on a computer.

3.1 DEVICE ASSEMBLY

The goal of the experiment was to see how the thickness of the FEP film effected device output under different resistive loads. Therefore, four devices were fabricated with different thicknesses of FEP. These devices were identical except for the FEP thickness. The polymer thickness used were 25, 50, 75 and 125 µm. The devices are denoted in the text by the thickness of the polymer in micro meters, "FEP25", "FEP50", and so on. Figure 3.1 shows how different materials were used to assemble the tested devices.

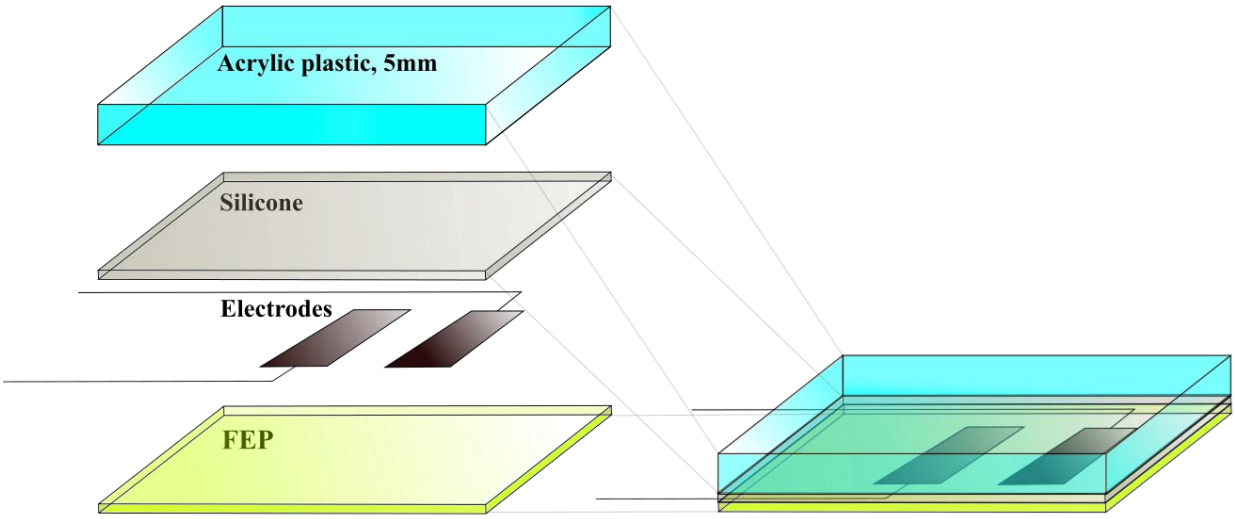

Figure 3.1: Illustration showing the constituent parts of the BMAT investigated. Acrylic plastic is used to insulate the electrodes and to be a rigid base for the device. Electrodes of copper with connected leads are imbedded between the acrylic plastic and a sheet of FEP. Silicon rubber ensures that water cannot leak in between the acrylic and FEP. The relative thickness of the FEP is greatly exaggerated in the illustration.

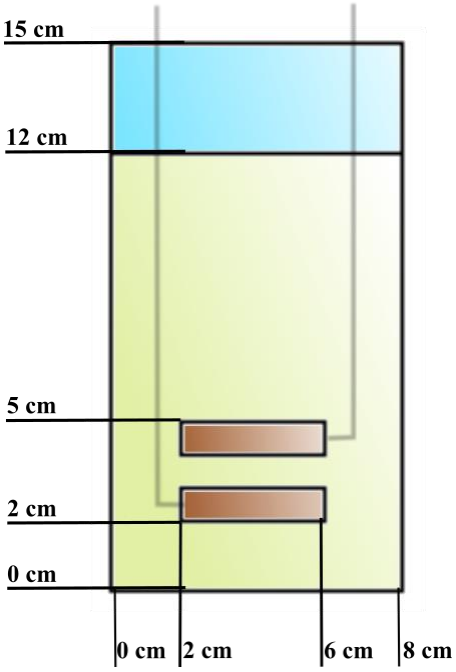

Figure 3.2: relative positioning of electrodes (brown), FEP sheet (green) and acrylic substrate (blue). The electrodes were 1 by 4 cm.

Copper tape was used as electrode material. The copper thickness was estimated to be $\sim 22\ \mu m$. Electrodes of 1 cm by 4 cm was cut out and carefully applied by hand with the adhesive side down to 8 cm by 12 cm FEP sheets. The electrodes were rubbed with cotton sticks from center and out to maximize contact and remove air between the copper and the FEP. Lead wires was connected to the backside of the electrodes with Kapton tape and conducting glue. Paint insulated 0.5 mm copper wire was used for this. Acrylic substrates of 8 cm by 15 cm and of 0.5 cm thickness were covered with an approximately 2 mm thick layer of uncured transparent wet-room construction silicon from Biltema. The FEP sheets with electrodes and leads were pressed against the uncured silicone with the electrode side facing the silicone, thereby imbedding them between the FEP and the acrylic substrate. The silicone was then allowed to cure. Figure 3.2 shows the geometry and dimensions of construction in the plane of the device.

The FEP surface was cleaned with ethanol and rinsed in deionized water before the experiments. As mentioned, four of these devices were made, all with different thicknesses of FEP sheet. The left side of figure 3.3 is a picture of copper electrodes after they have been adhered to a sheet of FEP. The right picture shows the four finished BMATs.

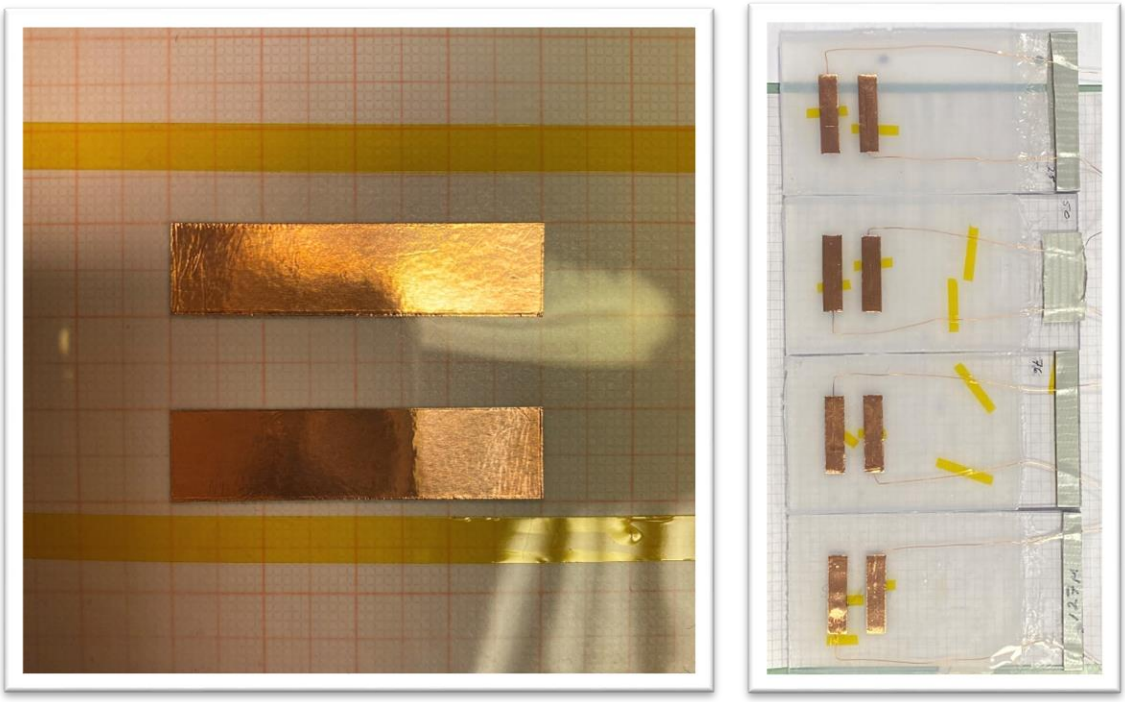

Figure 3.3: Left: Picture of FEP sheet after copper electrode have been adhered to its surface during assembly of devices. The background is millimeter paper. Right: Four test devices completed.

3.2 GENERAL SETUP

Figure 3.4 shows the experimental setup used throughout the experiment. A plastic container was filled with deionized water. An air pump provided a constant flow of air through a plastic pipe. The end of the plastic pipe was placed under the bottom part of the submerged device so that bubbles ejected from the pipe would slide across the entire FEP surface. A cardboard box was used to obtain a distance between the water container and the conducting laboratory bench. This was done to decrease unwanted capacitive connections. The positive terminal of the picoampere meter was connected to the bottom electrode via the resistor. The upper most electrode was connected to the negative terminal of the picoampere meter and to a conductive point in the laboratory table, illustrated by a grounding symbol in figure 3.4. This grounding of the negative terminal / top electrode gave a significantly better signal to noise ratio in the preliminary experiments. Therefore, it was used in the main experiments as well.

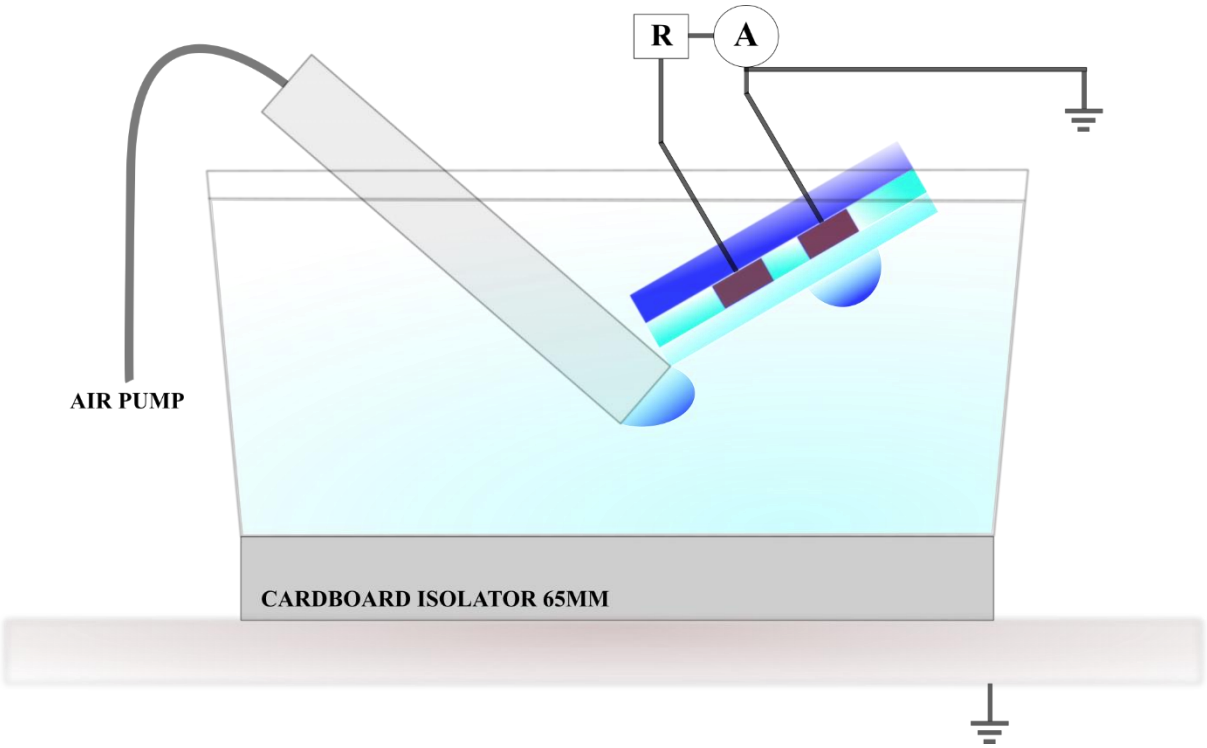

Figure 3.4: Illustration of experimental setup. Air is pumped into a plastic pipe. The opening of the pipe is placed under the bottom end of the submerged device. The top electrode is grounded to the laboratory table holding the setup. A carboard box is used to isolate the plastic container holding the water from the table.

A stable adjustable rig was used to hold the devices in the same relative position to the pipe, water surface, and container during all experiments. Figure 3.5 shows a picture of the experimental setup with a rig for holding devices, the water container, and the bubble generator. No changes were done to the rig position during the experiment between different devices. Therefore, the position of the different BMATs tested relative to the bubble ejecting pipe and water surface was not changed.

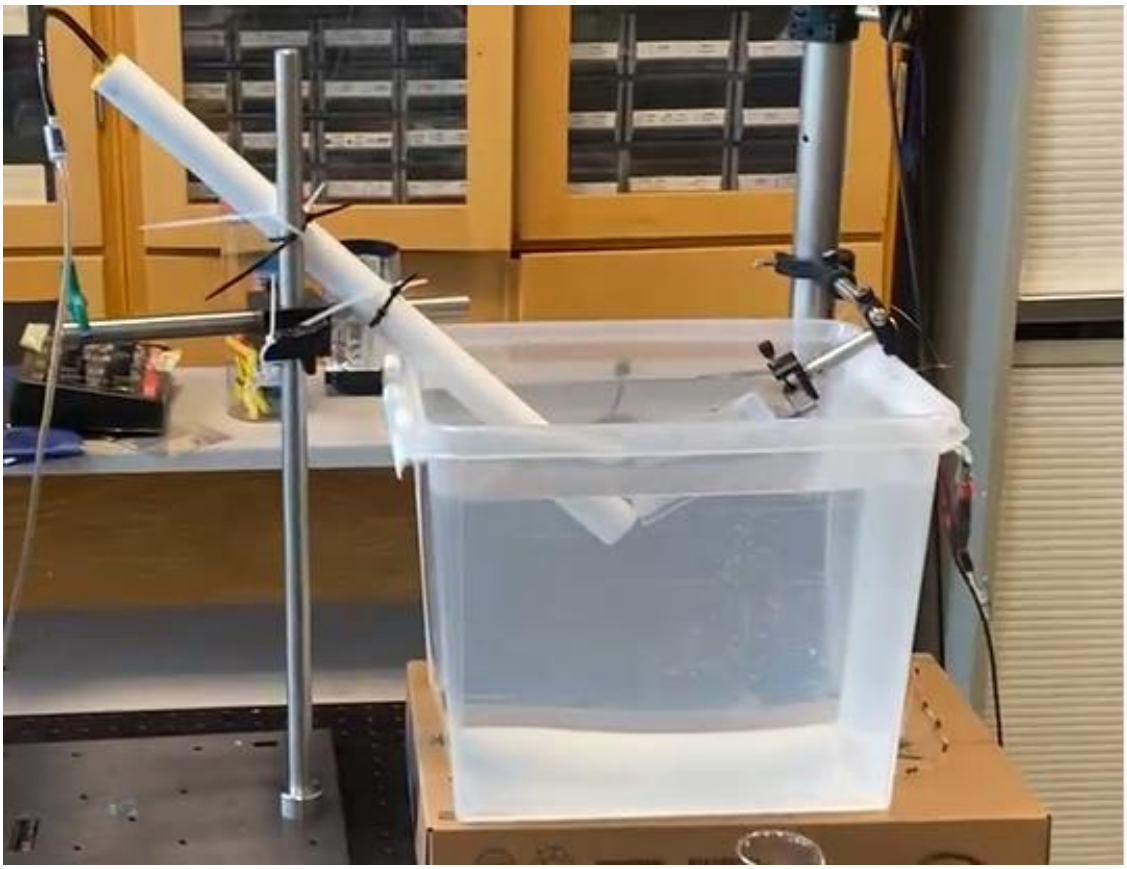

Figure 3.5: Picture of experimental setup. An apparatus for fixing the BMAT is seen to the right in the picture. The pipe with connection to the air-pump is seen to the left in the picture.

Figure 3.6 shows a picture of the device and air pipe submerged, depicted from the side through the transparent container. The device was fixed at an angle of $30° \pm 2°$ relative to the water surface. The same angle for the plastic pipe was $40° \pm 2°$. The depth of the highest part of the pipe opening was $5cm \pm 1cm$.

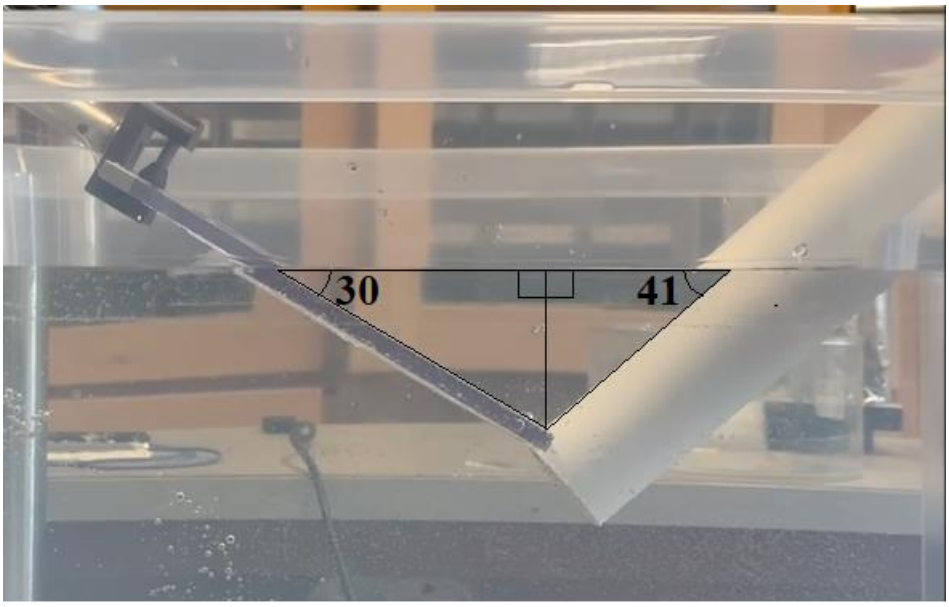

Figure 3.6: Picture showing the relative positioning of the test device and bubble generator to each other and the water surface.

The device angle and relative positioning of bubble generator was chosen on basis of observations done under preliminary experiments. It was observed that when the angle became too steep, the device stopped producing current. From visual observation it was assumed that this was due to the bubble not making sufficient contact with the FEP surface, sliding across it with a substantial wet layer between it and the surface.

3.3 PROCEDURE

The four devices were tested in short circuit, and under 0.5, 1, 2 and 3 GΩ of load. The reason for choosing to test the devices under such high loads was as follows.

If we in model 1 disregard the time variability of capacitance and the rate at which bubbles overlap with electrodes, it can be simplified and described as a first order system with a time constant of $\tau = RC$, where C is the characteristic total capacitance of the system and R is the load resistance. In this simplified view, it can be expected to see more variability in output when the duration of the input is comparable to the time constant of the system. Preliminary experiments showed that the time from zero to maximum overlap between electrode and bubble to be on the order of 10^{-2} seconds. We have assumed from the thickness of the FEP and the electrode area the capacitance of the electrodes to be on the order of 10^{-11} farads. This is shown in equation 2.4-2.8. Therefore, for the time constant of the system to be on the same order of magnitude as the duration of the input, R must be around $10^{9}\ \Omega$.

From every combination of FEP thickness and load resistance 600 seconds of data was collected. That is, 5 runs for every of the 4 different devices. In addition to this, FEP125 were run a second time for 0, 0.5 and 2 GΩ in the end of the experiment. This to identify potential drift in results due to potentially poorly controlled parameters. Every device was exposed to the bubbles for 10 minutes before data collection started. This was chosen because it was observed from preliminary experiments that output increased the first minutes of exposure and then stabilized. A table showing the order of experimental runs can be found in appendix 4.

3.4 THE TEST ENVIRONMENT AND DATA ACQUISITION

The devices were tested in a plastic container filled with 26 liters of deionized water. The temperature of the water increased from 23.7 to 24.1 Celsius during the time of the experiment (6 hours). The bubbles were generated by pumping air through a 40 mm polypropene tube into the water at an angle of $40° \pm 2°$ relative to the horizontal, and at a depth of $5cm \pm 1cm$. The position of the pipe and power settings on the air pump was kept constant during all experiment. Average bubble volume was measured by collecting 41 bubbles in an upside-down waterfilled beaker. In 30 seconds $80\ ml$ of air had accumulated in the beaker. Average volume per bubble is from this $1.95\ ml$, and frequency around 1.4 bubbles per second.

The instrumentation used was a Keithley 6485 picoampere meter connected to a computer with Logger Pro data collection software. The settings on the picoampere meter were set to “fast”, constituting an integration time of 0.1 power line cycles (PLC), corresponding to a reading rate of 500 samples per second with a 50hz power line. The range used was 2µA. The data collection settings in the software were set to 1000 samples per second.

Equipment used:

- Millipore Milli-Di, > 1MΩ @ 25 °C water deionizer.
- ALEAS air pump, AP-2888
- Keithley 6485 Pico amperemeter
- Vernier, LabQuest Mini
- Computer with Logger Pro software
- Resistors, 500 MΩ, tolerance of ± 2% , KOA.

3.5 PROCEDURE OF CALCULATIONS

Current

It was assumed that any net current measured over many signal cycles must have been due to a bias error in the meter and not a physical net current. The electrodes are insulated from each other, therefore the net current over time must be zero. The average bias current was calculated as the net cumulated charge divided by data collection time,

$$\bar{I}_{bias} = \frac{1}{T}\sum_{0}^{\frac{T}{\Delta t}} I(i)\Delta t, \tag{3.1}$$

where T is the duration of the dataset (600 seconds) and Δt is the measurement interval. The bias current was subtracted from the data before presentation or further analyses.

Average peak current for the first pulse

As one bubble passed the device a signal of three pulses was measured. The middle pulse was negative and the first and third positive. This is referred to as a signal triplet in the text. The average current peak heights for the first pulse in the triplet was calculated by manually reading the maximum value of the first pulse in the last 50 signal triplets in each data set and dividing by 50.

Charge

Before current data was used to calculate charge or energy, it was filtered by a moving average of 0.02 seconds to reduce the contribution of noise. Cumulative charge transferred was then calculated as

$$q(n) = \sum_{0}^{n} \left| I_{filtered}(i) \times \Delta t \right|, \tag{3.2}$$

where Δt is the interval of individual current measurements (1 millisecond) and $I_{filtered}$ is the measured current applied the running mean described above. The average charge transferred per bubble was calculated by choosing a time interval and dividing the cumulative charge by the number of bubbles that passed the device in that interval. This was done for the 10 last bubbles in each dataset, where one dataset contains the data for one FEP-load combination. An example of a FEP-load combination is FEP127 under 1GΩ. The variance of charge per bubble was obtained by dividing the interval into subintervals, each containing the accumulated charge from the passing of a single bubble.

Energy

Instantaneous power was calculated as the product of filtered current squared and load resistance,

$$p(i) = {I_{filter}}^2(i)R. \tag{3.3}$$

The average energy dissipated between two discrete measurements is then $p(i) \times \Delta t$, where Δt is the time between measurements (0.001 seconds).

Cumulated energy dissipated in load for n measurements was then calculated as the cumulative sum of this energy,

$$E(n) = \sum_{0}^{n} p(i) \times \Delta t. \tag{3.4}$$

Mean energy per bubble was then calculated by dividing the cumulated energy from a time interval by the number of bubbles that passed the electrodes in that interval. The variance was obtained by dividing the interval into subintervals, each containing the cumulative energy from the passing of a single bubble. In that way their individual contributions to energy were obtained. The ten last bubbles in each data set were used for this.

Time

In order to evaluate system time response, the average duration of the first pulse in the signal triplet was measured. To obtain this, the duration of the ten last peaks in each data set were measured semi-automatically in Logger Pro using the cursor and selecting the interval. The pulse is measured from the point where the current signal exceeds the noise level, to where it first reaches zero again after the peak. The uncertainty associated with the human factor in this method is quantified in appendix 1.

4 RESULTS

The four BMAT devices were subjected to bubbles and tested under different resistive loads. The current through this load was measured. In the first part of this chapter the results from these measurements are presented. In the second part, the theoretical model of the system is used to attempt to replicate the measurements by numerical simulation. All data presented with error bars indicate two standard deviations of estimated standard uncertainty, unless otherwise is clearly stated.

4.1 CURRENT, CHARGE AND ENERGY

For each FEP and load resistance combination, 600 seconds of data was collected. In these 600 seconds the devices where exposed to about 1.4 bubbles passing per second. Figure 4.1 zooms in on the time axis to show a representative example of the current signal shape generated as a single bubble passes the electrodes. The different subplots show how current signal shape varies with FEP thickness (left to right) and load resistance (top to bottom). A running mean of 10 datapoints is applied to reduce noise.

In short circuit the current signal consisted of three pulses. A positive followed by a negative, and at last a positive pulse. In theory we expected the signal to be symmetric. Recall equation 2.2, describing the idealized short circuit current. However, a symmetric current signal was not observed, as the last pulse was significantly smaller than the first.

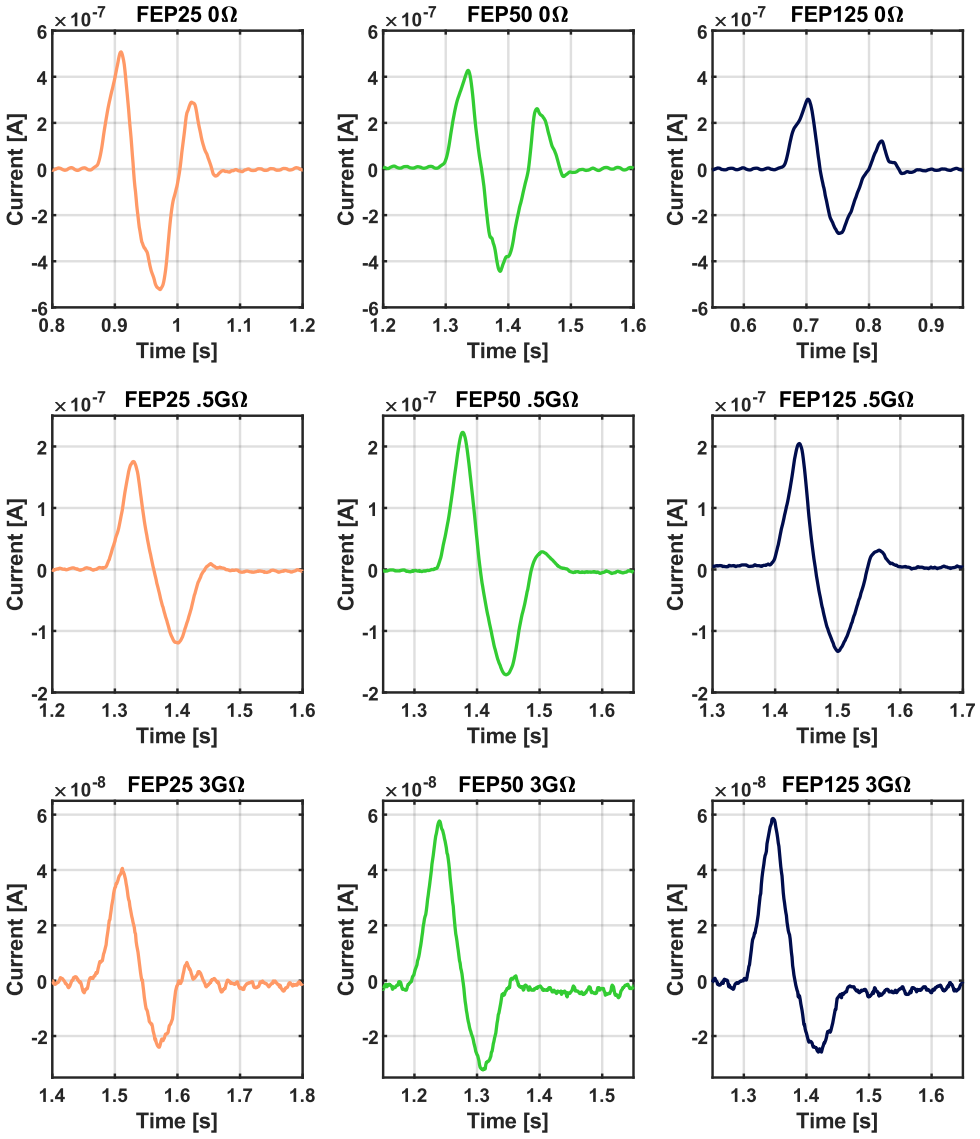

Figure 4.1: Examples of current signal shape created as a single bubble passes FEP25 (left column), FEP50 (middle column) and FEP125 (right column) under short circuit (top row), 0.5GΩ (middle row) and 3 GΩ (bottom row) load resistance. A running mean of 0.01 seconds (10 datapoints) is applied to reduce noise.

Figure 4.2 shows the full raw data for each polymer thickness superimposed for easy comparison of current peak magnitude. The left graph displays current under short circuit. The middle graph displays the current with a load resistance of 0.5 GΩ. FEP25 peak current magnitude is lowest. FEP50 and FEP76 are about equal and highest. The FEP25 current peak magnitude clearly suffers the most from the increase in load resistance. The right graph shows the current under a load of 3 GΩ. Current drops further, about one order of magnitude down from the short circuit measurements. The limitations of the data resolution are visible here. The resolution of the data collected was $3 \times 10^{-9} A$. See appendix 1 for details on uncertainty.

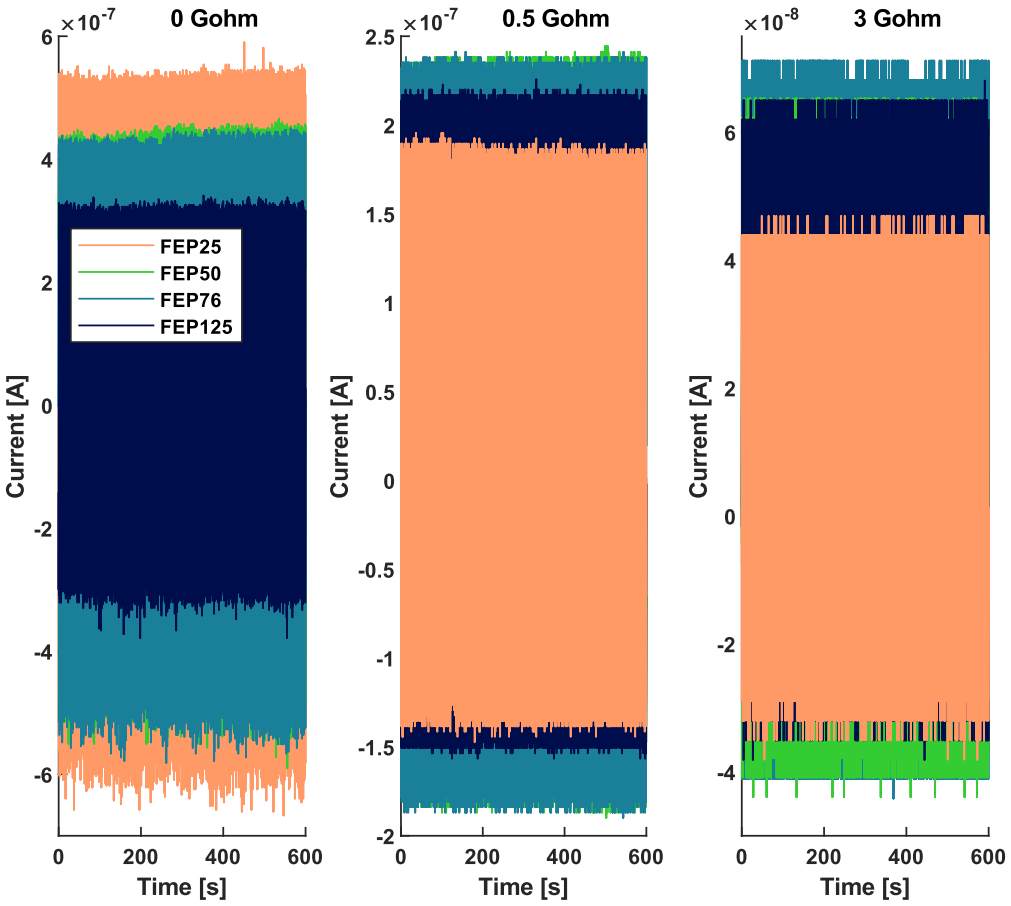

Figure 4.2: The 600 seconds of collected current data for different FEP thicknesses superimposed for comparison. Left: Short circuit. Middle: 0.5 GΩ load resistance. Right: 3 GΩ load resistance. No filtering applied.

4.1.1 Charge per bubble

Figure 4.3 shows the average charge transferred through the amperemeter per bubble under short circuit. Here, it is referred to the integral of the absolute value of the current. That is, the total area under the current curve from the passing of one bubble, illustrated by the orange area marked in the left panels of figure 4.3. This was obtained by first calculating the cumulative absolute value of the current data. This is shown in equation 3.2. Then, the interval containing the 10 last bubbles of each dataset was used to obtain average charge transferred per bubble. See chapter 3.5 for procedure of calculations.

When subjecting the different devices to bubbles under short circuit it was observed that charge transferred per bubble increases with decreasing thickness of FEP. Charge transferred for FEP125 is nearly half of FEP25.

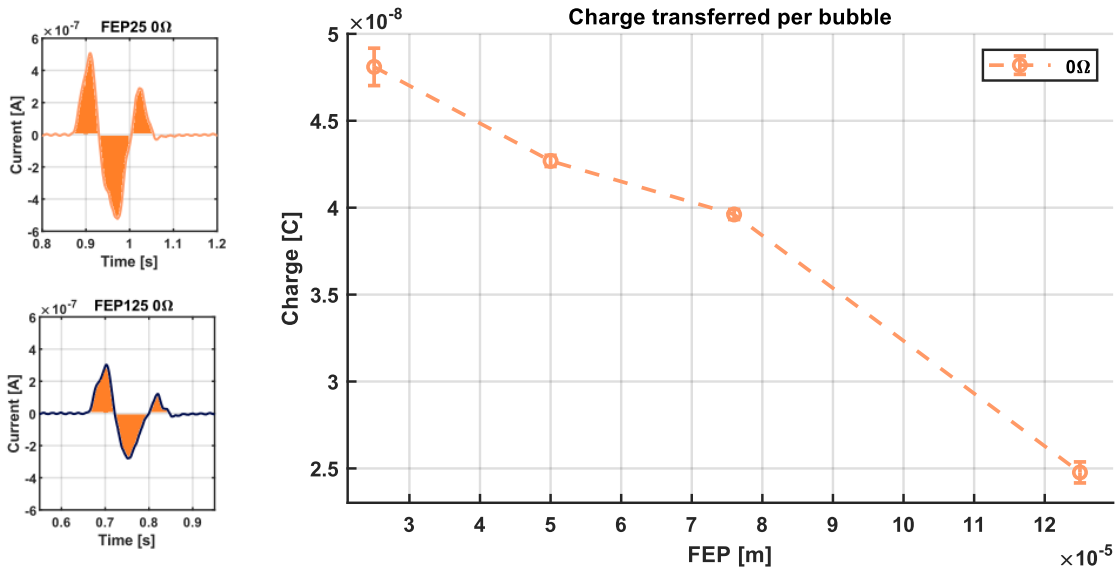

Figure 4.3: Left: Charge per bubble is here defined as the total area under the current curve from the passing of one bubble, here illustrated by coloring the area orange. Right: Average charge transferred through meter in short circuit per bubble versus FEP thickness. Uncertainty is due to uncertainty of the mean and inherent uncertainty in the measurements.

Consider the optimal situation based on the four phases described in chapter 2.2.1:

1. The bubble overlaps 100% with E_1. A charge, σA_e is transferred from E_2 to E_1 in order to screen the corresponding exposed charge on the FEP surface.
2. The bubble slides off E_1. The same charge is transferred back to E_2.
3. The bubble overlaps 100% with E_2. A charge, σA_e is transferred from E_1 to E_2 in order to screen the corresponding exposed charge on the FEP surface.
4. The bubble slides off E_2. The same charge is transferred back to E_1.

The maximum amount of charge that has passed through the ampere meter between the electrodes during these phases is therefore $4\sigma A_e$. Because this is the theoretical optimal amount of charge transferred per bubble passing the device, we can infer from measured charge transferred per bubble that surface charge density is

$$\sigma > \frac{Measured\ charge\ transferred\ per\ bubble}{4A_e}, \tag{4.1}$$

where A_e is the electrode area. This is the minimum surface charge density because it accounts for a bubble which perfectly covers the entire electrode area, perfectly unscreens the static field and perfectly transfers the same amount of charge through the meter. If this was the case, the same amount of charge should be transferred in phase 1 as in phase 4. Therefore, a symmetric current signal would be measured, where the first and third pulse magnitude was equal. It can be seen in the three upper subplots of figure 4.1 that this is not the case. From the measured charge in figure 4.3 and equation 4.1

we expect FEP125 to have a surface charge density larger than 15 μCm^2 and FEP25 to have a surface charge density larger than 30 μCm^{-2}.

When a load was connected in series with the electrodes and the picoampere meter, the charge measured through the meter per bubble did not follow the same pattern as under short circuit. FEP25 generated the least amount of charge through the load for all loads. For all loads, FEP50 or FEP76 yielded highest charge. Figure 4.4 displays average charge transferred through the load between electrodes per bubble subjected to the device. Charge is here measured in the exact same way as described for figure 4.3.

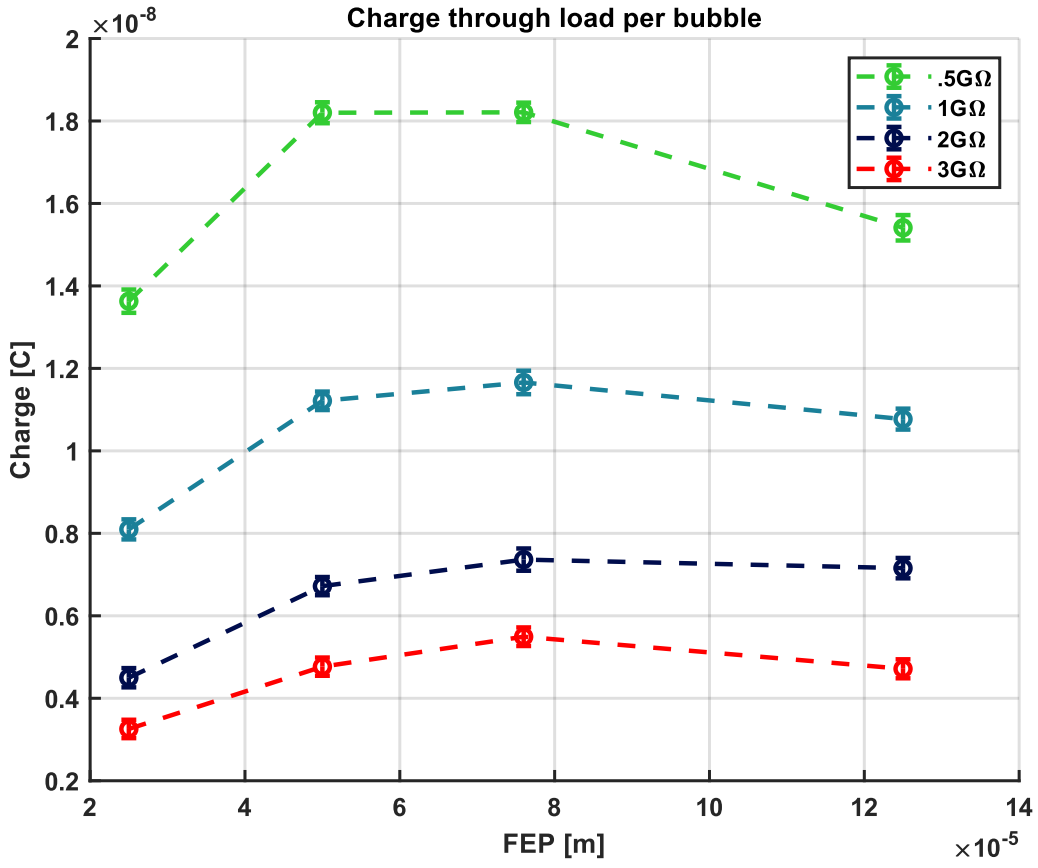

Figure 4.4: Average charge transferred through load per bubble passing device versus FEP thickness. Uncertainty due to uncertainty of mean and inherent uncertainty in measurements.

4.1.2 Energy per bubble

The average energy generated per bubble passing the devices was calculated from the current data. Figure 4.5 shows the average energy dissipated in the load per bubble passing the device based on the 10 last bubbles in each dataset. Energy yield per bubble increases with decreasing load resistance for the resistances used. This indicates that the load for which the largest amount of energy is transduced is somewhere in the interval from 0 to 1 GΩ for all FEP thicknesses.

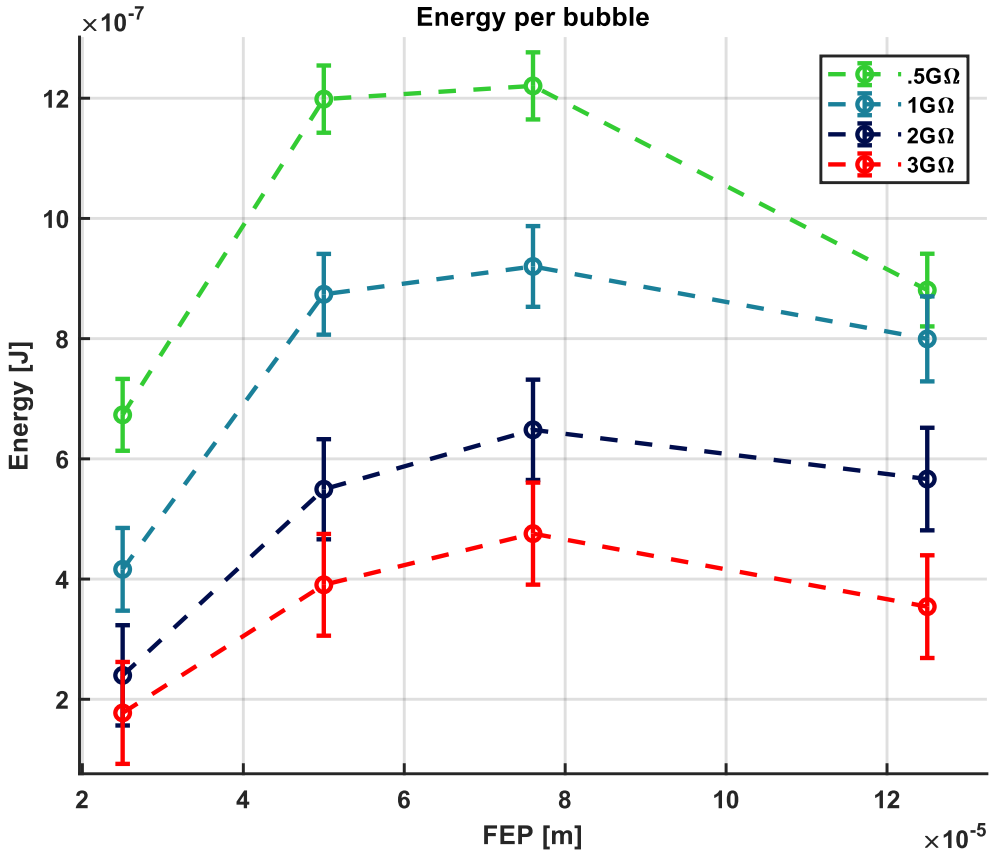

Figure 4.5: Average energy dissipated in load per bubble passing versus FEP thickness. Different colors represent different load resistances. Uncertainty due to resistor tolerance, current measurement and uncertainty of the mean.

4.1.3 Peak current and power of the first pulse in the signal triplet

The average peak current (left panel) and corresponding average peak power (right panel) in the first pulse in the signal triplet is presented in figure 4.6. This was obtained by averaging the maximum current for the first pulse of the 50 last signal triplets for each data set. There was no filtering of the raw data applied in advance to this, which is reflected in the error bars. The instantaneous power is calculated as $p = {I_{MAX}}^2 R$, where I_{MAX} is the measured peak current and R is the resistance of the load.

The highest mean peak current is for FEP25 under short circuit. It is approximately $5.25 \times 10^{-7} A$, translating to a peak current density of approximately $1.31 \times 10^{-3} A/m^2$. We see that for all loads

FEP25 yields the lowest peak power. The maximum power is obtained by FEP50 under 0.5GΩ load, reaching roughly $2.8 \times 10^{-5} W$. This corresponds to a power area density of $0.07\ W/m^2$. Here, the area current and power density is calculated relative to the area of one electrode. As can be seen in the right panel of figure 4.6, measurement uncertainty is high.

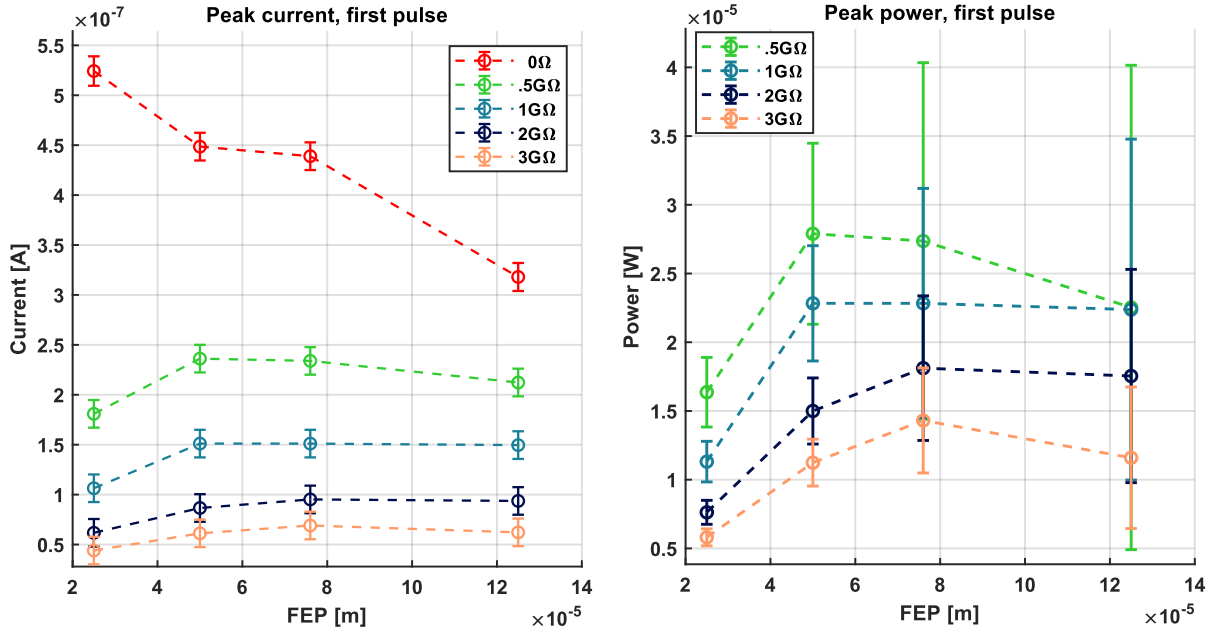

Figure 4.6: Average peak current of first pulse in triplet (left panel) and corresponding average peak power (right panel). Data collected from the last 50 signal triplets in each dataset.

4.1.4 Duration of charge transfer of the first pulse in the signal triplet

In order to evaluate the system time response, the mean duration of the first pulse in the signal triplet was measured. To obtain this, the duration of the ten last peaks in each data set were measured semi-automatically in Logger Pro using the cursor and selecting the interval. The pulse was measured from the point where the current signal exceeds the noise level, to where it first reaches zero again after the peak. The duration of positive current for the first triplet pulse versus FEP thickness is displayed in figure 4.7. Be aware that error bars in this plot is only one standard deviation to make it readable. The high uncertainty is due to the semi-automatic method of measuring. This is described in more detail in appendix 1. The duration dependency on resistance is clear. As resistance increases so do the duration of the first pulse.

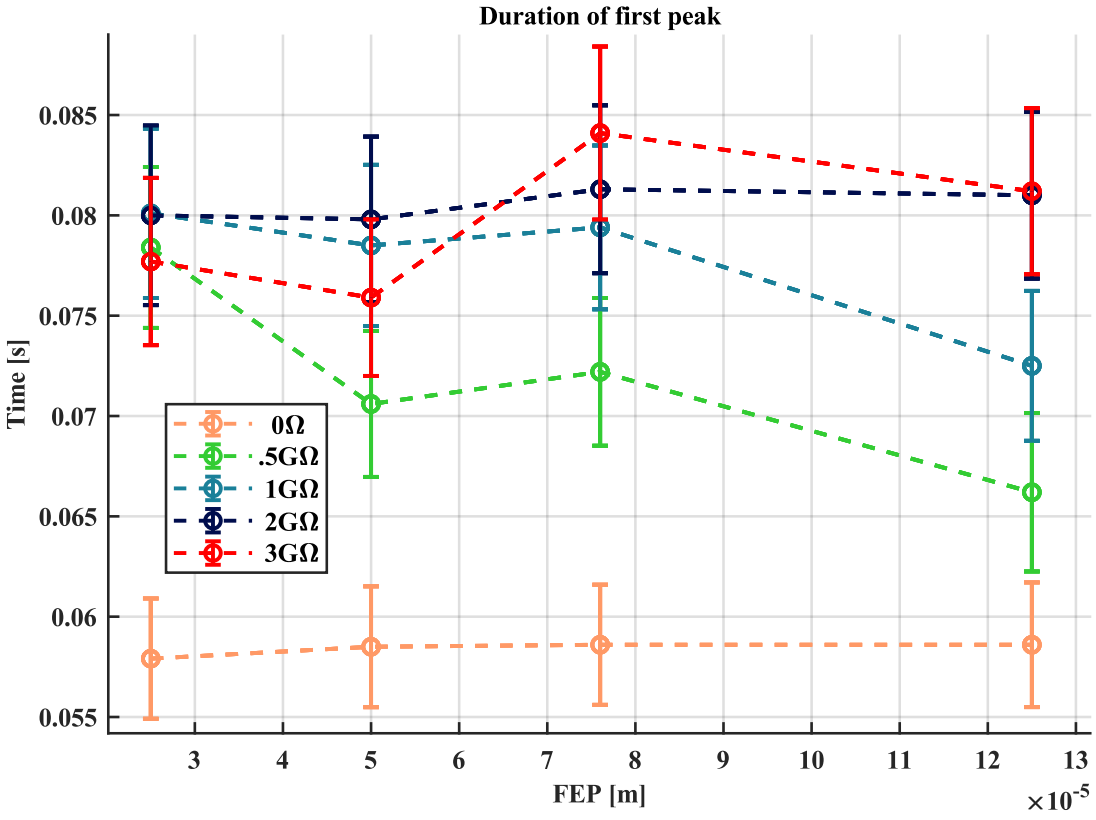

Figure 4.7: Mean total duration of first peak in triplet. Error bars are here only one standard deviation of uncertainty.

4.2 SIMULATION

In describing the BMAT in chapter 2, no assumptions were made on if or how thickness might affect surface charge density. The data on charge transferred in short circuit displayed in figure 4.3 shows that as FEP thickness was increased, the charge transferred per bubble decreased. In the view of equation 2.2 this can be interpreted as a direct consequence of thinner FEP holding a higher effective surface charge density than thicker FEP. It is important to mind that this suggestion rests on the assumption that our theoretical description is valid. The surface charge density parameter used in simulation can be calibrated to reflect this. We assume here that the relative difference between devices in how much charge was transferred in short circuit, is the same as the relative difference in effective surface charge density between devices. For example, because FEP25 transferred roughly twice as much charge per bubble as FEP125, it is assumed that the effective surface charge density of FEP25 is roughly twice that of FEP125. From this we obtain a relative relationship between FEP surface charge densities for different FEP thicknesses as displayed in table 4.1. The effective charge density of FEP125 is chosen for relative comparison.

Thickness [μm]	**Charge transferred per bubble in short circuit. [C]**	**Effective charge density relative to FEP125, [σ/σ_{FEP125}]**
FEP25	4.81×10^{-8}	1.94
FEP50	4.27×10^{-8}	1.72
FEP76	3.96×10^{-8}	1.60
FEP125	2.48×10^{-8}	1.00

Table 4.1: Adjusted relative surface charge density between different FEP thicknesses based on assumption that charge transferred under short circuit conditions is proportional to effective surface charge density on the FEP surface.

The relative relationship of surface charge density proposed in table 4.1 is used in all simulations. In addition to the relative relationship between surface charge density between thicknesses, the magnitude must be chosen in simulations. The surface charge density of submerged or alternatingly submerged FEP can be expected to be on the order of 10 μC/m^2 [19]. Zhu et al. operated with an assumption of charge density of their nanostructured FEP surface employed in experiments with water waves to be approximately 42 μC/m^2 [17]. In the following simulations the magnitude of the surface charge density parameter was adjusted by trial and error to obtain an approximate best-fit with the measured data. The approximate best fit was found when FEP125 had a surface charge density of $30\mu Cm^{-2}$, which is realistic based on previous reports [17, 19].

In connecting the negative terminal of the picoampere meter to a conducting part of the laboratory bench, the signal to noise ratio improved by more than one order of magnitude. However, the setup may have created a significant capacitive connection between the water body and the upper electrode through the table and other conducting equipment in contact with it. This was to some degree countered by placing the water container on top of a cardboard box, creating a distance between it and the conducting table. This can be seen in figure 3.4. However, because of unexpected attributes of the measured current signal shape, it was suspected that this connection was significant despite measures to decrease it. Therefore, it might have had an important influence on the measured current. The capacitive connection described is from here on denoted C_{GROUND} in order to distinguish it from the other capacitive connections discussed earlier. In the following simulation the possible effect of this is evaluated. Simulation is done both with and without accounting for C_{GROUND}.

In the simulation of model 1, C_{GROUND} is assumed to be very large compared to $C_{E2}(t)$. In this manner it can be approximated in the equivalent circuit of model 1 as a conductor parallel to $C_{E2}(t)$. The zero-resistance path this creates around $C_{E2}(t)$ results in the $C_s(t)$ to be equal to $C_{E1}(t)$.

The model was simulated numerically in MATLAB in order to see if it reflected any of the results displayed so far. This was done with the assumption of device specific relative FEP surface charge density, as shown in table 4.1. The system response was simulated with and without C_{GROUND}. The model results are referred to as M1 and M1*, where the latter denotes the model results when considering C_{GROUND}. As mentioned, FEP125 surface charge density was adjusted for rough fitting. It was set to 30 μC/m^2 for all of the following simulations of model 1. All other model parameters are based on the analytical assumptions and calculations discussed in chapter 2, and visual observations of the bubble geometry. In simulating short circuit current, a low load resistivity of 1MΩ was used in the MATLAB program. This was done because the crude time resolution used resulted in high model error when resistivity was set low. The simulation results under 1MΩ load are assumed to be representative for the short circuit measurements because, preliminary experiments hardly showed an observable decline in current output after a load of this magnitude was connected, suggesting that the BMAT is a high impedance source.

The current signal from the passing of one bubble was simulated by solving equation 2.12 numerically in MATLAB, obtaining the voltage across the load over time. Ohms law was used to find the current through the load from this. Figure 4.8-10 shows the simulated current signal together with the measured current signal. Figure 4.11-13 compares simulation results with measured average charge transferred through load per bubble, average peak current in first pulse, and average duration of the first current pulse in the signal triplet. The parameters used in the simulations were as stated in table 4.2.

Parameters	***M1****	***M1***
Surface charge density FEP 125, $[Cm^{-2}]$	30×10^{-6}	30×10^{-6}
Surface charge density FEP 76, $[Cm^{-2}]$	48×10^{-6}	48×10^{-6}
Surface charge density FEP 50, $[Cm^{-2}]$	52×10^{-6}	52×10^{-6}
Surface charge density FEP 25, $[Cm^{-2}]$	58×10^{-6}	58×10^{-6}
W_E, electrode width, [m]	0.04	0.04
l_E, electrode length, [m]	0.01	0.01
W_b, bubble width, [m]	0.03	0.03
l_b, bubble length, [m]	0.015	0.015
Bubble speed, [m/s]	0.25	0.25
C_{GROUND}, [F]	∞	0
C_p, [F]	28.32×10^{-12}	28.32×10^{-12}
$C_s(t)$, serial capacitance, [F]	$C_s = \frac{A_{w1}\varepsilon_{FEP}}{d}$	$\frac{1}{C_s(t)} = \frac{1}{C_{E1}(t)} + \frac{1}{C_{E2}(t)}$
Time resolution, [s]	1.88×10^{-6}	1.88×10^{-6}
Bubble shape (Shape of three-phase line of air, water and FEP surface.)	Elliptical, as described by equation 2.14, chapter 2.23 and appendix 2.	Elliptical, as described by equation 2.14, chapter 2.23 and appendix 2.

Table 4.2: Model parameters used when deriving results displayed. M1 denotes the model as described in chapter 2. M1 denotes the model when taking into account the effect of C_{GROUND}.*

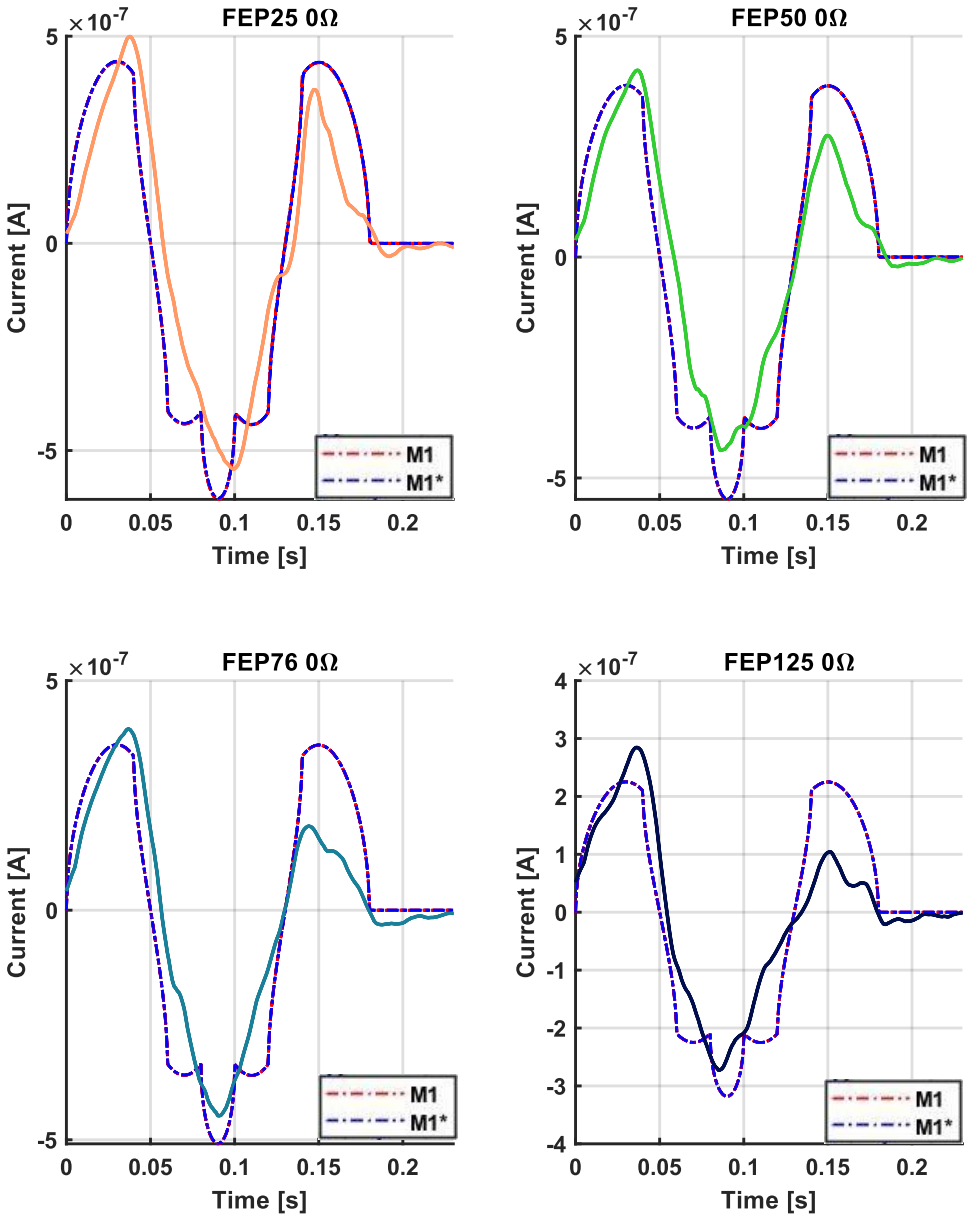

Figure 4.8: Comparison between measured current signal and simulated current signal in short circuit for FEP25 (top left), FEP50 (top right), FEP76 (bottom left), and FEP125 (bottom right). The simulated current signal without accounting C_{GROUND} is denoted M1. The simulated current signal accounting for C_{GROUND} is denoted M1. Parameters used in the simulation is given in table 4.2. The measured current signal is applied a running mean of 0.01 seconds to reduce noise.*

In figure 4.8 we see how the model predicts the current signal from the different devices with no load between the electrodes. Bear in mind that the surface charge density parameter used in the model is calibrated from this data. Therefore, the fact that the model seems to replicate approximately the relative difference in signal magnitude between the different devices is expected. Both M1 and M1* predicts a perfectly symmetrical signal, the first and third peaks being mirror images of each other.

This is not observed in the measurements. Calculating the average ratio of the first to the third current pulse magnitude in the measured data we obtain table 4.3. That is, the peak height of the first pulse divided by the peak height of the third pulse. The average is based on the five last signal triplets in the measurements.

	FEP25, 0 Ω	**FEP50, 0 Ω**	**FEP76, 0 Ω**	**FEP125, 0 Ω**
Ratio 1.peak/3.peak	1.74 ± 0.16	1.67 ± 0.13	2.19 ± 0.15	2.91 ± 0.24

Table 4.3: Mean ratio of first to third pulse in short circuit measurement. Average based on the five last signal triplets for each filtered dataset. The uncertainty in the average is purely statistical with confidence of 95%.

Looking at table 4.3 it is clear that the symmetrical signal predicted by M1 and M1* is not observed in measurements. Therefore, this is a qualitative attribute of the signal that the model to no degree replicates. In figure 4.9 measured current signal and simulated current signal under 0.5 GΩ of load is compared.

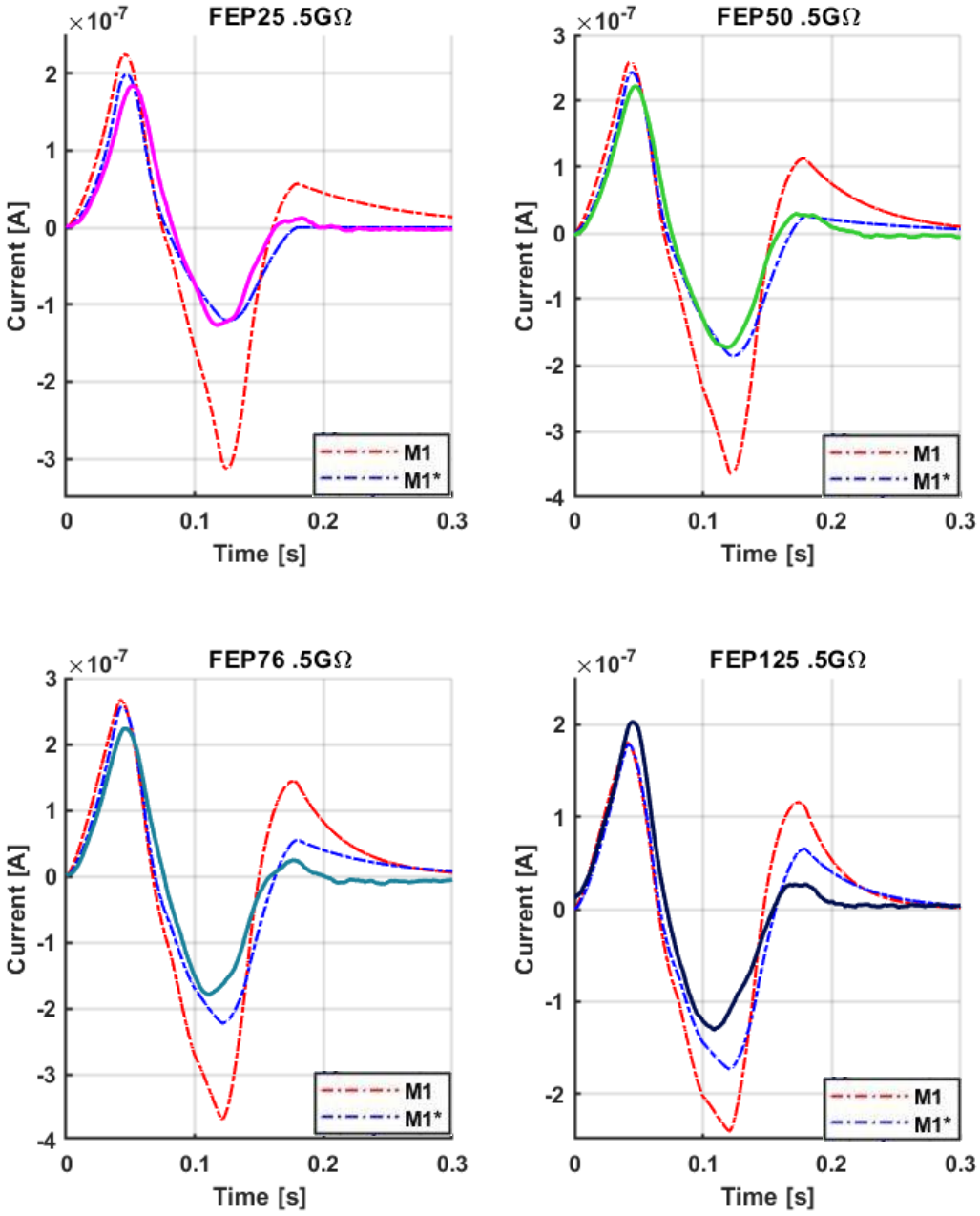

Figure 4.9: Comparison between measured current signal and simulated current signal under 0.5 GΩ of load for FEP25 (top left), FEP50 (top right), FEP76 (bottom left), and FEP125 (bottom right). The simulated current signal without considering C_{GROUND} is denoted M1. The simulated current signal accounting for C_{GROUND} is denoted M1. Parameters used in the simulation is given in table 4.2. The measured current signal is applied a running mean of 0.01 seconds to reduce noise.*

In figure 4.9 and 4.10 we see how the model simulates the current signal from the different devices with respectively 0.5 GΩ and 3 GΩ of load between the electrodes. Qualitative conformity between the measured signal and M1* is visibly better than between measured signal and M1. That is, at high load the model better reflects the measured signal when accounting for C_{GROUND}.

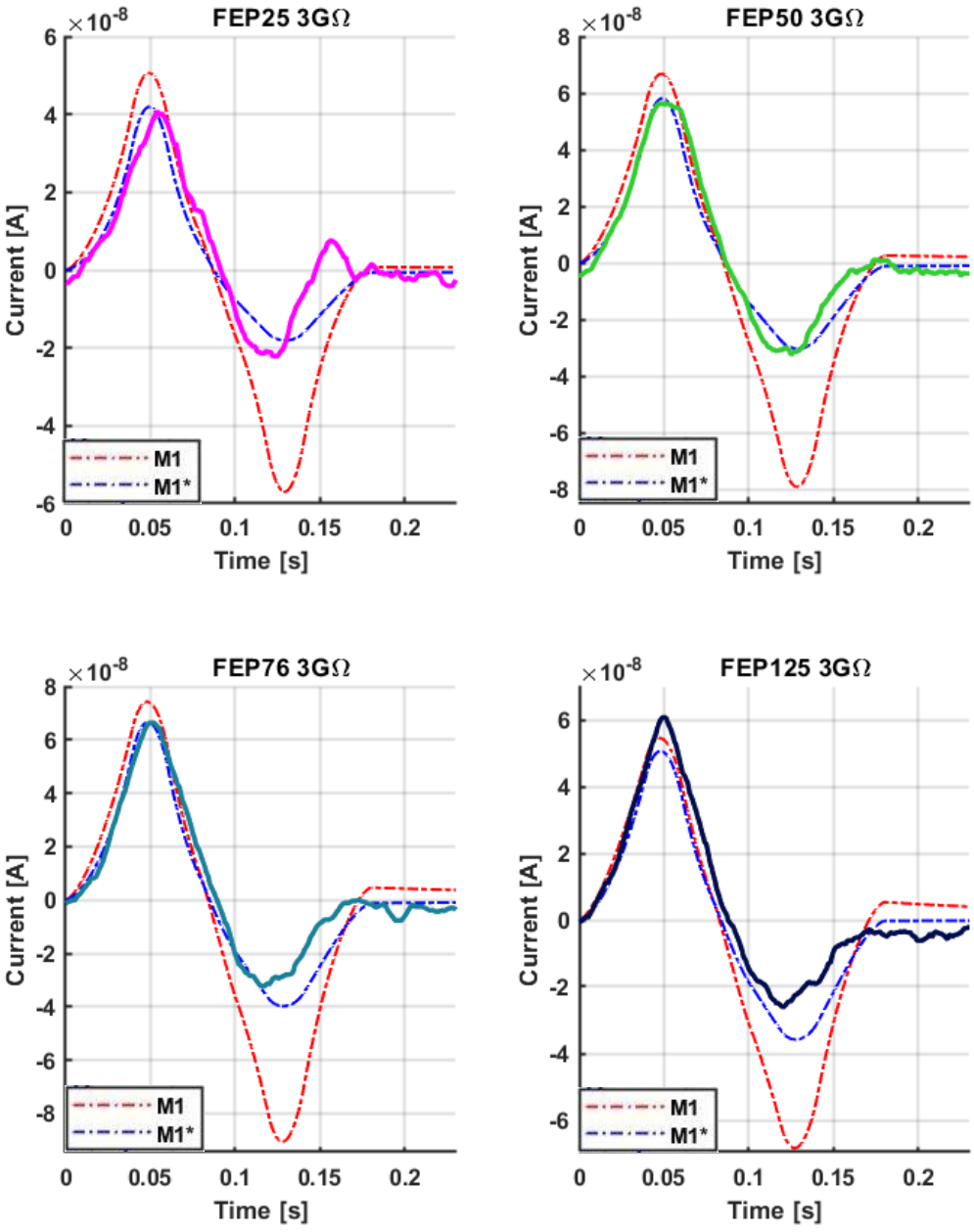

Figure 4.10: Comparison between measured current signal and simulated current signal under 3 GΩ of load for FEP25 (top left), FEP50 (top right), FEP76 (bottom left), and FEP125 (bottom right). The simulated current signal without considering C_{GROUND} is denoted M1. The simulated current signal accounting for C_{GROUND} is denoted M1. Parameters used in the simulation is given in table 4.2. The measured current signal is applied a running mean of 0.01 seconds to reduce noise.*

The absolute value of the simulated current through the load was integrated to find simulated charge transferred through the load per bubble. Figure 4.11 shows measured charge transferred through the load (whole line with error bars) per bubble, the simulation results (red cross) and the simulated result when accounting for C_{GROUND} (black diamonds). The measured charge per bubble is the same as displayed in figure 4.3. The different subplots display charge versus FEP thickness for different values of load. The covariation between simulation and measurement can be seen for both M1 and M1*. Quantitatively, M1* is noticeably closer to the measurements than M1. This is also apparent in figure 4.9 and 4.10 where one can see that M1 fails to replicate the diminishing of the second pulse in the signal triplet.

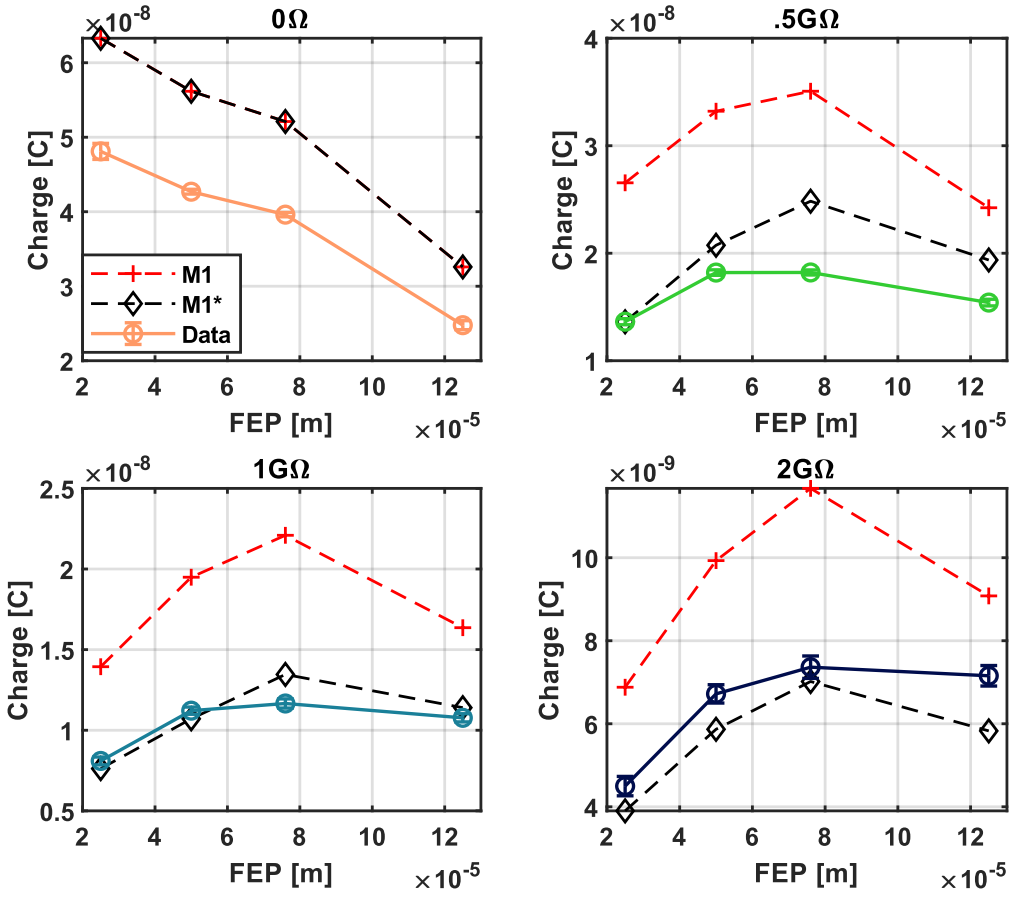

Figure 4.11: Charge transferred through load per bubble versus thickness of FEP under 0Ω (top left), 0.5GΩ (top right), 1GΩ (bottom left), and 2GΩ (bottom right). The simulated charge without considering C_{GROUND} is denoted M1 (red cross). The simulated charge accounting for C_{GROUND} is denoted M1 (black diamond).*

Figure 4.12 shows the measured peak current for the first pulse in the signal triplet (whole line with error bars) per bubble, the model results (red cross) and the model result when considering C_{GROUND}

(black diamonds). The different subplots display peak current versus FEP thickness for different values of load.

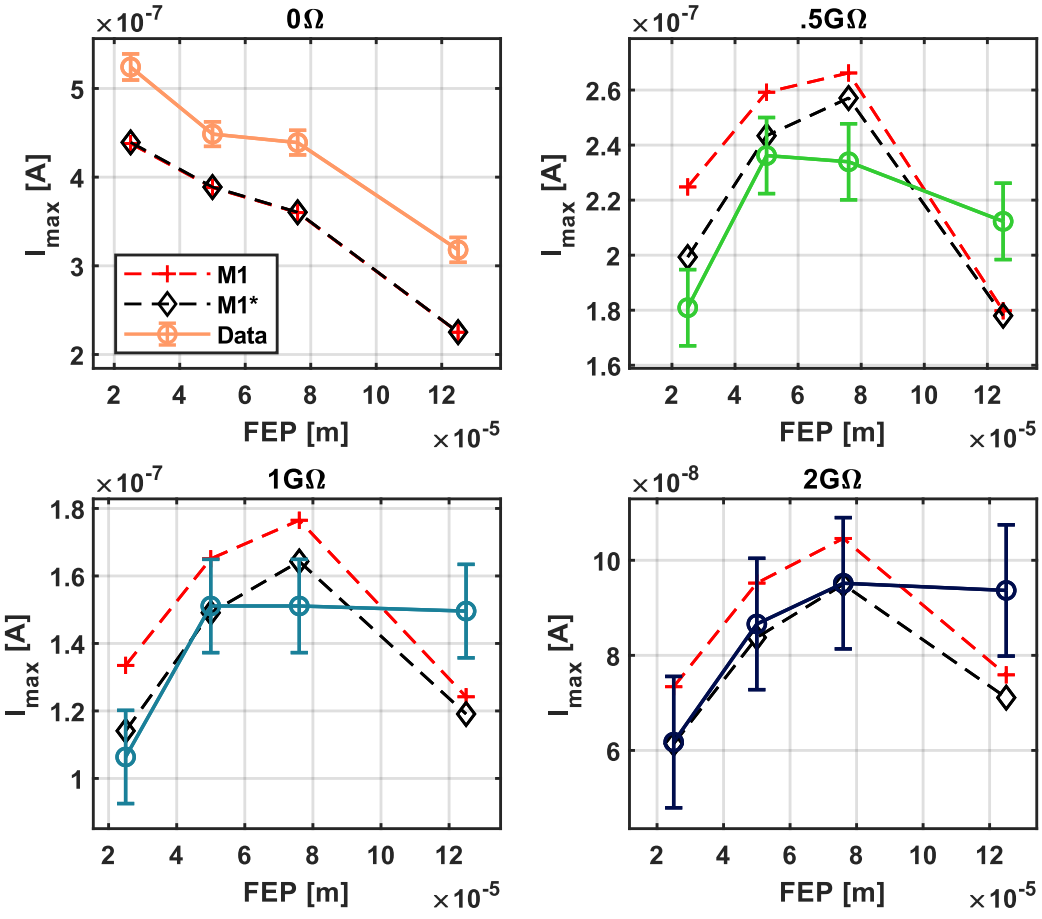

Figure 4.12: Peak current for the first pulse versus thickness of FEP under 0Ω (top left), 0.5GΩ (top right), 1GΩ (bottom left) and 2GΩ (bottom right). The simulated charge without considering C_{GROUND} is denoted M1 (red cross). The simulated charge accounting for C_{GROUND} is denoted M1 (black diamonds).*

Figure 4.13 shows the measured duration of the first pulse in the signal triplet compared with the model prediction. The uncertainty in measured duration is high due to the method of obtaining this data. Here, error bars are only one standard deviation in magnitude. This is explained in the appendix on uncertainty.

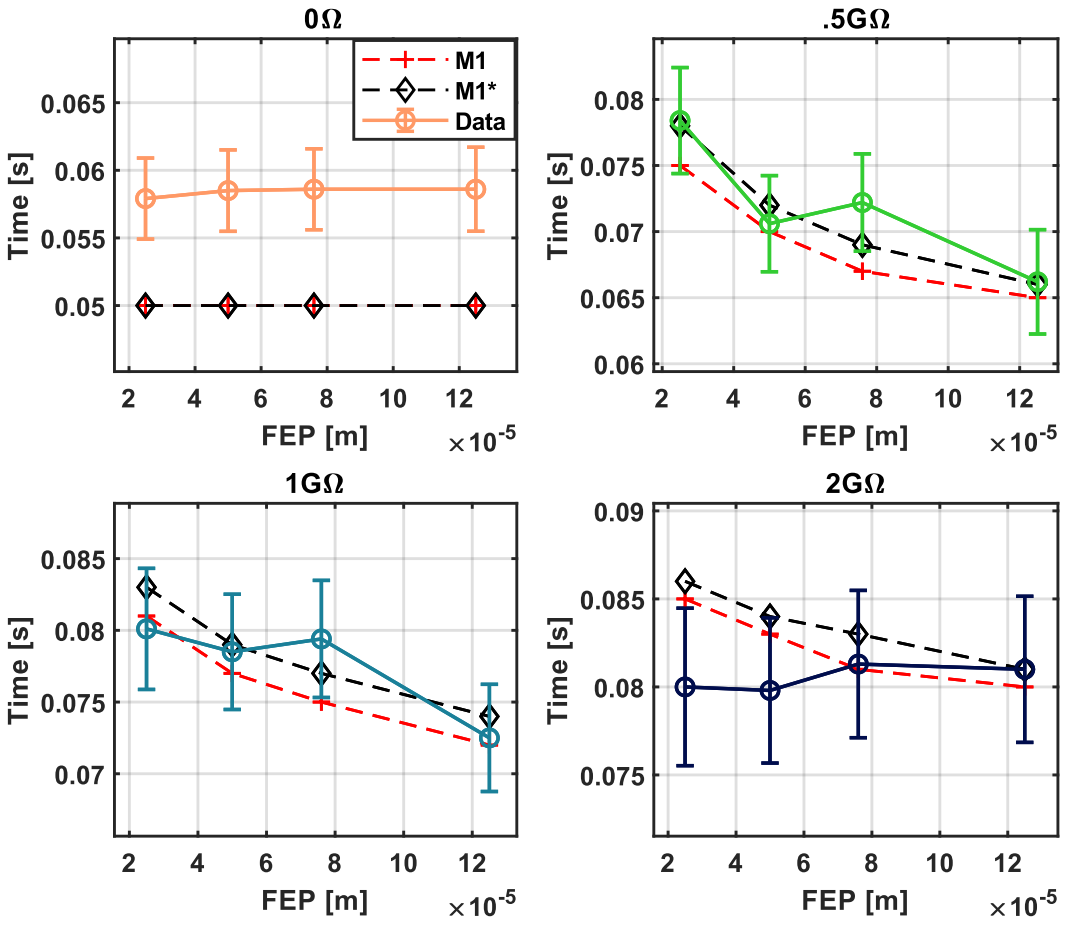

Figure 4.13: Duration of first pulse versus thickness of FEP under 0Ω (top left), 0.5GΩ (top right), 1GΩ (bottom left) and 2GΩ (bottom right). The simulated duration without considering C_{GROUND} is denoted M1 (red cross). The simulated duration accounting for C_{GROUND} is denoted M1 (black diamond). Error bar magnitude is here only one standard deviation.*

The model replicates the earlier observed tendencies with regard to the duration of the first pulse. The duration of the first pulse increases when resistance increases. The model also predicts that duration decreases with increasing polymer thickness.

Covariance between the model and the measured signal shape was observed at high load. This is seen in figure 4.9-4.13. At zero load the model clearly failed to reflect qualitative features of the measured signal shape. For example, the ratio of the first to the third pulse magnitude, and how this ratio showed a tendency to increase with FEP thickness. Motivated by this, an alternative interpretation of the model was analyzed and simulated.

4.2.1 Model 2

Equivalent circuit

In model 1 it was assumed that there are no sources or sinks of charge in the water body. We could then view $C_{E1}(t)$ and $C_{E2}(t)$ as one capacitor as discussed in chapter 2.2.2. This simplified the analysis of the equivalent circuit. Consider the following alternative interpretation:

As a bubble pushes positive charge away from the polymer under the bottom electrode, it is equivalent to charges from the electrode to move into the water body, rather than to the other electrode, as assumed in model 1. When a bubble displaces the diffuse positive layer along the FEP surface, a corresponding charge is induced in the electrode above. Now, the induced charge in the electrode is screening the field from the FEP surface charges instead of the diffuse layer in the water. Because the net positive charge associated with this layer is no longer bound by the negative surface charges, we consider them as free and inserted into the water body. Therefore, for the purpose of analyzing the circuit, we assume this to be analogous to a current parallel to $C_{E1}(t)$ and $C_{E2}(t)$.

Therefore, the current through $C_{E1}(t)$ and $C_{E2}(t)$ may not be equal and the waterbody must be considered as a circuit node of its own. In this model, the driving current must be split into two sources. One for each electrode. Each proportional to the rate at which surface charge is exposed under the respective electrode. The equivalent circuit of this is shown in figure 4.14.

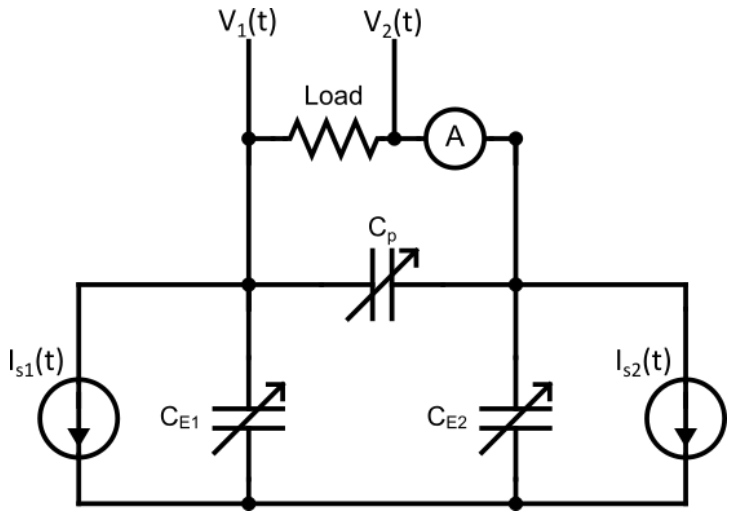

Figure 4.14: Equivalent circuit when considering the water body as an independent node. The unscreening of polymer surface charge is here modeled as a current source transporting current from the electrode and into the waterbody underneath. Each electrode has a current source representing the unscreening of charge under it.

The output of the ideal current sources $I_{s1}(t)$ and $I_{s2}(t)$ is here,

$$I_{s1}(t) = \frac{dA_{b1}(t)}{dt}\sigma, \tag{4.1}$$

and,

$$I_{s2}(t) = \frac{dA_{b2}(t)}{dt}\sigma. \tag{4.2}$$

Analysis of equivalent circuit

The water body is chosen, as reference, to be of zero potential relative to the other nodes in the circuit. Recall that positive current through the load was defined to be in the direction towards the bottom electrode, E_1.

Observe that the charge stored in $C_{E1}(t)$ must be the sum of the charge from transferred through the load and Cp, minus the integral of $I_{s1}(t)$. This can be written as

$$C_{E1}(t)V_1(t) = -\int I_{s1}(t)dt + \int \frac{V_2(t) - V_1(t)}{R}dt + C_p\big(V_2(t) - V_1(t)\big), \tag{4.3}$$

where $V_1(t)$ is the potential on the left side of the load and in figure 4.14 and $V_2(t)$ is the potential on the right side. Likewise, the charge on $C_{E2}(t)$ is

$$C_{E2}(t)V_2(t) = -\int I_{s2}(t)dt - \int \frac{V_2(t) - V_1(t)}{R}dt - C_p\big(V_2(t) - V_1(t)\big). \tag{4.4}$$

The derivative of equation 4.3 is

$$\frac{dV_1(t)}{dt}\Big(C_{E1}(t)+C_p(t)\Big) = -V_1(t)\left(\frac{1}{R} + \frac{dC_{E1}(t)}{dt}\right) - I_{s1}(t) + \frac{V_2(t)}{R} + C_p\frac{dV_2(t)}{dt}. \tag{4.5}$$

The derivative of equation 4.4 is

$$\frac{dV_2(t)}{dt}\Big(C_{E2}(t)+C_p(t)\Big) = -V_2(t)\left(\frac{1}{R} + \frac{dC_{E2}(t)}{dt}\right) - I_{s2}(t) + \frac{V_1(t)}{R} + C_p\frac{dV_1(t)}{dt}. \tag{4.6}$$

Model 2 describes the potential across the load, V2(t) – V1(t). This is done with two differential equations, equation 4.5 and 4.6.

Again, these equations were simulated using the same simple loop program in MATLAB, running the equations in small time steps. The model 2 results without considering C_{GROUND} are discussed as M2. The model 2 simulation result considering C_{GROUND} is discussed as M2*. In simulation of model 1 C_{GROUND} was simply assumed to be large enough to be considered a conductor. A better approximation is attempted here:

The magnitude of C_{GROUND} parameter used to simulate model 2 was chosen based on the following approximation. The bottom of the water container was separated from the conducting laboratory bench by a 65 mm cardboard box. The container had a bottom area of approximately $0.3m \times 0.3m$. This alone should constitute a capacitance of at least $\frac{\varepsilon_0 \times A}{0.065} = 12 \times 10^{-12} F$, approximating it as an infinite plane parallel plate capacitor. However, edge effects should here be prominent and add substantially to this because the distance between the "plates" are large compared to the "plate" dimensions. In addition to this, both the apparatus holding the bubble pipe and the tested devices were made of metal, in contact with the table and in close proximity (2-10 cm) to the water body. It was therefore chosen to round this capacitance up to the closest order of magnitude, $10^{-10} F$.

Table 4.4 shows the parameters used when simulating model 2. Mind that the only differences in the simulation parameters of model 1 and model 2 are:

- Surface charge density magnitude was increased by 50% in model 2 simulations. The relative relation between surface charge density between different FEP thickness were held the same.
- Improvement of evaluation of capacitive connection between upper electrode and water body through ground, C_{GROUND}, as discussed above.

Except for this, the assumptions of the capacitive connections and the properties of the bubble are held constant, still based on the analytic evaluations done in chapter 2.2.2 and 2.2.3.

Parameters	***M2* (C_{GROUND} considered)***	***M2***
FEP125 $[Cm^{-2}]$	45×10^{-6}	45×10^{-6}
FEP76 $[Cm^{-2}]$	72×10^{-6}	72×10^{-6}
FEP50 $[Cm^{-2}]$	78×10^{-6}	78×10^{-6}
FEP25 $[Cm^{-2}]$	87×10^{-6}	87×10^{-6}
$I_{S1}(t)$	$\frac{dA_{b_1}(t)}{dt}\sigma$	$\frac{dA_{b_1}(t)}{dt}\sigma$
$I_{S2}(t)$	$\frac{dA_{b_2}(t)}{dt}\sigma$	$\frac{dA_{b_2}(t)}{dt}\sigma$
W_E, electrode width, [m]	0.04	0.04
l_E, electrode length, [m]	0.01	0.01
W_b, bubble width, [m]	0.03	0.03
l_b, bubble length, [m]	0.015	0.015
Bubble speed, [m/s]	0.25	0.25
Cp, [F]	28.32×10^{-12}	28.32×10^{-12}
C_{GROUND} [F]	10^{-10}	0
$C_s(t)$, serial capacitance, [F]	$C_{E1}(t) = \frac{A_{W1}(t)\varepsilon_{FEP}}{d}$ $C_{E2}(t) = \frac{A_{W2}(t)\varepsilon_{FEP}}{d} + 10^{-10}$ (Equation 2.4)	$C_{E1}(t) = \frac{A_{W1}(t)\varepsilon_{FEP}}{d}$ $C_{E2}(t) = \frac{A_{W2}(t)\varepsilon_{FEP}}{d}$ (Equation 2.4)
Time resolution, [s]	1.88×10^{-6}	1.88×10^{-6}
Bubble shape (shape of three-phase line of air, water and FEP surface)	Elliptical, as described by equation 2.14, chapter 2.23 and appendix 2.	Elliptical, as described by equation 2.14 and chapter 2.23 and appendix 2.

Table 4.4: Model parameters used in model 2. FEP surface charge density is increased with 50%.

Figure 4.15 shows the signal shapes model 2 predicts under short circuit with parameters as in table 4.4. For M2 the predicted signal is similar as in M1 and M1*. Namely, no significant difference in the magnitude of first and third peak can be seen. The signal predicted by M2*, on the other hand, replicates the measured difference between the first and third pulse magnitude quite well.

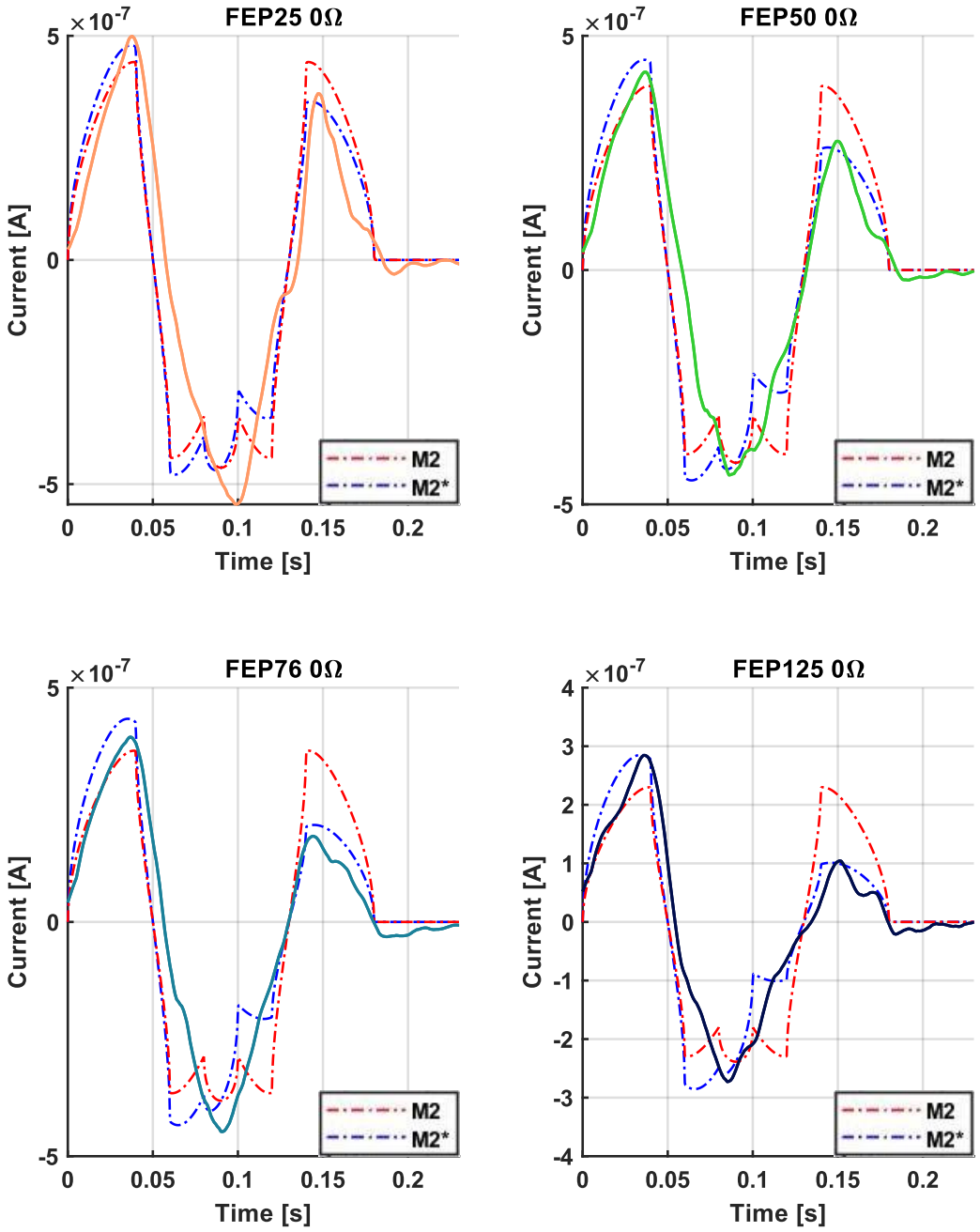

Figure 4.15: Comparison between measured current signal and model 2 simulated current signal in short circuit for FEP25 (top left), FEP50 (top right), FEP76 (bottom left), and FEP125 (bottom right). The simulated current signal without accounting C_{GROUND} is denoted M2. The simulated current signal accounting for C_{GROUND} is denoted M2. Parameters used in the simulation is given in table 4.4. The measured current signal is applied a running mean of 0.01 seconds to reduce noise.*

The ratio of the magnitude of pulse 1. to pulse 3. in the measured short circuit current signal was obtained and displayed in table 4.3. Adding to table 4.3 the simulated ratio obtained by M2* we obtain the following, displayed in table 4.5.

	FEP25	**FEP50**	**FEP76**	**FEP125**
Ratio 1.pulse/3.pulse	1.74 ± 0.16	1.67 ± 0.13	2.19 ± 0.15	2.91 ± 0.24
Ratio M2*	1.36	1.72	2.09	2.82

Table 4.5: Mean ratio of first to third pulse magnitude in short circuit measurement (first row) and model 2 when accounting for C_{GROUND} (second row). Average based on five last signal triplets for each dataset filtered with a running mean of 0.02 seconds. Uncertainty in mean is purely statistical with confidence of 95%.

As displayed earlier in table 4.3, it can be seen that the measured first pulse is in fact approximately between 60 - 200% higher than the third. Also, the ratio increases with increasing thickness. We see that M2* reflects both these observed tendencies. For FEP50, 76 and 125 the ratio predicted is within the 95% confidence interval of the measured ratio.

Figure 4.16 and 4.17 displays an example of measured signal shape plotted together with model prediction for model 2 under respectively 0.5 GΩ and 3 GΩ of load.

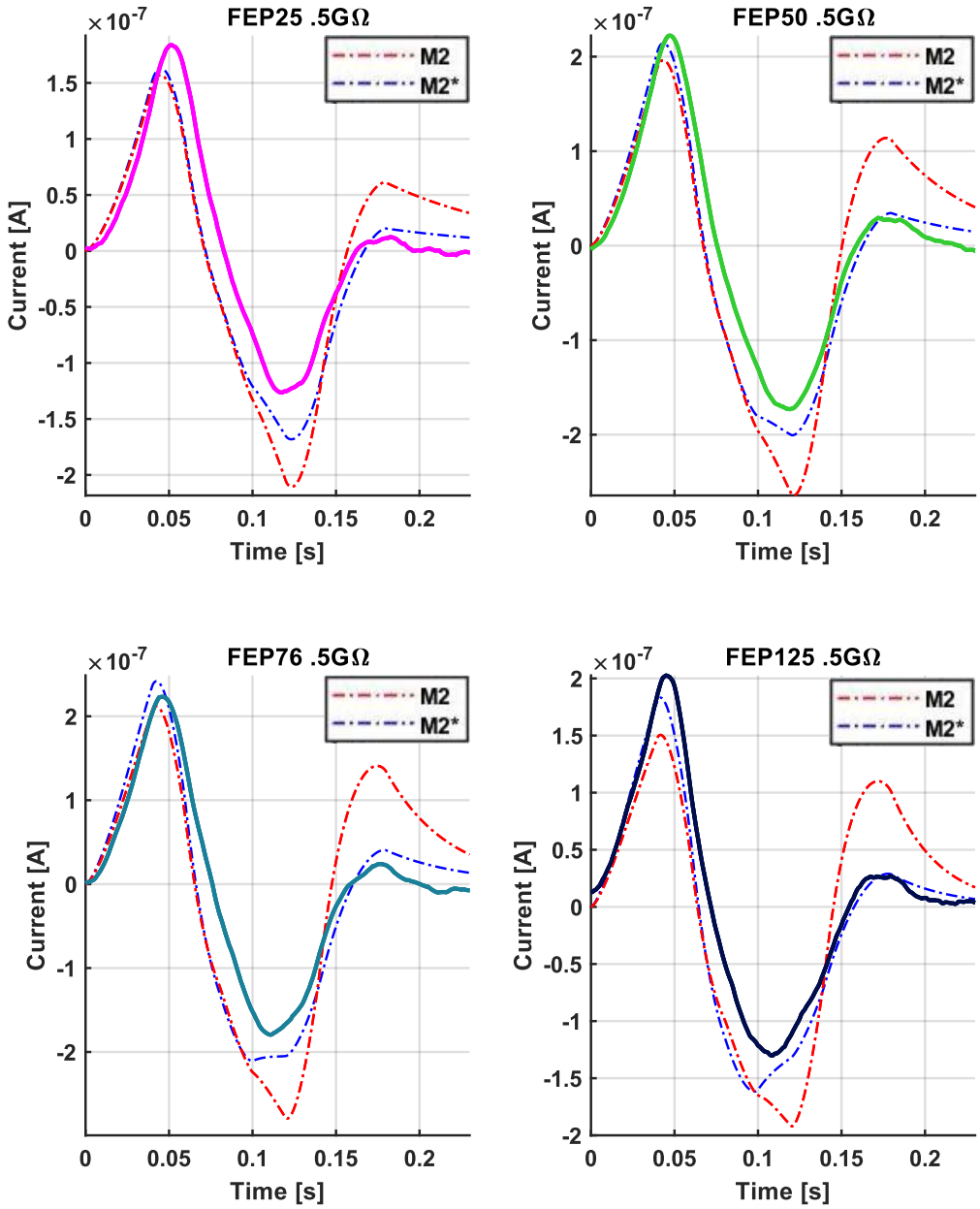

Figure 4.16: Comparison between measured current signal and model 2 simulated current signal under a load of 0.5 GΩ for FEP25 (top left), FEP50 (top right), FEP76 (bottom left), and FEP125 (bottom right). The simulated current signal without accounting for C_{GROUND} is denoted M2. The simulated current signal accounting for C_{GROUND} is denoted M2. Parameters used in the simulation is given in table 4.4. The measured current signal is applied a running mean of 0.01 seconds to reduce noise.*

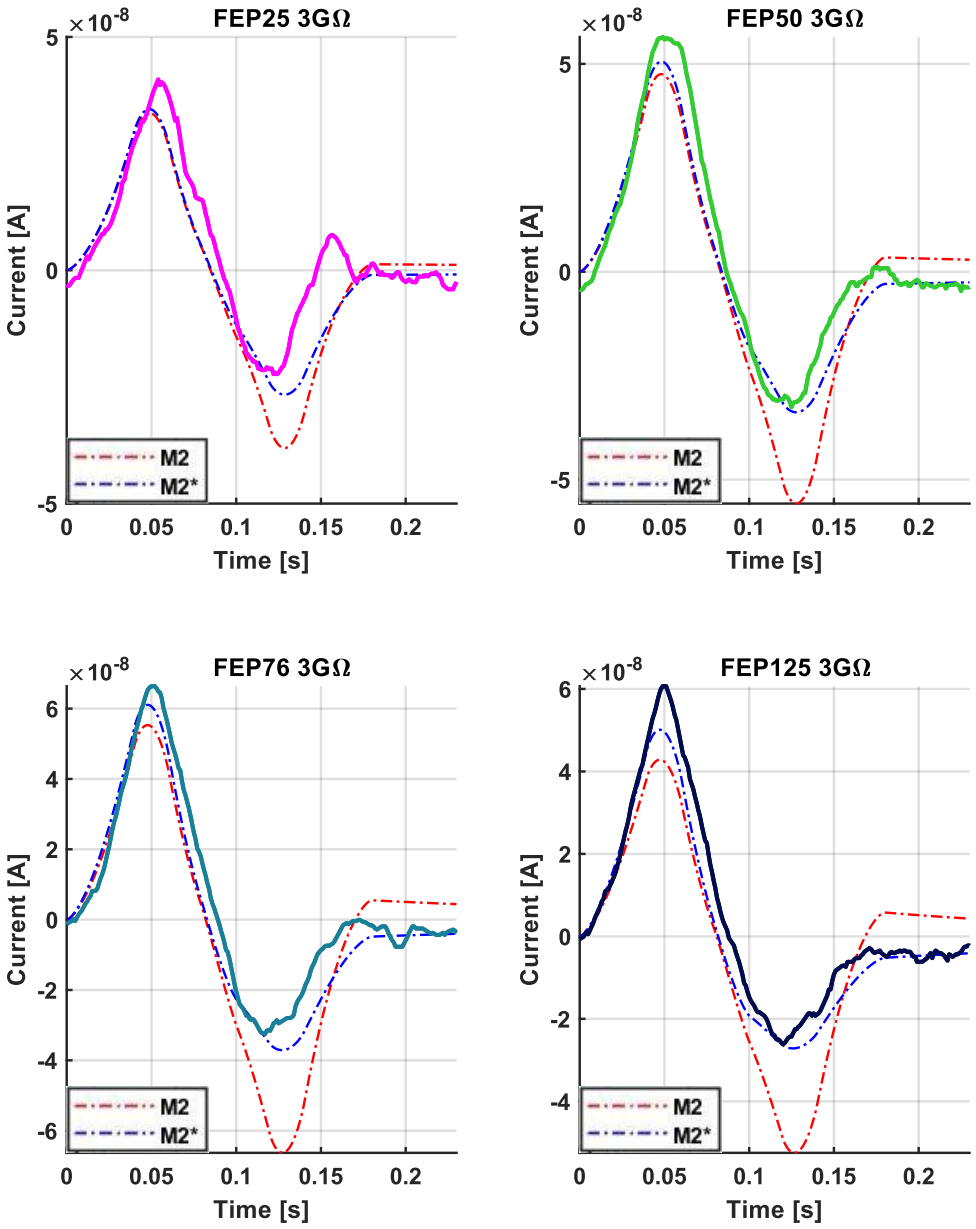

Figure 4.17: Comparison between measured current signal and model 2 simulated current signal under a load of 3 GΩ for FEP25 (top left), FEP50 (top right), FEP76 (bottom left), and FEP125 (bottom right). The simulated current signal without accounting for C_{GROUND} is denoted M2. The simulated current signal accounting for C_{GROUND} is denoted M2. Parameters used in the simulation is given in table 4.4. The measured current signal is applied a running mean of 0.01 seconds to reduce noise.*

Figure 4.15 and table 4.5 show that M2* predicts the relative relationship between the first and third pulse at zero load. This feature was absent in M1 and M1*. In figure 4.17 one can see that M2* also predicts a small negative current after the bubble has passed both electrodes, slowly tapering off to

zero, under 3GΩ of load. This is also observed in the data, but not replicated by M1 or M1*. For a slightly better view of this feature, review figure 4.1.

It is interesting to compare model 1 and model 2 in how they simulate transferred charge through the outer circuit. Figure 4.18 compares the simulated charge transferred through the outer circuit per bubble for M1* and M2*. Mind that the two simulations differ in two parameters. These are the magnitude of C_{GROUND} and the surface charge density of FEP125. Model parameters can be found in table 4.2 and 4.4.

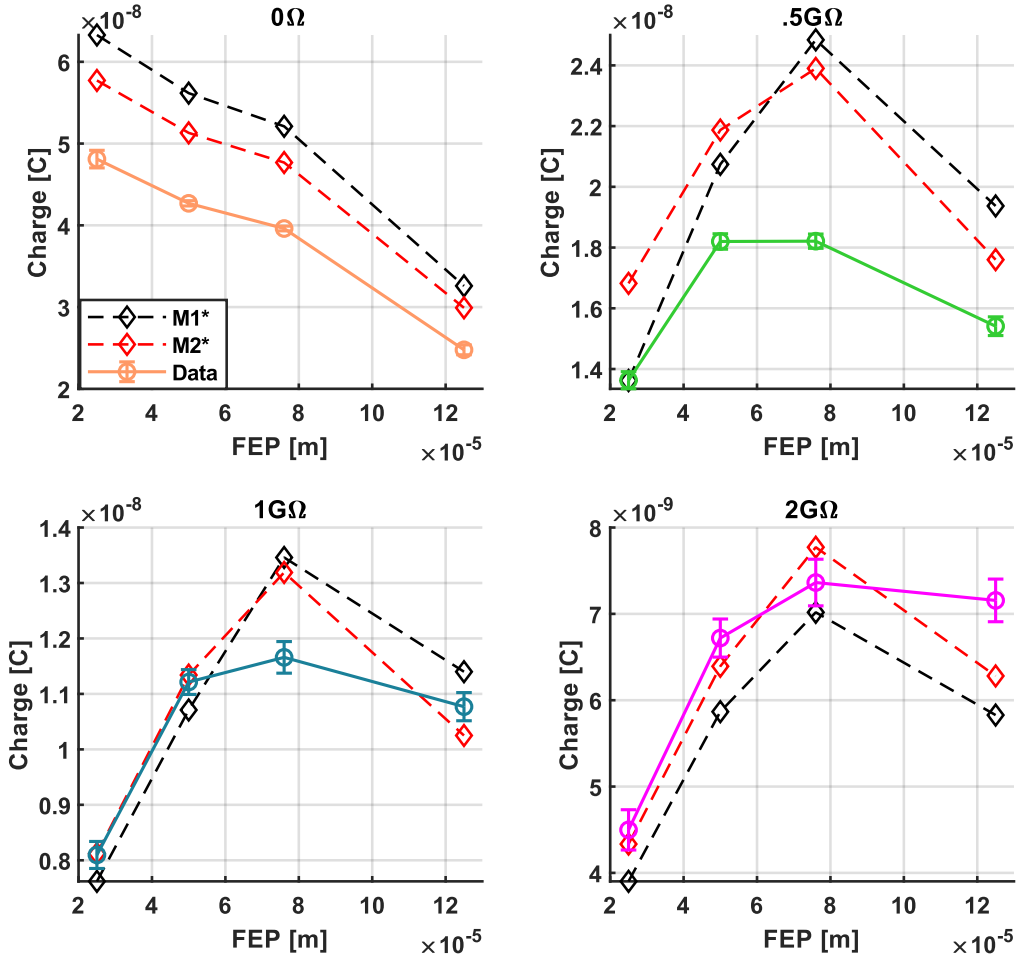

Figure 4.18: Comparison of model 1 and 2 on simulation of charge transferred through the outer circuit per bubble. Model 1 simulation accounting for C_{GROUND} is denoted with black diamonds. Model 2 simulation accounting for C_{GROUND} is denoted with red diamonds. Measured charge is denoted by whole line with error bars.

The simulations of model 2 reproduces feature of the current signal shape that simulation of model 1 did not reproduce. However, when considering the total charge transferred through the outer circuit per bubble, model 1 and model 2 predictions are quite similar. This can be seen in figure 4.18.

5 DISCUSSION

5.1 SIGNAL SHAPE

Figure 4.1 shows individual signal triplets created from one bubble passing both electrodes. In short circuit the signal consists of three pulses. This can be explained within the framework from chapter 2.2.1 as a superposition of phase 2 and 3. That is, the bubbles length in the direction of motion is longer than the gap between the electrodes. This was also observed and explained in a similar manner by Wijewardhana et al. [28].

The last signal pulse was significantly smaller than the first in magnitude. This feature was more significant for thicker FEP. To illustrate this, the ratio of the first to the third current pulse magnitude was measured and shown in table 4.3. Model 1 predicted a perfectly symmetrical current signal and did therefore not replicate this feature to any degree. This can be seen in figure 4.8. After modifying the model, deriving model 2 in chapter 4.2.1, this tendency was well replicated when accounting for C_{GROUND}. This can be seen in figure 4.15, and was quantified in table 4.5.

When a high resistive load was connected between the electrodes, this further reduced the magnitude of the second and third pulse relative to the first. Both simulation of model 1 and model 2 reproduced this feature. Accounting for C_{GROUND} improved the covariation between simulation and measurement for both models.

Model 2 simulation replicated the ratio of the first to the third pulse magnitude in short circuit when accounting for C_{GROUND}. This might indicate that model 2 is a better description of the physical process occurring in the BMAT. Recall the essential distinction between the models. In model 2 each electrode was considered individually. The displacement of the positive diffuse layer by the bubble was considered analogous to positive charge being injected into the water body circuit-node. In model 1 we assumed that the current through C_{E1} and C_{E2} always was equal and that it therefore was permissible to consider the two capacitors as one. The model 1 assumption proves insufficient in describing the current signal shape attributes in short circuit. However, the current signal shape expected by the models relies on the assumption that the shape of the bubble is constant as it slides across the electrodes. It can therefore not be excluded that asymmetry in the current signal is simply due to degrading contact between bubble and the FEP surface as it slides along.

Figure 4.7 shows the duration of the first pulse versus FEP thickness. The measured duration of the first positive pulse in the current signal increased with increasing load. Uncertainty in this statement is low when considering the difference between duration in short circuit (0Ω) and in any of the applied loads. A tendency was also seen of duration decreasing with increasing FEP thickness under 0.5GΩ of

load. This tendency has significant uncertainty attached to it. Recall that error bars in figure 4.7 are only one standard error. However, it can be considered more likely than not that the first pulse duration of the signal triplet decreases with increasing FEP thickness for 0.5 GΩ.

In figure 4.13 it is clearly seen that simulation of model 1 replicates the increase in first pulse duration with increasing load. The model 1 simulation also produced a decrease in first pulse duration with increasing FEP thickness, as observed for 0.5 GΩ. The exact first pulse duration was not retrieved from model 2 simulation. However, by close observation of figure 4.16 and 4.17 one can see that the same tendencies are reproduced by model 2.

5.2 CHARGE TRANSFERRED PER BUBBLE

In short circuit, charge transferred per bubble decreased with increasing FEP thickness. This is displayed in figure 4.3. Charge transferred per bubble for FEP125 was nearly half of FEP25. This is considered the first key finding.

When a load was connected between the electrodes, charge transferred through it decreased with increasing load. This can be seen in figure 4.4. A non-linear relationship between FEP thickness and charge transferred through the load was also seen. Energy per bubble, being a function of charge, therefore showed the same pattern. Medium FEP thickness yielded highest charge and energy per bubble. FEP25 yielded the lowest charge transferred and energy for all loads. This is considered the second key finding.

Measurement uncertainty in the second key finding is low. This can be seen by the error bars in figure 4.4 and 4.5, denoting two standard deviations in measurement uncertainty as calculated in appendix 1. However, because only one device per FEP thickness was made, there is no way of statistically quantifying the uncertainty due to potential lack of precision in fabrication. The probability that the results are due to random variations in fabrication rather than the FEP thickness alone can therefore not be excluded or statistically quantified. Drifting of environmental parameters and their effect was controlled for by testing some devices twice. Some drift was observed, but this was not significant compared to the variations observed with respect to FEP thickness. It is therefore unlikely that the observed features of the data are due to an unidentified drifting parameter.

As mentioned, the first key finding was that as FEP thickness was increased, short circuit charge transfer decreased. The most direct interpretation of this results is that the thinner FEP holds a higher effective surface charge density. This would explain why more charge is induced in the electrode per bubble. Previous investigations done on polymer surfaces in air, made similar conclusions. In 1991 Xia and Jiang found that the surface charge density of a FEP film with a conducting backplate was correlated to its thickness after corona charging [34]. The thinner film in this study obtained the highest surface charge density. The surfaces in this experiment were only exposed to air after

charging. After negative corona charging of a 11 µm and a 25 µm sample, the thinner sample had roughly double the effective charge density of the thicker. Because most of the charge is at or near the surface, they proposed the relationship between surface charge density, surface potential and thickness of

$$\sigma = \frac{\varepsilon \varepsilon_0 V_s}{d}, \tag{5.1}$$

where σ is the surface charge density of the FEP, ε is the relative permittivity of the FEP, ε_0 is the permittivity of free space, V_s is the surface potential, and d is the thickness of FEP sheet. Their findings therefore suggested that surface potential relative to the backplate was approximately constant, translating into higher charge density on thin samples.

Yatsuzuka et al. studied how drops of ultra-pure water falling on a PTFE surface gained positive charge, leaving the surface net negative. Based on scanning of the surface potential and measuring of the charge gained by the droplets that had been in contact with the surface, they concluded that electrification of a polymer surface by pure water is influenced by the thickness of the polymer [35]. It was reported that surface charge density became lower as the thickness of the polymer was increased. The authors proposed that the reason for this was the decreasing of the Coulomb force between surface charges and the mirror charges in the backplate when thickness was increased.

The experiments done by Yatszuka et al. and Xia and Jiang [34, 35] indicate that the electrostatic connection between the surface charges on the polymer and opposite mirror charges in the conductor on its back side, influences the density of surface charge the material can hold. Considering this, it is not the thickness of the electrification layer in itself that effect surface charge density, but the distance from the surface to a conducting material on its back side. As mentioned, Yatsuzuka et al. discussed that the decreasing Coulomb force possibly was the reason for the thicker PTFE plates to hold a lower surface charge density [35]. In their experiment, only a maximum of 12 droplets was dripped onto the surface and allowed to roll off. Also, the thinnest PTFE plate was 3.2 mm thick. In this case therefore, the extension of the charged area on the PTFE surface was perhaps comparable to the distance to the conducting back plate. This would justify explaining the phenomena in terms of a decreasing Coulomb force with increasing thickness, because the electric field between the surface charge and the mirror charges in the conductor is not uniform. However, in the case of Xia and Jiang, the FEP sheet samples they used were only 10 µm and a 25 µm thick. The electrode was circular with a diameter of 53 mm [34]. If the plane of the surface charge can be approximated as a homogenously charged plane, it can be argued that the field between the FEP surface and the backside conductor should be uniform in the bulk of the area. If this is true, changing the distance between the surface charges and the mirror charges does not change the electrostatic force between the planes, only the potential difference between them. The approximation of the surface charges as a homogenously charged plane can be

argued for, based on the surface charge density and the average distance between charged species on the surface. Assuming that charge is spread uniformly in species of elementary charge, the typical distance between charges on the surface can be calculated as $\sqrt{\frac{e}{\sigma}}$, where σ is the surface charge density and e is the elementary charge. Fluoropolymer films used for energy harvesting are typically reported to have surface charge densities above $10^{-5}Cm^{-2}$ [17, 31]. Therefore, the typical distance between charges on the surface will be on the order of $10^{-7}m$. If the thickness of the electrification layer is much larger than this distance, we would expect the field between the surface charge and the mirror charges to be approximately uniform in the bulk of the area. Changing the distance between the surface and the conducting backplate/electrode will in that case not change the electrostatic force between the surface charges and the mirror charges in the bulk area. However, along the edges of the electrode the field is not uniform and the argument about Coulomb force arguably becomes more plausible in this region.

Short circuit charge transfer per bubble is found to be higher for thinner FEP in this thesis. This indicates that the surface charge density decreases with increasing thickness on a submerged FEP surface subjected to bubbles. Earlier work demonstrates thickness dependency on surface charge density on polymer surfaces in air [34, 35]. Thickness dependency on surface charge density of submerged polymer surfaces was not found to have been investigated by others before.

The second key finding was a non-linear relationship between FEP thickness and charge transferred per bubble when a high load resistor was connected between the electrodes. Medium FEP thickness yielded the highest charge transferred under high load. Both models replicated this finding in terms of a covariance with the measurements. This can be seen most clearly in figure 4.11 and 4.18.

The observed effect can be explained as the combined effect of thin FEP having higher effective surface charge density, and thin FEP also resulting in higher mutual capacitance between the electrodes, as shown in section 2.2.2. Higher surface charge density increases output. This can be seen straight forward by equation 2.2 or 2.12. However, thinner FEP also contributes to higher mutual capacitance between the electrodes, which decreases output. To explain this, consider equation 2.12, describing the potential across the load in model 1. If total capacitance is high, voltage across the load is lower, and therefore the current through the load. This is true for any situation where there is a difference between the second and third term in equation 2.12. Therefore, high mutual capacitance between the electrodes reduces the BMATs ability to transfer charge through the outer circuit quickly. Because the driving force behind the charge transfer is limited in time, this results in a lower total charge transferred per bubble. In other words, high mutual capacitance between electrodes results in a smaller fraction of the induces charge to transfer through the load before the bubble has passed.

Wijewardhana et al. showed that in their BMAT that, increasing electrode area while keeping all else constant, decreased the power dissipated in the test load connected between the electrodes [27]. They explained this as an effect of the increased capacitance due to the increased electrode area.

It is shown in this thesis that increasing capacitance by decreasing electrification layer thickness also can negatively affect power output. This finding fits with the conclusions in [27] and the theoretical understanding presented in this thesis. When the load between the electrodes is non zero and the capacitance between the electrodes becomes large, more of the induced charge will be trapped in the field between the electrodes rather than transferring through the outer circuit.

The practical implication of the above discussion is that for a given load, device geometry and bubble properties, electrification layer thickness can be optimized to maximize charge transferred through the outer circuit and thereby energy transduced.

In this thesis, only four different thicknesses of FEP were used. Also, the exact fraction of the area under the electrodes uncovered by the bubbles is unknown and variable. For future investigations it would be interesting to do experiments more specifically designed to reveal the relationship between electrification layer thickness and effective surface charge density in a BMAT. This could be done by more precisely controlling the wet and dry area of the device by dipping instead of subjecting it to bubbles. A wider range of FEP thicknesses could be tested, and the conducting material should be applied on its backside in a manner guaranteeing perfect contact. This could be done, for example, by metal sputtering. Such a study would give deeper insight in how electrification layer thickness and its effective surface charge density covaries, both quantitatively and qualitatively. Parameters such as ion availability, temperature and flow speed along the surface could also be varied as these parameters effect the properties of the EDL which again might affect the polymer surface ability to hold effective surface charge.

If a wider range of loads were tested, a good indication of the matched load would be obtained for the different FEP thicknesses. It is suspected that this would show that matched load increases with FEP thickness. This because, thicker FEP results in lower capacitance and therefore increases the quickness of the charge transfer through the load. The range of loads used in this experiment is not sufficient to show this.

5.3 ENERGY HARVESTING EFFICIENCY

There are many possible ways of evaluating the effectiveness of energy harvesting. Consider energy transduction efficiency, here defined as the ratio of the electric energy output from one bubble to the mechanical energy carried by one bubble. In order to evaluate this, we must evaluate the mechanical energy one bubble carries. On one hand, one can consider a bubble in water to have potential energy.

That is, the integral of the buoyancy force with respect to depth. On the other hand, the bubble can be viewed as an object moving, and therefore to have kinetic energy.

A bubble in water can be viewed as having a potential energy equaling the energy required to work against its buoyancy. Let us consider the change in potential energy of the bubble in the time interval it interacts with the BMAT in this work. This can be calculated as

$$\Delta E_p = mass\ of\ water\ displaced \times g \times vertical\ travel\ distance, \tag{5.2}$$

where g is the gravitational constant. The relevant trajectory length generating energy is from where the leading edge of the bubble meats E_1 to its trailing edge leaves E_2. This constitutes 4.5 cm if the bubble is 1.5 cm long. The BMAT plane the bubble was moving along had an angle of 30° relative to the horizontal. Therefore, the vertical travel distance generating energy is $4.5\ cm \times sin(30) = 2.25\ cm$. The average bubble volume was measured to 1.95 mL, i.e., 1.95 grams of water displaced. We disregard the fact that the bubbles volume and buoyancy slightly change over the vertical distance traveled due to pressure difference. This results in the bubble having a potential energy difference from before it effects the circuit to after of $\Delta E_p = 4.3 \times 10^{-4}\ J$.

Comparing this to the maximum energy per bubble, obtained by FEP76 under 0.5GΩ, we get a conversion efficiency of

$$\eta_{potential} = \frac{12 \times 10^{-7} J}{4.3 \times 10^{-4}\ \mathrm{J}} = 0.28\%. \tag{5.3}$$

Alternatively, suppose that the bubble moving in one direction must be compensated for by an equal volume of water moving in the opposite direction, in order for total volume to be conserved. Again, we disregard the compressibility of the bubble since we are considering a small extension in the vertical direction. Using the same bubble speed as in the simulations of 0.25 m/s, the kinetic energy of the corresponding water volume, moving in the same velocity as the bubble, becomes

$$\frac{1}{2} m v^2 = 6.1 \times 10^{-5}\ J. \tag{5.4}$$

Comparing this to the maximum obtained energy per bubble we get a conversion efficiency of

$$\eta_{kinetic} = \frac{12 \times 10^{-7} J}{6.1 \times 10^{-5}\ J} \approx 2\%. \tag{5.5}$$

The two measures of efficiency yields estimates separated by almost an order of magnitude.

Another way of comparing the results from this study with other reports is to calculate energy harvested per unit volume of bubbles, in other words, joules per cubic meter. Once more, using the

maximum obtained energy of $12 \times 10^{-7} J$ for one bubble, and the measured average bubble volume we obtain

$$Energy\ per\ volume\ bubble = \frac{12 \times 10^{-7} J}{1.95 \times 10^{-6}\ m^3} = 0.62\ Jm^{-3}. \quad (5.6)$$

In the same manner, the peak power per unit volume can be calculated. The highest peak power was measured from FEP50 under 0.5GΩ load, reaching approximately $2.8 \times 10^{-5} W$, therefore,

$$Peak\ power\ per\ volume\ bubble = \frac{2.8 \times 10^{-5} W}{1.95 \times 10^{-6}\ m^3} = 14\ Wm^{-3}. \quad (5.7)$$

Table 5.1 show energy and power per bubble volume in this work, compared to other relevant studies on BMAT where this information was provided. The optimum (match) load was not obtained in this work. Both maximum energy per bubble, and maximum peak power was obtained under the lowest load tested, 0.5 GΩ.

	Energy per bubble volume	**Peak power per bubble volume**	**Bubble volume used in study**	**Electrification material**
This thesis	$0.62\ Jm^{-3}$	$14\ Wm^{-3}$	$1.95 \times 10^{-6}\ m^3$	FEP, flat untreated
Yan, 2022 [23]	$1.72\ Jm^{-3}$	$56.4\ Wm^{-3}$	$0.1 \times 10^{-6} m^3$	PTFE, flat -Unknown thickness. -100 MΩ matched load.
Li, 2023 [22]	-	$0.45\ Wm^{-3}$	$10 \times 10^{-6} m^3$	PTFE, pipe -1 mm wall thickness -500 MΩ matched load

Table 5.1: Energy per bubble volume and peak power per bubble volume reported here and in [22, 23].

5.4 MODELS AND SIMULATION

Simulation of the system was done under assumptions both based on physical arguments done before experiments, and observations of the data. Simulations were done first using the model derived in chapter 2, model 1. Seeing that the simulation of this model failed to replicate some key qualitative aspects of the measurements, an adjusted model was derived and simulated, model 2.

The capacitance between E_2 and the water through ground, C_{GROUND}, was accounted for differently in model 1 and 2. In model 1 it was simply assumed to be large enough to be considered as a conductor parallel to $C_{E2}(t)$. This approximation is crude because for it to be valid this capacitance should be much larger than that associated with the electrode-water connection, $C_{E2}(t)$. Before simulating model 2, this capacitance was attempted approximated by evaluating the geometry of the setup. From the discussion in chapter 4.2.1 it was approximated to be around 100 pF.

As discussed in chapter 4.2, the relative relation of surface charge density between FEP thicknesses used in simulations, is obtained from the short circuit charge transferred per bubble. This can be reviewed in table 4.1. Therefore, it is important to note that the presented models and simulations to no degree predicts the relationship between FEP thickness and effective surface charge density in the BMAT. This information was only observed experimentally and implemented as a parameter in simulations. Recall also that this method rested on an assumption that charge transferred in short circuit is proportional to the device surface charge density. A more complete model should include a qualitative description of how effective surface charge density depends on electrification layer thickness, among other parameters. However, simulations replicated the relative relationship between FEP thickness and performance when load was increased. This indicates that if surface charge density is known, the presented model might be useful in describing the rest of the process in terms of design parameters, the bubble properties and well-known bulk material properties.

The magnitude of the surface charge density parameter used in simulations was determined by simple trial and error. Plainly, the simulations were run several times while adjusting FEP125 surface charge density, holding the relative relationship between FEP125 and the other thicknesses constant, as shown in table 4.1. This was done until the best approximate fit with measurements was reached. Using this method, the surface charge density parameter used in simulation of model 2 was 50% higher than for model 1. In simulation of model 1, surface charge density was set to 30 μCm^{-2} for FEP125. For model 2 the corresponding was 45 μCm^{-2}, 50% higher than for model 1.

The M2* simulation replicated the signal shapes measured better than the other simulations. This, combined with the more realistic assumption of value of C_{GROUND} used in this simulation can be used to argue that this model is more physically correct in describing the system. However, the surface charge density parameter-setting required in model 2 to replicate measured results is suspiciously high when considering previous work on FEP in water. Zhu et al. reported for example of a surface charge density of approximately $42\mu Cm^{-2}$for a nano structured $70\mu m$ FEP film [17].

5.5 ANALYTICAL APPROXIMATION OF ENERGY PER BUBBLE

Model 1, as described by equation 2.12, were simulated numerically. However, if further simplifications are done, equation 2.12 can be solved analytically. In the following discussion this is done by removing the time dependency in two parameters. Namely, mutual capacitance and the rate at which the bubble overlaps with the electrodes. Also, only the time interval of phase 1 is considered. That is, the time from the bubble starts to overlap with E_1 until it is at the maximum overlap with E_1.

We approximate $C_1 \; and \; C_2$ to be constant at

$$C_1 = C_2 = \frac{A_e \varepsilon}{d} \tag{5.8}$$

where A is the electrode area, ε is the permittivity of FEP and d is the thickness of the FEP film. The total serial capacitance through the water then becomes

$$C_s = \frac{1}{\frac{1}{C1} + \frac{1}{C2}} = \frac{C_{1/2}}{2}. \tag{5.9}$$

We keep our previous approximation of the direct capacitance between the two electrodes,

$$C_p = 28 \; pF. \tag{5.10}$$

The total capacitance becomes

$$C_{total} = \frac{C}{2} + C_p. \tag{5.11}$$

The time dependency of $\frac{dA}{dt}$ can be removed by considering the bubble as a rectangular shape of width W_b and length l_b moving at a constant speed. The rate of area change then becomes

$$\frac{dA}{dt} = W_b \times v. \tag{5.12}$$

If $W_b = 2.7 \; cm$ and $l_b = 1 \; cm$, the maximum overlap between the electrode and this bubble is equal to the maximum overlap of the elliptical bubble used in the simulations in chapter 4. This shape is described in detail in appendix 2. The time needed for the rectangular bubble to fully overlap with the electrode is $\frac{l_b}{v}$, where v is the speed of the bubble. Using the same speed as observed from the data and used in simulations, this time interval, T, becomes

$$T = \frac{l_b}{v} = 0.04 \; seconds. \tag{5.13}$$

This represents the duration of phase 1 as illustrated in figure 2.4. We see that from t = 0 to t = T, $\frac{dA}{dt}$ is a constant.

The simplifications done on capacitance and $\frac{dA}{dt}$ enables us to write equation 2.12 as

$$C_{total}\frac{dV(t)}{dt} = \frac{dA}{dt}\sigma - \frac{V(t)}{R}. \tag{5.14}$$

A solution for this is equation is

$$V(t) = \frac{dA}{dt}\sigma R\left(1 - e^{-\frac{t}{\tau}}\right), \tag{5.15}$$

where τ is the time constant

$$\tau = RC_{total}. \tag{5.16}$$

Using ohms law, the current through the load is then

$$I_{RL}(t) = \frac{V(t)}{R_L} = \frac{dA}{dt}\sigma\left(1 - e^{-\frac{t}{\tau}}\right). \tag{5.17}$$

The instantaneous power dissipated in the load is

$$P(t) = I_R(t)^2 \times R\,. \tag{5.18}$$

The energy dissipated in the load from t = 0 to t = T is

$$E_{phase1} = \int_0^T P(t)dt, \tag{5.19}$$

which solves to

$$E_{phase1} = \left(\frac{dA}{dt}\sigma\right)^2 R\left(T + 2\tau e^{-\frac{T}{\tau}} - \frac{\tau}{2}e^{-\frac{2T}{\tau}} - \frac{3}{2}\tau\right). \tag{5.20}$$

Equation 5.20 gives the energy dissipated in the load in the first phase. If we approximate that energy dissipated in the load is equal in each phase of the bubble passing the BMAT, the total energy per bubble becomes

$$Energy\ per\ bubble \approx E_{phase1} \times 4. \tag{5.21}$$

Figure 5.1 shows the same as figure 4.5, measured energy per bubble. Superimposed on this is the prediction of equation 5.21. Except the bubble geometry and the simplification of capacitance, the parameters are held as when simulating model 1 in chapter 4. Table 5.2 shows the parameters used. The parameters simplified relative to earlier simulation of model 1 are highlighted.

Parameters	***Value***
Surface charge density FEP 125, $[Cm^{-2}]$	30×10^{-6}
Surface charge density FEP 76, $[Cm^{-2}]$	48×10^{-6}
Surface charge density FEP 50, $[Cm^{-2}]$	52×10^{-6}
Surface charge density FEP 25, $[Cm^{-2}]$	58×10^{-6}
W_E, electrode width, [m]	0.04
l_E, electrode length, [m]	0.01
W_b, bubble width, [m]	***0.027***
l_b, bubble length, [m]	***0.01***
Bubble speed, [m/s]	0.25
C_{GROUND}, [F]	0
C_p, [F]	28×10^{-12}
$\boldsymbol{C_{E1}}$, $\boldsymbol{C_{E2}}$	$\boldsymbol{C_{E1} = C_{E2} = \frac{A_e \varepsilon}{d}}$
C_s, serial capacitance, [F]	$\boldsymbol{\frac{1}{C_s} = \frac{1}{C_{E1}} + \frac{1}{C_{E2}}}$
Time resolution, [s]	–
Bubble shape, (three-phase line air, water and FEP surface)	***Rectangular***

Table 5.2: Parameters used when solving equation 5.19 in figure 5.1.

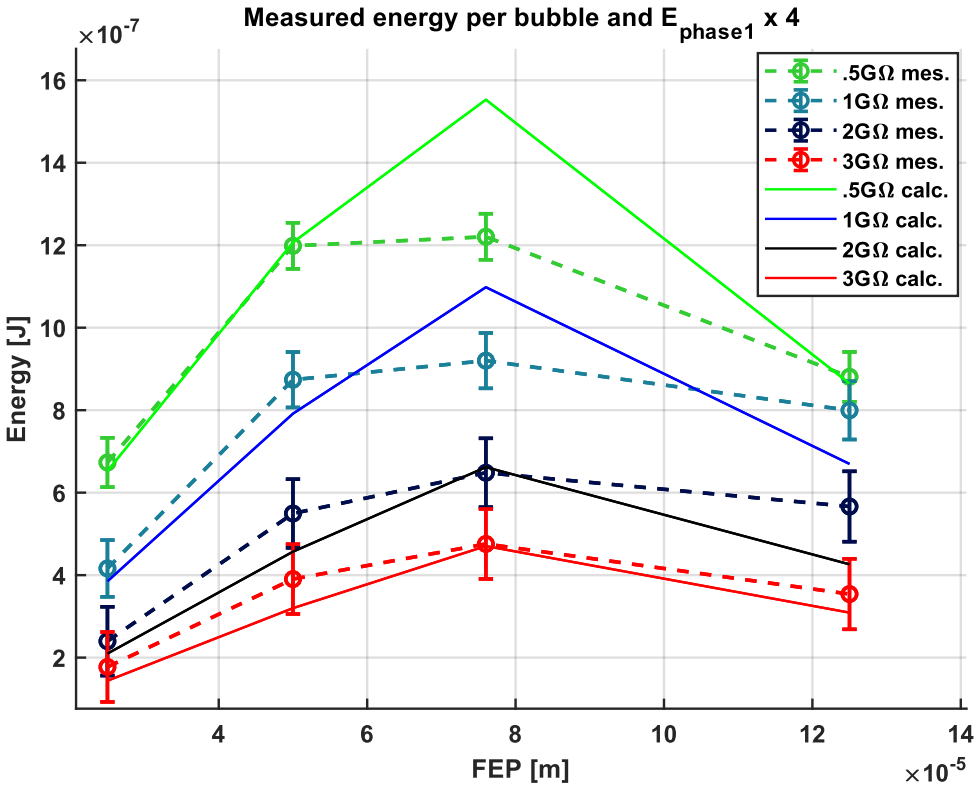

Figure 5.1: Measured energy dissipated in different loads per bubble passing the BMAT as earlier shown in figure 4.5 in dotted lines with error bars. Prediction by equation 5.21 on energy per bubble in whole line with corresponding color.

It can be seen in figure 5.1 that even with the rough simplifications done to obtain a simple analytical prediction on energy, there is covariance between calculated energy and measured energy.

In figure 5.2, equation 5.21 is solved with varying bubble speed under a 0.5GΩ load. It is seen here that energy per bubble rises quickly with bubble speed, reaching an optimum speed before it asymptotically goes to zero for very high speeds. Note that the different FEP thicknesses have optimum energy yields at different bubble speeds. For thicker FEP, optimum speed is higher.

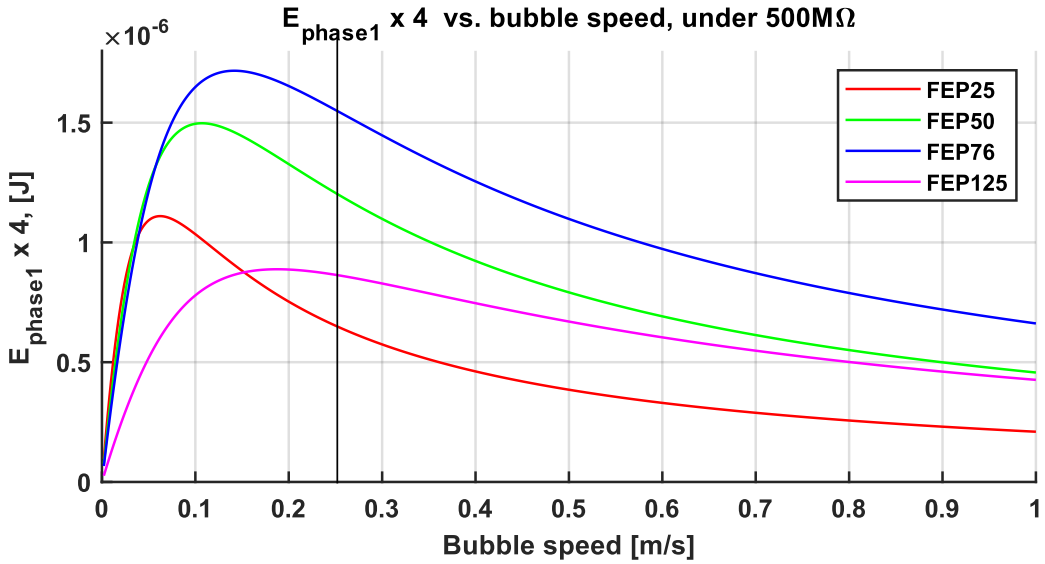

Figure 5.2: Equation 5.21 prediction on energy per bubble under a load of 0.5GΩ as a function of bubble speed for FEP25 (red), FEP50 (green), FEP76 (blue), and FEP125 (magenta). The approximate bubble speed obtained in experiment of 0.25 m/s is marked by a line.

Figure 5.3 shows the same as figure 5.2, but for a load one order of magnitude smaller, 50MΩ. The same relative relationship between the different thicknesses can be seen. However, optimum energy is reached for much higher bubble speeds. Also, the magnitude of the optimum energy is equal as for 500MΩ. This indicates that the same amount of energy could be harvested from a slow bubble as from a fast bubble if the resistive load is lowered in magnitude.

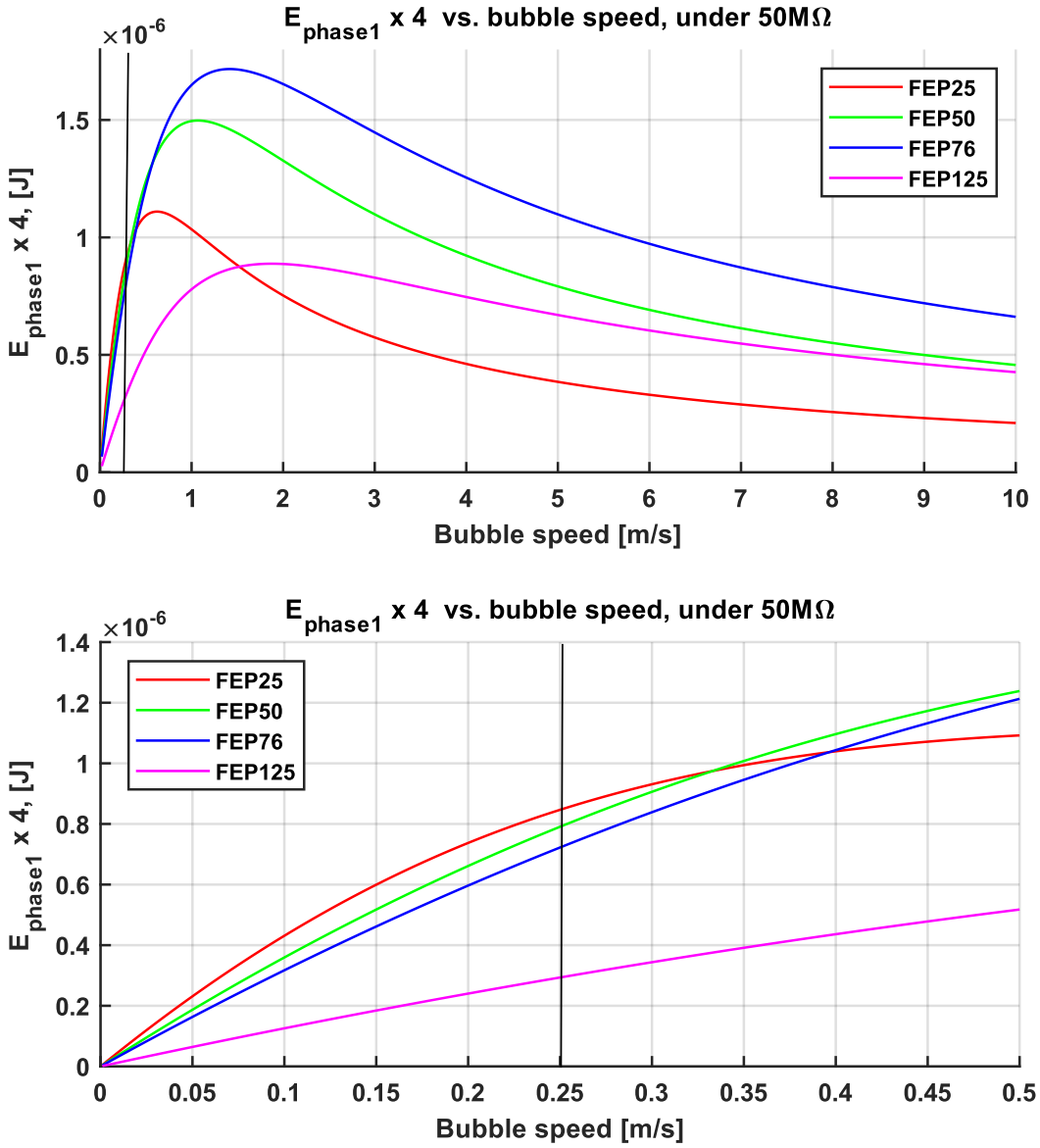

Figure 5.3: Equation 5.21 prediction on energy per bubble under a load of 50MΩ as a function of bubble speed for FEP25 (red), FEP50 (green), FEP76 (blue), and FEP125 (magenta). The approximate bubble speed in experiment of 0.25 m/s is marked by a line. Upper panel: Zero to 10 m/s. Lower panel: Zero to 0.5 m/s.

The calculation leading to figure 5.2 and 5.3 both rests on the simplifying assumptions made above and that the surface charge density on the FEP surface would not be affected by bubble speed. However, it is highly possible that a big change in bubble speed both effects the magnitude of the surface charge density, and possibly the relative relationship between surface charge density between different thicknesses of FEP. Besides this, figure 5.2 and 5.3 illustrates that in optimization of BMAT energy yield, one should consider bubble speed in relation to load and electrification layer thickness. For example, consider if the BMAT described in this thesis was to drive an application constituting a load of 50MΩ, and the expected characteristic bubble speed was 4 m/s. The upper panel of figure 5.3 indicates that a thick FEP might be most effective. Suppose the expected bubble speed is only 0.1 m/s. The lower panel of figure 5.3 would suggest that thinner FEP might be better.

6 CONCLUSIONS

In this work it is demonstrated that air bubbles sliding across a FEP sheet in water with two electrodes imbedded, transduced some of the bubble's mechanical energy into electric energy. Similar devices have been demonstrated lately [22-24, 27-30], but no experimental research has been found on the effect of the electrification layer thickness. Therefore, the main aim of this work was to find how the thickness of the FEP sheet effected the process of energy transduction. A theoretical model of the device was presented to describe the current through a resistive load connected between the electrodes. The model described this in terms of the surface charge density of the FEP surface, geometric properties of the device, bulk material properties and the rate at which the bubble overlaps with the electrodes.

In experiments, it was first found that a thinner FEP sheet in the BMAT gave a higher charge transfer through the outer circuit in short circuit. When a high load was connected between the electrodes, the medium thickness of FEP used, yielded the highest charge transferred through the load and therefore the highest amount of energy transduced. The highest energy yield was obtained by the medium thickness FEP reaching 1.2 μJ transduced from a 1.95 ml bubble. Numerical simulation of the model replicated qualitatively the relationship between charge transferred per bubble, and FEP thickness. Features of the current signal shape from the passing of one bubble was also replicated. Examples are the duration of the first current pulse and the relative magnitude between pulses in the signal. Both these features varied with load resistance and FEP thickness.

The experimental results strongly indicate that thin FEP holds a higher effective surface charge density, increasing the number of induced charges. However, thinner FEP increases mutual capacitance between the electrodes, resulting in slower charge transfer through the outer circuit when a high load is applied. The experimental results therefore illustrates that the challenge of optimizing energy transduction may involve a compromise between high effective charge density and low mutual capacitance between electrodes. The theoretical model presented imply that optimization of energy transduction also relies on electrode area, permittivity of the electrification layer and bubble speed.

7 REFERENCES

[1] K. Adu-Manu, N. Adam, C. Tapparello, H. Ayatollahi, and W. Heinzelman, "Energy-Harvesting Wireless Sensor Networks (EH-WSNs): A Review," *ACM transactions on sensor networks*, vol. 14, no. 2, pp. 1-50, 2018, doi: 10.1145/3183338.

[2] M. Pinuela, P. D. Mitcheson, and S. Lucyszyn, "Ambient RF Energy Harvesting in Urban and Semi-Urban Environments," *IEEE transactions on microwave theory and techniques*, vol. 61, no. 7, pp. 2715-2726, 2013, doi: 10.1109/TMTT.2013.2262687.

[3] G. Zhu, B. Peng, J. Chen, Q. Jing, and Z. Lin Wang, "Triboelectric nanogenerators as a new energy technology: From fundamentals, devices, to applications," *Nano energy*, vol. 14, no. C, pp. 126-138, 2015, doi: 10.1016/j.nanoen.2014.11.050.

[4] D. Champier, "Thermoelectric generators: A review of applications," *Energy conversion and management*, vol. 140, pp. 167-181, 2017, doi: 10.1016/j.enconman.2017.02.070.

[5] D. S. Renné, "Progress, opportunities and challenges of achieving net-zero emissions and 100% renewables," *Solar Compass*, vol. 1, p. 100007, 2022, doi: 10.1016/j.solcom.2022.100007.

[6] M. Bawahab, H. Xiao, and X. Wang, "A Study of Linear Regenerative Electromagnetic Shock Absorber System," 0148-7191, 2015.

[7] X. Tang, Z. Mones, X. Wang, F. Gu, and A. D. Ball, "A Review on Energy Harvesting Supplying Wireless Sensor Nodes for Machine Condition Monitoring," 2018: Chinese Automation and Computing Society in the UK - CACSUK, pp. 1-6, doi: 10.23919/IConAC.2018.8748946.

[8] S. K. Sengar, *Introduction to Wireless Power Transmission*. 2014.

[9] I. A. U.S. Energy Information Administration, SW, Washington, DC 20585. "Electricity explained, How electricity is generated." https://www.eia.gov/energyexplained/electricity/how-electricity-is-generated.php (accessed 28.07, 2023).

[10] S. Wang, Y. Xie, S. Niu, L. Lin, and Z. L. Wang, "Freestanding Triboelectric-Layer-Based Nanogenerators for Harvesting Energy from a Moving Object or Human Motion in Contact and Non-contact Modes," *Adv. Mater*, vol. 26, no. 18, pp. 2818-2824, 2014, doi: 10.1002/adma.201305303.

[11] H. Zhang, S. Feng, D. He, Y. Xu, M. Yang, and J. Bai, "An electret film-based triboelectric nanogenerator with largely improved performance via a tape-peeling charging method," *Nano energy*, vol. 48, pp. 256-265, 2018, doi: 10.1016/j.nanoen.2018.03.051.

[12] Z. L. Wang, "On Maxwell's displacement current for energy and sensors: the origin of nanogenerators," *Materials today (Kidlington, England)*, vol. 20, no. 2, pp. 74-82, 2017, doi: 10.1016/j.mattod.2016.12.001.

[13] Z. L. Wang, "Triboelectric Nanogenerators as New Energy Technology for Self-Powered Systems and as Active Mechanical and Chemical Sensors," *ACS Nano*, vol. 7, no. 11, pp. 9533-9557, 2013, doi: 10.1021/nn404614z.

[14] H. Zou *et al.*, "Quantifying the triboelectric series," *Nat Commun*, vol. 10, no. 1, pp. 1427-1427, 2019, doi: 10.1038/s41467-019-09461-x.

[15] Z. Yang, E. Halvorsen, and T. Dong, "Electrostatic Energy Harvester Employing Conductive Droplet and Thin-Film Electret," *Journal of microelectromechanical systems*, vol. 23, no. 2, pp. 315-323, 2014, doi: 10.1109/JMEMS.2013.2273933.

[16] X. Yang, S. Chan, L. Wang, and W. A. Daoud, "Water tank triboelectric nanogenerator for efficient harvesting of water wave energy over a broad frequency range," *Nano energy*, vol. 44, pp. 388-398, 2018, doi: 10.1016/j.nanoen.2017.12.025.

[17] G. Zhu *et al.*, "Harvesting Water Wave Energy by Asymmetric Screening of Electrostatic Charges on a Nanostructured Hydrophobic Thin-Film Surface," *ACS Nano,* vol. 8, no. 6, pp. 6031-6037, 2014, doi: 10.1021/nn5012732.
[18] L. E. Helseth, "Electrical energy harvesting from water droplets passing a hydrophobic polymer with a metal film on its back side," *Journal of electrostatics,* vol. 81, pp. 64-70, 2016, doi: 10.1016/j.elstat.2016.03.006.
[19] L. E. Helseth and X. D. Guo, "Fluorinated ethylene propylene thin film for water droplet energy harvesting," *Renewable Energy,* vol. 99, pp. 845-851, 2016, doi: 10.1016/j.renene.2016.07.077.
[20] L. E. Helseth and X. D. Guo, "Hydrophobic polymer covered by a grating electrode for converting the mechanical energy of water droplets into electrical energy," *Smart Mater. Struct,* vol. 25, no. 4, p. 45007, 2016, doi: 10.1088/0964-1726/25/4/045007.
[21] L. E. Helseth and X. D. Guo, "Contact Electrification and Energy Harvesting Using Periodically Contacted and Squeezed Water Droplets," *Langmuir,* vol. 31, no. 10, pp. 3269-3276, 2015, doi: 10.1021/la503494c.
[22] C. Li, H. Zhang, Y. Wang, X. Liu, A. Ali, and Z. Q. Tian, "Liquid–Solid Triboelectric Nanogenerator for Bubble Energy Harvesting," *Advanced materials technologies,* vol. 8, no. 11, p. n/a, 2023, doi: 10.1002/admt.202201791.
[23] X. Yan *et al.*, "Bubble energy generator," *Science advances,* vol. 8, no. 25, pp. eabo7698-eabo7698, 2022, doi: 10.1126/sciadv.abo7698.
[24] C. Li, X. Liu, D. Yang, and Z. Liu, "Triboelectric nanogenerator based on a moving bubble in liquid for mechanical energy harvesting and water level monitoring," *Nano energy,* vol. 95, p. 106998, 2022, doi: 10.1016/j.nanoen.2022.106998.
[25] Y. Song, W. Zhao, Y. Huang, and D. Li, "Underwater Bubble Detection and Counting By a Dynamic Changing Solid-Liquid Interfacial Process," *Sensors and actuators. B, Chemical,* vol. 329, p. 129083, 2021, doi: 10.1016/j.snb.2020.129083.
[26] Q.-T. Nguyen and K.-K. K. Ahn, "Fluid-Based Triboelectric Nanogenerators: A Review of Current Status and Applications," *International Journal of Precision Engineering and Manufacturing - Green Technology,* vol. 8, no. 3, pp. 1043-1060, 2020, doi: 10.1007/s40684-020-00255-x.
[27] K. R. Wijewardhana, T. K. Ekanayaka, E. N. Jayaweera, A. Shahzad, and J.-K. Song, "Integration of multiple bubble motion active transducers for improving energy-harvesting efficiency," *Energy,* vol. 160, pp. 648-653, 2018/10/01/ 2018, doi: https://doi.org/10.1016/j.energy.2018.07.058.
[28] K. R. Wijewardhana, T.-Z. Shen, and J.-K. Song, "Energy harvesting using air bubbles on hydrophobic surfaces containing embedded charges," *Applied energy,* vol. 206, pp. 432-438, 2017, doi: 10.1016/j.apenergy.2017.08.211.
[29] J. Chen *et al.*, "Self-Powered Triboelectric Micro Liquid/Gas Flow Sensor for Microfluidics," *ACS Nano,* vol. 10, no. 8, pp. 8104-8112, 2016, doi: 10.1021/acsnano.6b04440.
[30] Y. Yang, J. Park, S.-H. Kwon, and Y. S. Kim, "Fluidic Active Transducer for Electricity Generation," *Sci Rep,* vol. 5, no. 1, pp. 15695-15695, 2015, doi: 10.1038/srep15695.
[31] Z.-H. Lin, G. Cheng, L. Lin, S. Lee, and Z. L. Wang, "Water-Solid Surface Contact Electrification and its Use for Harvesting Liquid-Wave Energy," *Angew. Chem. Int. Ed,* vol. 52, no. 48, pp. 12545-12549, 2013, doi: 10.1002/anie.201307249.
[32] Z. Guan, P. Li, Y. Wen, Y. Du, T. Han, and X. Ji, "Efficient underwater energy harvesting from bubble-driven pipe flow," *Applied energy,* vol. 295, p. 116987, 2021, doi: 10.1016/j.apenergy.2021.116987.
[33] Z. Guan, P. Li, Y. Wen, Y. Du, and G. Wang, "Efficient and high-power subsea bubble energy harvesting by controlling flow pattern," *Sustainable energy technologies and assessments,* vol. 55, p. 102898, 2023, doi: 10.1016/j.seta.2022.102898.
[34] Z. Xia, J. Wu, and J. Jiang, "Influence of thickness on properties of polymer films electrets," 1991: IEEE, pp. 100-105, doi: 10.1109/ISE.1991.167190.
[35] K. Yatsuzuka, Y. Mizuno, and K. Asano, "Electrification phenomena of pure water droplets dripping and sliding on a polymer surface," *Journal of electrostatics,* vol. 32, no. 2, pp. 157-171, 1994, doi: 10.1016/0304-3886(94)90005-1.

[36] H. Zhang, S. Feng, D. He, P. Molinié, and J. Bai, "Amplitude-variable output characteristics of triboelectric-electret nanogenerators during multiple working cycles," *Nano energy,* vol. 63, p. 103856, 2019, doi: 10.1016/j.nanoen.2019.103856.
[37] Y. Yun *et al.*, "High Quality Electret Based Triboelectric Nanogenerator for Boosted and Reliable Electrical Output Performance," *International Journal of Precision Engineering and Manufacturing-Green Technology,* vol. 8, no. 1, pp. 125-137, 2021, doi: 10.1007/s40684-020-00245-z.
[38] S. Hasan, A. Z. Kouzani, S. Adams, J. Long, and M. A. P. Mahmud, "Comparative study on the contact-separation mode triboelectric nanogenerator," *Journal of electrostatics,* vol. 116, p. 103685, 2022, doi: 10.1016/j.elstat.2022.103685.
[39] X. He, H. Guo, X. Yue, J. Gao, Y. Xia, and C. Hu, "Improving energy conversion efficiency for triboelectric nanogenerator with capacitor structure by maximizing surface charge density," *Nanoscale,* vol. 7, no. 5, pp. 1896-1903, 2015, doi: 10.1039/c4nr05512h.
[40] X. Kang, C. Pan, Y. Chen, and X. Pu, "Boosting performances of triboelectric nanogenerators by optimizing dielectric properties and thickness of electrification layer," *RSC Adv,* vol. 1, no. 3, pp. 17752-17759, 2020, doi: 10.1039/d0ra02181d.
[41] D. J. Lacks and R. Mohan Sankaran, "Contact electrification of insulating materials," *Journal of physics. D, Applied physics,* vol. 44, no. 45, p. 453001, 2011, doi: 10.1088/0022-3727/44/45/453001.
[42] T. A. L. Burgo, F. Galembeck, and G. H. Pollack, "Where is water in the triboelectric series?," *Journal of electrostatics,* vol. 80, pp. 30-33, 2016, doi: 10.1016/j.elstat.2016.01.002.
[43] S. Lin, L. Xu, A. Chi Wang, and Z. L. Wang, "Quantifying electron-transfer in liquid-solid contact electrification and the formation of electric double-layer," *Nat Commun,* vol. 11, no. 1, pp. 399-399, 2020, doi: 10.1038/s41467-019-14278-9.
[44] L. E. Helseth, "Ion Concentration Influences the Charge Transfer Due to a Water−Air Contact Line Moving over a Hydrophobic Surface: Charge Measurements and Theoretical Models," 2023, doi: https://doi.org/10.1021/acs.langmuir.2c02716.
[45] X. Li *et al.*, "Polymer electrets and their applications," *Journal of applied polymer science,* vol. 138, no. 19, pp. 50406-n/a, 2021, doi: 10.1002/app.50406.
[46] *Teflon FEP fluoropolymer resin, Product and Properties Handbook*.
[47] Z. Levin and P. V. Hobbs, "Splashing of Water Drops on Solid and Wetted Surfaces: Hydrodynamics and Charge Separation," *Phil. Trans. R. Soc. Lond. A,* vol. 269, no. 1200, pp. 555-585, 1971, doi: 10.1098/rsta.1971.0052.
[48] M. Matsui, N. Murasaki, K. Fujibayashi, B. Peng You, and Y. Kishimoto, "Electrification of pure water flowing down a trough set up with a resin sheet," *Journal of electrostatics,* vol. 31, no. 1, pp. 1-10, 1993, doi: 10.1016/0304-3886(93)90043-7.
[49] V. V. Yaminsky and M. B. Johnston, "Static Electrification by Nonwetting Liquids. Contact Charging and Contact Angles," *Langmuir,* vol. 11, no. 10, pp. 4153-4158, 1995, doi: 10.1021/la00010a083.
[50] R. Zimmermann, U. Freudenberg, R. Schweiß, D. Küttner, and C. Werner, "Hydroxide and hydronium ion adsorption — A survey," *Current opinion in colloid & interface science,* vol. 15, no. 3, pp. 196-202, 2010, doi: 10.1016/j.cocis.2010.01.002.
[51] K. N. Kudin and R. Car, "Why Are Water−Hydrophobic Interfaces Charged?," *J. Am. Chem. Soc,* vol. 130, no. 12, pp. 3915-3919, 2008, doi: 10.1021/ja077205t.
[52] V. Tandon, S. K. Bhagavatula, W. C. Nelson, and B. J. Kirby, "Zeta potential and electroosmotic mobility in microfluidic devices fabricated from hydrophobic polymers: 1. The origins of charge," *ELECTROPHORESIS,* vol. 29, no. 5, pp. 1092-1101, 2008, doi: 10.1002/elps.200700734.
[53] R. J. Hunter, *Introduction to Modern Colloid Science*. Oxford University Press, 1993.
[54] D. J. Griffiths, *Introduction to electrodynamics*. Cambridge University Press, 1989.

APPENDIX 1, UNCERTAINTY

Tolerance of resistors

The devices were run in series with 0.5, 1, 2 and 3 GΩ of resistance. This was done by connecting 0.5 GΩ resistors in series. Each resistor is given to have a tolerance of+- 2% from the manufacturer. It was chosen to estimate the resistor standard deviation as the $\frac{tolerance}{\sqrt{3}}$ (Iso GUM 4.3.7). Therefore, the estimated standard uncertainty of a single resistor is assumed to be

$$\sigma_{.5G\Omega} = \frac{R \times 0.02}{\sqrt{3}} = 0.011547 \times R \rightarrow \frac{500 \times 10^6 \times 0.02}{\sqrt{3}} = 5.7735 \times 10^6. \qquad (A1.1)$$

Because we assume the variance of the resistors not to be correlated and normally distributed around the mean value of 0.5 GΩ, the standard deviation of several resistors in series can be approximated as the root sum of squares of the standard deviation of a single resistor.

$$\sigma_{sum} = \sqrt{Number\ of\ resistors\ \times\ \sigma^2{}_{.5G\Omega}}. \qquad (A1.2)$$

This gives the different combined standard uncertainties as shown in table A1.1.

Resistance [GΩ]	Standard uncertainty [Ω]	Relative standard uncertainty [%]
.5	5.77×10^6	1.15
1	8.16×10^6	0.816
2	11.54×10^6	0.577
3	14.13×10^6	0.471

Table A1.1: The values standard uncertainty in this table are used in evaluation of uncertainty in the peak power and energy per bubble.

Measurement uncertainty of current

The Pico amperemeter used was a Keithley 6485. It has an accuracy rating for the 2μA range of $\pm 0.15\%$ in addition to an offset of 100pA. The 2μA range was used for all experiments. In the experiments done this contributes maximally to an uncertainty of $10^{-6}A \times 0.0015 + 10^{-10}A = 1.6 \times 10^{-9}A$ because the largest current measured was almost $6 \times 10^{-7}A$.

Uncertainty due to noise are estimated from the standard deviation of the output signal when the device was not subjected to bubbles. The noise was highest under short circuit measurements. It was

then calculated to be approximately $6 \times 10^{-9}\ A$. When a moving average of 0.02 seconds was applied the noise standard deviation was reduced by more than one order of magnitude.

The resolution of the data collected to the computer was $3 \times 10^{-9} A$.

We see that for the typical current measured, noise and data resolution dominates uncertainty. Uncertainty in current data is calculated as

$$u(I) = \sqrt{(1.6 \times 10^{-9} A)^2 + (6 \times 10^{-9}\ A)^2 + (3 \times 10^{-9} A)^2} = 6.9 \times 10^{-9}\ A, \qquad (A1.3)$$

and when filtered by a moving average of 0.02 seconds,

$$u(I_{filter}) = \sqrt{(1.6 \times 10^{-9} A)^2 + (6 \times 10^{-10}\ A)^2 + (3 \times 10^{-9} A)^2} = 3.5 \times 10^{-9}\ A. \qquad (A1.4)$$

Effect of running mean on accumulated charge measurements

The filtered current data was used in calculations of charge and energy. In order to roughly evaluate how much of the signal was lost due to this filtering the integral of the filtered current was compared to that of the unfiltered current for a period of time where the device was under influence of a bubble. That is, for an interval where the current magnitude was high. The argument for the validity of this method is:

- When current magnitude is higher than the magnitude of the typical noise, the contribution of noise to the integral will be low as long as the integrated interval contains many wavelengths of the expected dominant noise frequency.
- In periods where the device did not interact with a bubble, we assume all non-zero current readings to be due to noise. Because charge was evaluated from the absolute value of current, and energy is a function of current squared, noise contributes to the integral in these periods. In other words, this constitutes an error biased towards yielding higher measured charge or energy. This main reason for employing the filter.
- Consider an interval of data containing a signal triplet. The length of this interval is about 0.15 - 0.2 seconds. We assume 50 Hz noise to dominate. This interval then contains 7.5 – 10 cycles of this frequency. The degree to which the integral of the filtered current is smaller than the integral from the unfiltered current evaluated in this interval can therefore be a guide to how much of the actual signal was lost due to filtering.

This was evaluated for a random signal triplet in the FEP25, 0Ω dataset. The integral of the filtered signal triplet was here 4.53 % lower than that from the corresponding unfiltered. The same was done

for one random triplet in the FEP25, 3GΩ dataset. The corresponding decrease from the unfiltered signal integral was here 4.43%. When considering the integral of the whole 600 seconds of data the decrease from the unfiltered to the filtered integral was 19.22% for FEP25, 3GΩ and 8.33% for FEP25, 0Ω.

An interpretation of this can be that, as suggested, noise contributes more to the integral of absolute current in between signal triplets than in them. As much as ~5% of the integrated signal might be lost due to filtering. However, filtering greatly reduces the upward error associated with intervals where the current is close to zero. To illustrate, figure A1.1 shows the integrated charge of the first signal triplet for FEP25 at 0Ω, with and without the running mean of 0.02 seconds.

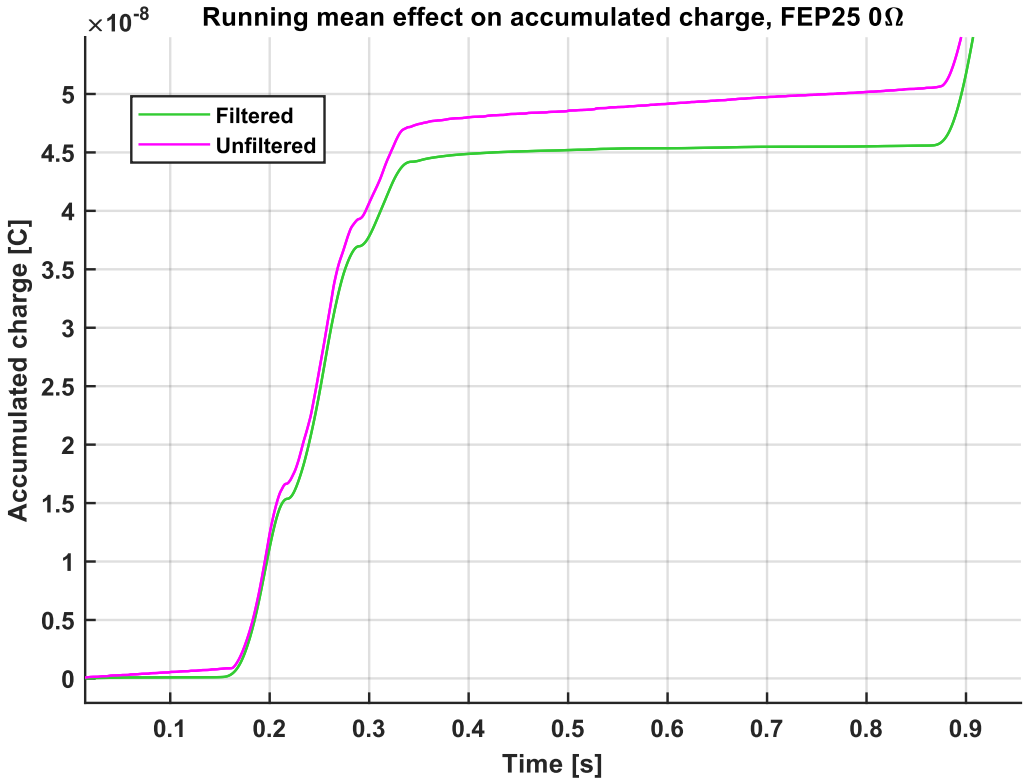

Figure A1.1: Accumulated charge for one signal triplet obtained from filtered signal (green) and unfiltered (magenta).

One can see that in the period between bubbles (0.4 – 0.8 seconds), the filtered accumulated charge only increases slightly while the unfiltered increases substantially more, resulting in falsely contributing energy from electromagnetic noise to the transduction of bubble motion energy.

Mean peak current, $\overline{I_{max}}$, was calculated from unfiltered current data. Its uncertainty is calculated as the root sum square of single measurement uncertainty and the standard error of the mean for the sample.

$$u^2(\overline{I_{max}}) = \frac{s^2}{N} + (6.9 \times 10^{-9}\, A)^2, \qquad (A1.5)$$

where s is the standard deviation of the N current peaks collected to create the mean.

Bias current

It was assumed that any net charge transfer measured over many signals must be due to drifting/ bias error in the meter and not a physical current. This was accounted for by subtracting this average bias current from the raw data. The average bias current was calculated as

$$\bar{I}_{bias} = \frac{\Delta t}{T} \sum_{0}^{\frac{\Delta t}{T}} I(i)\Delta t, \qquad (A1.6)$$

where T is the duration of the dataset (600 seconds) and Δt is the measurements interval.

Mean charge transferred per bubble

Cumulative charge transferred was calculated as

$$q(n) = \sum_{0}^{n} \left| I_{filtered}(i) \times \Delta t \right|, \qquad (A1.7)$$

where Δt is the interval of individual current measurements (1 millisecond). Mean charge transferred per bubble was calculated by choosing an interval and dividing the cumulative charge by the number of bubbles that passed the device in that interval.

Before charge transferred per bubble was calculated, the raw data was filtered in order to reduce uncertainty contribution from noise. It was assumed that no electromagnetic frequency below 50 Hz had meaningful impact on the measurements. Therefor the raw data was applied a moving average of 20 data points, corresponding to 0.002 seconds, in order to cover a whole 50 Hz cycle.

Assuming uncertainty in each current measurement is uncorrelated each other uncertainty in charge can be calculated as

$$u(q)^2 = \left(\Delta t u(I_1)\right)^2 + \left(\Delta t u(I_2)\right)^2 + \left(\Delta t u(I_3)\right)^2 \ldots + \left(\Delta t u(I_n)\right)^2. \qquad (A1.8)$$

Using the uncertainty calculated for the filtered current we obtain

$$u(q)^2 = n\Delta t^2 u^2(I_{\text{filter}}). \quad (A1.9)$$

We can express n as the time interval at which the charge transfer occurs, T, divided by the timestep Δt. Equation A1.9 then becomes

$$u(q)^2 = \Delta t T u^2(I_{filter}). \quad (A1.10)$$

The average time between bubbles is somewhat less than 1 second. Using 1 second for T we obtain an estimation of standard uncertainty in the charge produced by one bubble of $u(q) = 1.09 \times 10^{-10}$ Coulombs.

The standard uncertainty of the mean charge transferred per bubble is calculated as

$$u(\bar{q})^2 = u(q)^2 + \frac{s^2}{N}, \quad (A1.11)$$

where N is the number of signals measured, not to be confused with n, the number of current measurements within each interval of N. Standard deviation of charge samples is denoted s.

Mean energy per bubble

Instantaneous power is calculated as the product of filtered current squared and load resistance,

$$p(i) = {I_{filter}}^2(i)R. \quad (A1.12)$$

The standard uncertainty of the current is as mentioned as in equation (A1.4). And the standard uncertainty of R is as in table (A1.1). Considering the sensitivity of these underlying uncertainties the standard uncertainty of power becomes,

$$u(p)^2 = \left(\frac{dp}{d\bar{I}}\right)^2 u(I)^2 + \left(\frac{dp}{dR}\right)^2 u(R)^2. \quad (A1.13)$$

Cumulated energy dissipated in load for n measurements is calculated as

$$E(n) = \sum_0^n p(i) \times \Delta t. \quad (A1.15)$$

Average energy per bubble was then calculated by dividing the cumulated energy for an interval by the number of bubbles that passed the electrode in that interval. The variance was obtained by dividing the interval into subintervals, each containing the information from the passing of a single bubble. Uncertainty of energy was calculated as

$$u(E)^2 = \Delta t T u^2(p), \qquad (A1.16)$$

where T is the time interval. Using the highest peak current as a proxy for I(t) when evaluating A.1.13 for the different load values and T = 1 second, we obtain a simplified conservative estimate of uncertainty in energy per bubble as displayed in table A1.2. This is highly conservative because we estimate the energy uncertainty from the maximum uncertainty in power, which in reality lasts much shorter than the interval chosen, 1 second.

Load	**Maximum peak current as proxy for I(t)**	**Associated uncertainty in power**	**Associated uncertainty in energy per bubble**
0,5	$2.36 \times 10^{-7} A$	$8.76 \times 10^{-7} A$	$2.77 \times 10^{-8} J$
1	$1.51 \times 10^{-7} A$	$10.59 \times 10^{-7} A$	$3.35 \times 10^{-8} J$
2	$0.95 \times 10^{-7} A$	$13.16 \times 10^{-7} A$	$4.16 \times 10^{-8} J$
3	$0.69 \times 10^{-7} A$	$14.31 \times 10^{-7} A$	$4.23 \times 10^{-8} J$

Table A1.2: Estimated uncertainty in energy calculated for one bubble.

Uncertainty of average energy per bubble was calculated as the root sum square of the uncertainty of energy per bubble and the standard uncertainty of the mean for the sampled bubbles

$$u(\bar{E})^2 = u(E)^2 + \frac{s^2}{N}, \qquad (A1.17)$$

where s is the standard deviation in energy per bubble and N is the number of energy measurements.

Mean duration of the first pulse in the signal triplet

The duration of the first pulse in the current signal triplet was measured in Logger Pro using the cursor and selecting the interval of the pulse manually. To evaluate the variance associated with the use of this method, the same pulse was measured 10 times. The standard deviation of this sample is taken to represent the standard uncertainty associated with this method of collecting the data. The standard

uncertainty obtained by this method was 5.1%. No other sources of uncertainty were assumed to affect these measurements. Standard uncertainty of mean duration was therefore approximated as the root sum square of the standard error of the mean, and the standard uncertainty associated with human inaccuracy,

$$u(\overline{int})^2 = \frac{s^2}{N} + \left(\frac{5.1}{100}\overline{int}\right)^2 . \qquad (A1.18)$$

APPENDIX 2, DESCRIPTION OF THE BUBBLE

From preliminary experiments with the setup used, bubble velocity is approximated around 0.25 m/s. Bubbles was also observed to be sliding across the polymer surface in a roughly elliptical shape with an extension in the direction of movement of 1-2 cm and a width of 3-4 cm. We will attempt to approximate how these observed characteristics translates into the rate at which area under the electrodes overlaps with a bubble. We describe the bubble-water-polymer interface, the edge of the bubble in contact, as an elliptical shape, moving at a constant speed along the surface.

When an elliptical shape of width W and length l moves in the x-direction at a constant speed of v, the width of the shape where it intersects with x = 0 at time t is

$$W_{x=0}(t) = W\sqrt{sin\left(\frac{t}{T_b}\pi\right)}, \qquad (A2.1)$$

where $T_b = \frac{l_b}{V}$, is the time the whole bubble needs to pass x = 0. Therefore, the rate at which this shape covers area at x > 0 is

$$vW_{x=0}(t). \qquad (A2.2)$$

After t = T_b the entire bubble has passed x = 0. The contribution of eq. A2.2 is now zero. Therefore,

$$vW_{x=0}(t > T_b) = 0. \qquad (A2.3)$$

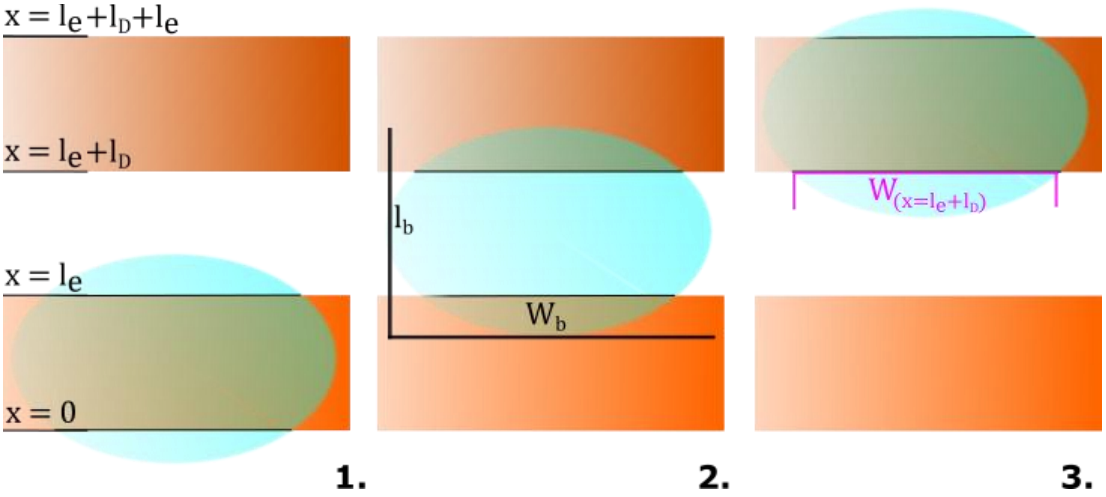

Figure A2.1: Illustration of an elliptical bubble of length lb and width Wb, sliding across two electrodes. The width of the line where the bubble intersects with a lower or upper edge of an electrode and the speed of the bubble determines how fast the are overlap between bubble and electrode changes. 1. The bubble is midway over the first electrode. In this instant the rate at which it slides off the electrode is equal to the rate at which it slides on. 2.

The electrodes are both limited in the x (length) and y (width) direction. We will disregard bubbles wider than the electrode. If the bubble is longer than the electrode, it will, when its leading edge reaches the top of the electrode (x = l_E) start to "slide off" at a rate

$$vW_{x=l_E}(t) = vW\sqrt{sin\left(\frac{t-T_e}{T_b}\pi\right)}, \qquad (A2.4)$$

where T_e is the time needed to travel one electrode length, $\frac{l_E}{v}$. This is the situation shown in part one of figure A2.1. Equation A2.4 does not contribute until the bubble reaches this point, that is when $t - T_e$ is larger than zero. After the bubbles trailing edge has left it is also zero. Therefore,

$$vW_{x=l_E}(t - T_e \leq 0 \leq t - T_e - T_b) = 0. \qquad (A2.5)$$

At the same time, if the bubble is longer than the electrode, its trailing edge is still on its way onto the electrode at x = 0. The total areal rate change happening at the electrode can be expressed as the sum of the area change happening a x = 0 and at x = El. Plainly, the rate at which it slides on minus the rate at which it slides off. This can be written as

$$\frac{dA_1(t)}{dt} = v\left(W_{x=0}(t) - W_{x=l_E}(t)\right), \qquad (A2.6)$$

the rate at which the area overlap between bubble and the bottom electrode changes.

Now, the time the leading edge of the bubble needs to travel from x = 0 to the first edge of the second electrode is $\frac{l_E+l_D}{v}$ (line in magenta in figure A2.1). The rate at which the bubble start to overlap with the first edge of the second electrode becomes

$$vW_{x=l_E+l_D}(t) = vW\sqrt{sin\left(\frac{t-T_e-T_D}{T_b}\pi\right)}. \qquad (A2.7)$$

The contribution of this expression is zero before the leading edge of the bubble starts overlapping with the second electrode and zero after its trailing edge has overlapped. Therefore,

$$vW_{x=l_E}(t - T_e - T_D \leq 0 \leq t - T_e - T_D - T_b) = 0. \qquad (A2.8)$$

Last, at the top of the second electrode, the bubble leaves at a rate

$$vW_{x=l_E+l_D+l_E}(t) = vW\sqrt{sin\left(\frac{t-T_e-T_D-T_b}{T_b}\pi\right)}. \qquad (A2.9)$$

This is zero everywhere except from the time the leading edge of the bubble starts to overlap with E_2 until its trailing edge leaves it. This can be expressed as

$$vW_{x=l_E}(t - 2T_e - T_D \leq 0 \leq t - 2T_e - T_D - T_b) = 0. \qquad (A2.10)$$

The rate of area overlap change at the second electrode then becomes

$$\frac{dA_2(t)}{dt} = v\left(W_{x=l_E+l_D}(t) - W_{x=l_E+l_D+l_E}(t)\right). \qquad (A2.11)$$

Based on the above equation we can calculate at which rate an elliptical bubble moving at a constant speed changes the dry area over both electrodes through time.

When simulating the output of the BMAT in MATLAB, the following script was used to calculate what fraction of area under each electrode was covered by the bubble at time t:

```
%% Parameters
w = 0.04; % Electrode width
El = 0.01; % Electrode length
Ew = 0.04; % Electrode width
Bw = 0.03; % Bubble width
Bl = 0.015; % Bubble length, maximum 2Gl + El
Gl = 0.01; % Electrode gap length
v = 0.25; % Bubble speed
TE = El/v; % Time needed to travel one electrode length
TB = Bl/v; % Time needed to travel on bubble length
TG = Gl/v; % Time needed to travel on gap length
T = 1*(TB + 2*TE + TG); % Time from leading edge starts to overlap E1 to trailing
edge leaves E2
dt = 100000; % time steps
t = linspace(0,T,dt); % time vector

%% Calculations
% Rate of overlap E1 lower border
wt1 = Bw*(sin(t*pi*1/TB)).^.5; % width at x=0
dAdt1 = (wt1-imag(wt1)).*v;
dAdt1([round((TB)*dt/T):end]) = 0; % remove contribution when not valid
% Rate of overlap E1 upper border
wt2 = Bw*(sin((t-TE)*pi*1./TB)).^.5;
dAdt2 = (wt2-imag(wt2)).*v;
dAdt2([1:round((TE)*dt/T)]) = 0;% remove contribution when not valid
dAdt2([round((TE+TB)*dt/T):end]) = 0;% remove contribution when not valid

% Rate of overlap E2 lower border
wt3 = Bw*(sin((t-TE-TG)*1*pi./TB)).^.5;
dAdt3 = (wt3-imag(wt3)).*v;
dAdt3([1:round((TE+TG)*dt/T)]) = 0;% remove contribution when not valid
dAdt3([round((TB+TE+TG)*dt/T):end]) = 0;% remove contribution when not valid
% Rate of overlap E2 upper border
wt4 = Bw*(sin((t-TE-TE-TG)*1*pi./TB)).^.5;
dAdt4 = (wt4-imag(wt4)).*v;
dAdt4([1:round((TE+TE+TG)*dt/T)]) = 0;% remove contribution when not valid
dAdt4([round((TE+TB+TE+TG)*dt/T):end]) = 0;% remove contribution when not valid

A1 = cumsum((dAdt1-dAdt2)*T/dt); % Area covered by bubble under E1
A2 = cumsum((dAdt3-dAdt4)*T/dt); % Area covered by bubble under E2
Aw1 = El*Ew-A1; % Area covered by water under E1
Aw2 = El*Ew-A2; % Area covered by water under E2
```

APPENDIX 3, SIMULATION

Model differential equations was simulated numerically in MATLAB by a simple loop program running the differential equation 2.13 (model 1) and equation 4.5 and 4.6 (model 2) in small time steps. The equations describing the bubble overlap area are solved by the MATLAB script provided in appendix. The simulation outputs was voltage across the load over time. The current was from this calculated by ohms law.

$$voltage = resistance \times current.$$

From this, model prediction on charge transfer is calculated in the same way as for the measured data (equation 3.2 without filtering the simulated current data).

Model 1

Under follows the MATLAB script solving equation 2.13 for the potential across the load over time for a given load value. First, parameters are defined with and without the capacitive connection between E_2 and the water through ground. Second, one while loop runs the equation for the time interval where the bubble interacts with the electrodes (phase 1-4 in chapter 2). Third, a second while loop runs the same equations for a time interval following where there is no driving force except charge imbalance between electrodes that has still to equalize.

The parts of the script which imports plots the data etc. is not shown. The code describing the bubble overlap rate displayed in appendix 2 preceded the following code.

MATLAB script model 1:

```
d125 = 125*10^-6; % FEP thickness
d76 = 76*10^-6;
d50 = 50*10^-6;
d25 = 25*10^-6;

sigma125 = 30*10^-6; % FEP surface charge density, table 4.1.
sigma76 = sigma125*1.6;
sigma50 = sigma125*1.72;
sigma25 = sigma125*1.94;
epsilon = 2*8.85*10^-12; % FEP permittivity.
A = 0.01*0.04; % Electrode area.
Ae = 0.01*0.04; % Electrode area.
RL = 500*10^6; % Load resistance.
i = 1;
dt = T/100000;
% Parameters start value, t = 0.
V125(i) = 0; % Potential over load.
intV125(i) = 0; % Charge transferred through load.
V76(i) = 0;
intV76(i) = 0;
V50(i) = 0;
intV50(i) = 0;
V25(i) = 0;
intV25(i) = 0;
```

```
V125j(i) = 0; % Potential over load, when accounting for E2-water capacitance.
intV125j(i) = 0; % Charge transferred through load, when accounting for E2-water capacitance.
V76j(i) = 0;
intV76j(i) = 0;
V50j(i) = 0;
intV50j(i) = 0;
V25j(i) = 0;
intV25j(i) = 0;

% Parallel capacitance between E1 and E2.
Cp125 = 40*epsilon*A/0.01; % FEP125
Cp76 = 40*epsilon*A/0.01;
Cp50 = 40*epsilon*A/0.01;
Cp25 = 40*epsilon*A/0.01; % FEP25


% Serial capacitance, no capacitance between E2 and water.
Cs125 = 1 ./ (1./((Aw1*epsilon)./d125) + 1./((Aw2*epsilon)./d125 )+1*10^-10); % FEP125
Cs76 = 1 ./ (1./((Aw1*epsilon)./d76) + 1./((Aw2*epsilon)./d76 )+1*10^-10);
Cs50 = 1 ./ (1./((Aw1*epsilon)./d50) + 1./((Aw2*epsilon)./d50)+1*10^-10);
Cs25 = 1 ./ (1./((Aw1*epsilon)./d25) + 1./((Aw2*epsilon)./d25)+1*10^-10); % FEP25

% Serial capacitance, WITH large capacitance between E2 and water.
Cs25j = Aw1*epsilon/d25; % FEP25
Cs50j = Aw1*epsilon/d50;
Cs76j = Aw1*epsilon/d76;
Cs125j = Aw1*epsilon/d125; % FEP125


%% No capacitance between E2 and water.
while  i < 100000 % Time interval where bubble interacts with E1 and E2.
    i = i + 1;

    %Potential across load for FEP125.
    V125(i) =  (( A1(i)-1*A2(i))*sigma125 - intV125(i-1)*(1/RL) ) / (Cs125(i) + Cp125);
    %Amount of charge transferred through load.
    intV125(i) = intV125(i-1) + V125(i)*dt;

    V76(i) =  (( A1(i)-1*A2(i))*sigma76 - intV76(i-1)*(1/RL) ) / (Cs76(i) + Cp76);
    intV76(i) = intV76(i-1) + V76(i)*dt;

    V50(i) =  (( A1(i)-1*A2(i))*sigma50 - intV50(i-1)*(1/RL) ) / (Cs50(i) + Cp50);
    intV50(i) = intV50(i-1) + V50(i)*dt;

    V25(i) =  (( A1(i)-1*A2(i))*sigma25 - intV25(i-1)*(1/RL) ) / (Cs25(i) + Cp25);
    intV25(i) = intV25(i-1) + V25(i)*dt;

end

while  i < 200000 % Time interval where bubble has passed E2. Charge imbalance equalize passively.
    i = i + 1;


    V125(i) =  (( 0)*sigma125 - intV125(i-1)*(1/RL) ) / (Cs125(end) + Cp125);
    intV125(i) = intV125(i-1) + V125(i)*dt;

    V76(i) =  (( 0)*sigma76 - intV76(i-1)*(1/RL) ) / (Cs76(end) + Cp76);
    intV76(i) = intV76(i-1) + V76(i)*dt;

    V50(i) =  (( 0)*sigma50 - intV50(i-1)*(1/RL) ) / (Cs50(end) + Cp50);
    intV50(i) = intV50(i-1) + V50(i)*dt;

    V25(i) =  (( 0)*sigma25 - intV25(i-1)*(1/RL) ) / (Cs25(end) + Cp25);
    intV25(i) = intV25(i-1) + V25(i)*dt;

end

%% Large capacitance between E2 and water.

i = 1
while  i < 100000  % Time interval where bubble interacts with E1 and E2.
    i = i + 1;

    % Potential across load when accounting for capacitance between E2 and
```

```
    % water for FEP125.
    V125j(i) =  (( A1(i)-1*A2(i))*sigma125 - intV125j(i-1)*(1/RL) ) / (Cs125j(i) + Cp125);
    % Amount of charge transferred through load when accounting for
    % capacitance between E2 and water for FEP125.
    intV125j(i) = intV125j(i-1) + V125j(i)*dt;

    V76j(i) =  (( A1(i)-1*A2(i))*sigma76 - intV76j(i-1)*(1/RL) ) / (Cs76j(i) + Cp76);
    intV76j(i) = intV76j(i-1) + V76j(i)*dt;

    V50j(i) =  (( A1(i)-1*A2(i))*sigma50 - intV50j(i-1)*(1/RL) ) / (Cs50j(i) + Cp50);
    intV50j(i) = intV50j(i-1) + V50j(i)*dt;

    V25j(i) =  (( A1(i)-1*A2(i))*sigma25 - intV25j(i-1)*(1/RL) ) / (Cs25j(i) + Cp25);
    intV25j(i) = intV25j(i-1) + V25j(i)*dt;

end

while  i < 200000 % Time interval where bubble has passed E2. Charge imbalance equalize passively.
    i = i + 1;

    V125j(i) =  (( 0)*sigma125 - intV125j(i-1)*(1/RL) ) / (Cs125j(end) + Cp125);
    intV125j(i) = intV125j(i-1) + V125j(i)*dt;

    V76j(i) =  (( 0)*sigma76 - intV76j(i-1)*(1/RL) ) / (Cs76j(end) + Cp76);
    intV76j(i) = intV76j(i-1) + V76j(i)*dt;

    V50j(i) =  (( 0)*sigma50 - intV50j(i-1)*(1/RL) ) / (Cs50j(end) + Cp50);
    intV50j(i) = intV50j(i-1) + V50j(i)*dt;

    V25j(i) =  (( 0)*sigma25 - intV25j(i-1)*(1/RL) ) / (Cs25j(end) + Cp25);
    intV25j(i) = intV25j(i-1) + V25j(i)*dt;

end
```

Tabel A3.1 show the simulation results from model 1 with parameters as stated in table 4.2. Peak current in first triplet pulse (I_{max}), charge transferred through outer circuit per bubble (Q), and duration of first triplet pulse (Δt). The results with the capacitive connection between the top electrode and the water accounted for (M1*) is denoted with a star, for example Q*.

	I^*_{max} $[A \times 10^{-6}]$	$I_{max}(\sigma)$ $[A \times 10^{-6}]$	Q^* $[C \times 10^{-9}]$	Q $[C \times 10^{-9}]$	Δt^* $[s]$	Δt $[s]$
FEP25, 1	0.4392	0.4379	63.3	63.3	0.050	0.050
FEP25, 500	0.1993	0.2248	13.6	26.6	0.078	0.075
FEP25, 1000	0.1141	0.1335	7.6	13.9	0.083	0.081
FEP25, 2000	0.06139	0.0734	3.9	6.9	0.086	0.085
FEP25, 3000	0.04198	0.05062	2.6	4.5	0.088	0.087
FEP50, 1	0.3888	0.3882	56.2	56.2	0.050	0.050
FEP50, 500	0.2434	0.2592	20.7	33.2	0.072	0.07
FEP50, 1000	0.1491	0.1651	10.7	19.5	0.079	0.077
FEP50, 2000	0.08375	0.0952	5.9	9.9	0.084	0.083
FEP50, 3000	0.05818	0.06683	4.0	6.6	0.086	0.085
FEP76, 0	0.3604	0.36	52.1	52.1	0.050	0.050
FEP76, 500	0.2571	0.2662	24.8	35.1	0.069	0.067
FEP76, 1000	0.1643	0.1765	13.5	22.1	0.077	0.075
FEP76, 2000	0.09493	0.1046	7.0	11.7	0.083	0.081
FEP76, 3000	0.06669	0.0743	4.855	7.731	0.085	0.084
FEP125, 0	0.2252	0.2251	32.59	32.59	0.05	0.05
FEP125, 500	0.1780	0.1798	19.37	24.23	0.066	0.065
FEP125, 1000	0.1191	0.1242	11.40	16.36	0.074	0.072
FEP125, 2000	0.07107	0.0759	5.828	9.08	0.081	0.080
FEP125, 3000	0.05059	0.05454	3.942	6.075	0.084	0.083

Table A3.1: Simulation results from model 1 with parameters as stated in table 4.2.

Model 2

Under follows the MATLAB script solving equation 4.5 and 4.6 for the potential across the load over time for a given load value. First, parameters are defined. Second, one while loop runs the equation for the time interval where the bubble interacts with the electrodes (phase 1-4 in chapter 2). Third, a second while loop runs the same equations for a time interval following where there is no driving force except charge imbalance between electrodes that has still to equalize.

The parts of the script which imports plots the data etc. is not shown. The code describing the bubble overlap rate displayed in appendix 2 preceded the following code.

MATLAB script model 1:

```
d125 = 125*10^-6; % FEP thicknesses.
d76 = 76*10^-6 ;
d50 = 50*10^-6;
d25 = 25*10^-6;

sigma125 = 45*10^-6; %FEP surface charge density based on table 4.1.
sigma76 = sigma125* 1.6;
sigma50 = sigma125 * 1.72;
sigma25 = sigma125 * 1.94;
epsilon = 2*8.85*10^-12; % FEP permittivity.
A = 0.01*0.04; % Electrode area
Ae = 0.01*0.04;
RL = 500*10^6; % Load resistance.
i = 1;
dt = T/100000;

% Start value parameters
Cjord = 100*10^-12; % Calculated capacitance between E2 and water.
CpGlobal = 40*epsilon*(4*10^-4)/0.01; % Parallel capacitance.

C2_125 = Aw2*epsilon/d125 + Cjord; % CE2
C1_125 = Aw1*epsilon/d125; % CE1
Cp125 = CpGlobal;
intIs1_125 = A1*sigma125; % Model current  source parallel to E1, integral.
Is1_125 = (dAdt1-dAdt2)*sigma125; % Model current  source parallel to E1.
intIs2_125 = A2*sigma125;
Is2_125 = (dAdt3-dAdt4)*sigma125;
V1_125(i) = 0; % potential on E1 side of load.
V2_125(i) = 0; % potential on E1 side of load.
dV1_125dt(i) = 0; % Change rate in potential on E1 side of load.
dV2_125dt(i) = 0; % Change rate in potential on E2 side of load.

C2_76 = Aw2*epsilon/d76 + Cjord;
C1_76 = Aw1*epsilon/d76;
Cp76 = CpGlobal;
intIs1_76 = A1*sigma76;
Is1_76 = (dAdt1-dAdt2)*sigma76;
intIs2_76 = A2*sigma76;
Is2_76 = (dAdt3-dAdt4)*sigma76;
V1_76(i) = 0;
V2_76(i) = 0;
dV1_76dt(i) = 0;
dV2_76dt(i) = 0;

C2_50 = Aw2*epsilon/d50 + Cjord;
C1_50 = Aw1*epsilon/d50;
Cp50 = CpGlobal;
intIs1_50 = A1*sigma50;
Is1_50 = (dAdt1-dAdt2)*sigma50;
intIs2_50 = A2*sigma50;
Is2_50 = (dAdt3-dAdt4)*sigma50;
V1_50(i) = 0;
V2_50(i) = 0;
```

```
dV1_50dt(i) = 0;
dV2_50dt(i) = 0;

C2_25 = Aw2*epsilon/d25 + Cjord;
C1_25 = Aw1*epsilon/d25;
Cp25 = CpGlobal;
intIs1_25 = A1*sigma25;
Is1_25 = (dAdt1-dAdt2)*sigma25;
intIs2_25 = A2*sigma25;
Is2_25 = (dAdt3-dAdt4)*sigma25;
V1_25(i) = 0;
V2_25(i) = 0;
dV1_25dt(i) = 0;
dV2_25dt(i) = 0;


%% Loop running DE.
while  i < 100000 % This is the interval the bubble interacts with E1 and E2
    i = i + 1;
    % FEP125
    Ct125(i) = (1 + C1_125(i)./C2_125(i));            % Serial capacitance CE1/CE2 over time.
    dC1_125dt(i) = (C1_125(i) - C1_125(i-1).*dt);     % Change in CE1.
    dC2_125dt(i) = (C2_125(i) - C2_125(i-1).*dt);     % Change in CE2.
    dCt125dt(i) = (Ct125(i) - Ct125(i-1).*dt);        % Change in serial capacitance.
    V1_125(i) = V1_125(i-1) + dV1_125dt(i-1)*dt ;     % Potential on E1 side of load.
    V2_125(i) = V2_125(i-1) + dV2_125dt(i-1)*dt ;     % Potential on E2 side of load.
    dV1_125dt(i) = ( -Is1_125(i) -V1_125(i-1).*(1/RL+dC1_125dt(i)) + V2_125(i)/RL  + Cp125*dV2_125dt(i-
1) )./ (C1_125(i)+Cp125);
    % Change in potential on E1 side of load.
    dV2_125dt(i) = ( -Is2_125(i) -V2_125(i-1).*(1/RL+dC2_125dt(i)) + V1_125(i)/RL  + Cp125*dV1_125dt(i)
)./ (C2_125(i)+Cp125);

    % FEP76
    Ct76(i) = (1 + C1_76(i)./C2_76(i));
    dC1_76dt(i) = (C1_76(i) - C1_76(i-1).*dt);
    dC2_76dt(i) = (C2_76(i) - C2_76(i-1).*dt);
    dCt76dt(i) = (Ct76(i) - Ct76(i-1).*dt);
    V1_76(i) = V1_76(i-1) + dV1_76dt(i-1)*dt ;
    V2_76(i) = V2_76(i-1) + dV2_76dt(i-1)*dt ;
    dV1_76dt(i) = ( -Is1_76(i) -V1_76(i-1).*(1/RL+dC1_76dt(i)) + V2_76(i)/RL  + Cp76*dV2_76dt(i-1) )./
(C1_76(i)+Cp76);
    dV2_76dt(i) = ( -Is2_76(i) -V2_76(i-1).*(1/RL+dC2_76dt(i)) + V1_76(i)/RL  + Cp76*dV1_76dt(i) )./
(C2_76(i)+Cp76);

    % FEP50
    Ct50(i) = (1 + C1_50(i)./C2_50(i));
    dC1_50dt(i) = (C1_50(i) - C1_50(i-1).*dt);
    dC2_50dt(i) = (C2_50(i) - C2_50(i-1).*dt);
    dCt50dt(i) = (Ct50(i) - Ct50(i-1).*dt);
    V1_50(i) = V1_50(i-1) + dV1_50dt(i-1)*dt ;
    V2_50(i) = V2_50(i-1) + dV2_50dt(i-1)*dt ;
    dV1_50dt(i) = ( -Is1_50(i) -V1_50(i-1).*(1/RL+dC1_50dt(i)) + V2_50(i)/RL  + Cp50*dV2_50dt(i-1) )./
(C1_50(i)+Cp50);
    dV2_50dt(i) = ( -Is2_50(i) -V2_50(i-1).*(1/RL+dC2_50dt(i)) + V1_50(i)/RL  + Cp50*dV1_50dt(i) )./
(C2_50(i)+Cp50);

    % FEP25
    Ct25(i) = (1 + C1_25(i)./C2_25(i));
    dC1_25dt(i) = (C1_25(i) - C1_25(i-1).*dt);
    dC2_25dt(i) = (C2_25(i) - C2_25(i-1).*dt);
    dCt25dt(i) = (Ct25(i) - Ct25(i-1).*dt);
    V1_25(i) = V1_25(i-1) + dV1_25dt(i-1)*dt ;
    V2_25(i) = V2_25(i-1) + dV2_25dt(i-1)*dt ;
    dV1_25dt(i) = ( -Is1_25(i) -V1_25(i-1).*(1/RL+dC1_25dt(i)) + V2_25(i)/RL  + Cp25*dV2_25dt(i-1) )./
(C1_25(i)+Cp25);
    dV2_25dt(i) = ( -Is2_25(i) -V2_25(i-1).*(1/RL+dC2_25dt(i)) + V1_25(i)/RL  + Cp25*dV1_25dt(i) )./
(C2_25(i)+Cp25);
end
```

```
while  i < 400000 % This is the interval after the bubble has passed. Current still flows because of
imbalance in charge.

    i = i + 1;

    Ct125(i) = Ct125(100000);
    dC1_125dt(i) = 0;
    dC2_125dt(i) = 0;
    dCt125dt(i) = 0;
    V1_125(i) = V1_125(i-1) + dV1_125dt(i-1)*dt ;
    V2_125(i) = V2_125(i-1) + dV2_125dt(i-1)*dt ;
    dV1_125dt(i) = ( -0 -V1_125(i-1).*(1/RL+dC1_125dt(i)) + V2_125(i)/RL  + Cp125*dV2_125dt(i-1) )./
(C1_125(100000)+Cp125);
    dV2_125dt(i) = ( -0 -V2_125(i-1).*(1/RL+dC2_125dt(i)) + V1_125(i)/RL  + Cp125*dV1_125dt(i) )./
(C2_125(100000)+Cp125);

    Ct76(i) = Ct76(100000);
    dC1_76dt(i) = 0;
    dC2_76dt(i) = 0;
    dCt76dt(i) = 0;
    V1_76(i) = V1_76(i-1) + dV1_76dt(i-1)*dt ;
    V2_76(i) = V2_76(i-1) + dV2_76dt(i-1)*dt ;
    dV1_76dt(i) = ( -0 -V1_76(i-1).*(1/RL+dC1_76dt(i)) + V2_76(i)/RL  + Cp76*dV2_76dt(i-1) )./
(C1_76(100000)+Cp76);
    dV2_76dt(i) = ( -0 -V2_76(i-1).*(1/RL+dC2_76dt(i)) + V1_76(i)/RL  + Cp76*dV1_76dt(i) )./
(C2_76(100000)+Cp76);

    Ct50(i) = Ct50(100000);
    dC1_50dt(i) = 0;
    dC2_50dt(i) = 0;
    dCt50dt(i) = 0;
    V1_50(i) = V1_50(i-1) + dV1_50dt(i-1)*dt ;
    V2_50(i) = V2_50(i-1) + dV2_50dt(i-1)*dt ;
    dV1_50dt(i) = ( -0 -V1_50(i-1).*(1/RL+dC1_50dt(i)) + V2_50(i)/RL  + Cp50*dV2_50dt(i-1) )./
(C1_50(100000)+Cp50);
    dV2_50dt(i) = ( -0 -V2_50(i-1).*(1/RL+dC2_50dt(i)) + V1_50(i)/RL  + Cp50*dV1_50dt(i) )./
(C2_50(100000)+Cp50);

    Ct25(i) = Ct25(100000);
    dC1_25dt(i) = 0;
    dC2_25dt(i) = 0;
    dCt25dt(i) = 0;
    V1_25(i) = V1_25(i-1) + dV1_25dt(i-1)*dt ;
    V2_25(i) = V2_25(i-1) + dV2_25dt(i-1)*dt ;
    dV1_25dt(i) = ( -0 -V1_25(i-1).*(1/RL+dC1_25dt(i)) + V2_25(i)/RL  + Cp25*dV2_25dt(i-1) )./
(C1_25(100000)+Cp25);
    dV2_25dt(i) = ( -0 -V2_25(i-1).*(1/RL+dC2_25dt(i)) + V1_25(i)/RL  + Cp25*dV1_25dt(i) )./
(C2_25(100000)+Cp25);
end
```

Tabel A3.2 show the simulation prediction from model 2 on charge transferred through outer circuit per bubble, with capacitive connection between top electrode and water accounted for. Parameters as stated in table 4.4.

Resistance [GΩ]	**FEP25 $[10^{-9}C]$**	**FEP50 $[10^{-9}C]$**	**FEP76 $[10^{-9}C]$**	**FEP125 $[10^{-9}C]$**
0	57.7	51.3	47.7	29.9
.5	16.8	21.9	23.9	17.6
1	8.1	11.3	13.2	10.3
2	4.3	6.4	7.8	6.3
3	2.9	4.3	5.3	4.4

Table A3.2: M2 prediction on charge transferred per bubble through outer circuit.*

APPENDIX 4, EXPERIMENT

Tabel A4.1 shows the order at which data was collected from different FEP thickness and load combinations. All experiments were done the same day in an interval of 6 hours.

Nr.	**Device**	**Load resistance** $[10^9\ ohm\ ]$	**Data collection time [s]**
1	FEP 127	0	1000
2	FEP 127	0.5	600
3	FEP 127	1	600
4	FEP 127	2	600
5	FEP 127	3	600
6	FEP 76	0	600
7	FEP 76	0.5	600
8	FEP 76	1	600
9	FEP 76	2	600
10	FEP 76	3	600
11	FEP 50	0	600
12	FEP 50	0.5	600
13	FEP 50	1	600
14	FEP 50	2	600
15	FEP 50	3	600
16	FEP 25	0	600
17	FEP 25	0.5	600
18	FEP 25	1	600
19	FEP 25	2	600
20	FEP 25	3	600
21	FEP 125	2	300
22	FEP 125	0	300
23	FEP 125	0.5	300

Table A4.1: The sequence of experimental runs.

Figure A.4.1 shows two pictures of the same bubble with a small time difference.

Figure A.4.1: Picture of bubble as it leaves the pipe and its leading edge starts to overlap with the bottom electrode (lower panel) and the same bubble at a later stage (upper panel). Note that the BMAT depicted here has a gap between the electrodes of only 1 mm. The depicted BMAT is identical to the ones discussed in the thesis in any other measure. The relative position of the bottom electrode is equal. The upper electrode is lower than in the discussed devices.